Alma Mater Studiorum - Università di Bologna

Facoltà di Scienze Matematiche Fisiche e Naturali

Corso di Laurea Magistrale in Fisica

Study of low p_T D^0 meson production at CDF II in $p\bar{p}$ collisions at $\sqrt{s} = 900$ GeV

Relatore:

Dott. Stefano Zucchelli

Correlatore:

Dott. Manuel Mussini

Candidato:

Elena Gramellini

Anno Accademico 2010-2011

III Sessione

To the loving memory of
Prof. Franco Rimondi

Contents

Introduction

In this thesis a study of the D^0 meson production in proton-antiproton collisions is presented. The data were collected with the CDF II detector at the Tevatron Collider of the Fermi National Accelerator Laboratory. This work is part of a specific effort by the CDF Collaboration to measure the inclusive differential cross section of prompt charmed mesons in the low p_T kinematic region.

The reconstruction of the neutral charmed meson (D^0) at low momenta and at different energies gives the opportunity to enrich the knowledge of the behavior of the strong interaction in the region where c-quark production is nearly in non-perturbative condition. In fact, the actual QCD theory cannot predict the behavior of the strong interaction in the low transferred four-momentum region (low Q^2) because of the running of the strong coupling constant α_s. In these kinematic conditions, α_s is of the order of the unity, thus perturbative expansions are no longer permitted. Nowadays, some phenomenological models have been formulated, but they are usually able to describe only few aspects of the observed physical quantities; however, they fail in predicting the strong interaction behavior in its whole complexity. Experimental studies in this region of interaction are crucial to overcome the theoretical limitation and to model new theories.

An analysis published by the CDF Collaboration in 2003 probed a minimum p_T of the D^0 of only 5.5 GeV/c because of the biases introduced by the trigger selection. In a recent study performed at the center of mass energy of 1.96 TeV, a lower limit of 1.5 GeV/c is reached using the Minimum Bias

(MB) and Zero Bias (ZB) data samples so that no bias is introduced whatsoever.
This thesis, carried out within the Bologna research group, complements that studies as it concerns the analysis of the MB and ZB data samples collected during a low energy scan at the energy of 900 GeV in the center of mass. This work is the first measurement of D^0 production ever performed in the low p_T range at this energy. The sample analyzed is the largest ever collected by a hadron collider in these conditions.

The primary purpose of the present analysis is the measurement of the D^0 raw yields as a function of the transverse momentum: the main step in the measurement of the D^0 production cross section. The decay channel used here is $D^0 \rightarrow K^-\pi^+$ ($\bar{D}^0 \rightarrow K^+\pi^-$) because of its simple topology, its high reconstruction efficiency (all the produced particles are charged and therefore observable in the tracking system) and its relatively high branching ratio (about 3.9%).

A preliminary task towards the measurement of the yields has been completed during the thesis work: since the beam position was not recorded for the runs of low energy scan, it has been reconstructed from data run-by-run. This was a necessary step to unfold the D^0 signal whose signature is a secondary vertex displaced from the beam of several microns. Finally the raw yields as a function of $p_T(D^0)$ have been measured.

This thesis is composed of seven chapters. In the first one, a theoretical outline is given. The second one shortly describes the CDF detector with some emphasis on the subdetectors used for this analysis. Chapter three describes the data samples and the analysis strategy. Chapter four is dedicated to the reconstruction of the beam position and chapter five to the preliminary data simulations. In chapter six, the search of the signal is finalized and in chapter seven the measurement of the raw yields as a function of $p_T(D^0)$ is presented.

Chapter 1

Theory and motivation

1.1 The Standard Model

The Standard Model (SM) is a theory that describes the strong, electromagnetic and weak interactions of the elementary particles in the framework of the quantum field theory. The weak and the electromagnetic interactions are unified into the electroweak interaction.

The SM is a gauge theory based on the local group of symmetry

$$G_{SM} = SU(3)_C \otimes SU(2)_T \otimes U(1)_Y \tag{1.1}$$

where the subscripts indicate the conserved charges: the strong charge, or color C, the weak isospin T (or rather its third component T_3) and the hypercharge Y. These quantities are related to the electric charge Q through the Gell-Mann-Nishijima relation:

$$Q = \frac{Y}{2} + T_3. \tag{1.2}$$

In the quantum field framework, the elementary particles correspond to the irreducible representations of the G_{SM} symmetry group. In particular, the particles with half-integer spin are called fermions and they are described by the Fermi-Dirac statistics, whether the particles with integer spin are called bosons and they are described by the Bose-Einstein statistics. The fundamental fermions and their quantum numbers are listed in Tab 1.1.

Generation:	I	II	III	T_3	Y	Q
leptonic doublets	$\begin{pmatrix} \nu_{eL} \\ e_L \end{pmatrix}$	$\begin{pmatrix} \nu_{\mu L} \\ \mu_L \end{pmatrix}$	$\begin{pmatrix} \nu_{\tau L} \\ \tau_L \end{pmatrix}$	$1/2$ $-1/2$	-1	0 -1
leptonic singlets	e_R	μ_R	τ_R	0	-2	-2
quark doublets	$\begin{pmatrix} u_L \\ d'_L \end{pmatrix}$	$\begin{pmatrix} c_L \\ s'_L \end{pmatrix}$	$\begin{pmatrix} t_L \\ b'_L \end{pmatrix}$	$1/2$ $-1/2$	$1/3$	$2/3$ $-1/3$
quark singlets	u_R d_R	c_R s'_R	t_R b'_R	0	$4/3$ $-2/3$	$2/3$ $-1/3$

Table 1.1: SM elementary fermions. The subscripts $_L$ and $_R$ indicate respectively the negative helicity (left-handed) and the positive helicity (right-handed).

Charged leptons interact via the weak and the electromagnetic forces, while neutrinos only interact via the weak force. Quarks can also interact via the strong force; they are triplets of $SU(3)_C$, that is they can exist in three different colors: C = R, G, B. If one chooses a base where u, c and t quarks are simultaneously eigenstates of both the strong and the weak interactions, the remaining eigenstates are usually written as d, s and b for the strong interaction and d', s' and b' for the weak interaction, because the latter ones are the result of a Cabibbo rotation on the first ones.

The gauge group univocally determines the interactions and the number of gauge bosons that carry them; the gauge bosons correspond to the generators of the group: 8 gluons (g) for the strong interaction, a photon (γ) and three bosons ($W^{\pm}$, Z^0) for the electroweak interaction.

A gauge theory by itself can not provide a description of massive particles, but it is experimentally well know that most of the elementary particles have non-zero masses. The introduction of massive fields in the SM lagrangian would make the theory non-renormalizable, and - so far - mathematically impossible to handle. This problem is solved in the SM by the introduction of a scalar iso-doublet $\Phi(x)$, the $Higgs\ field$, see Tab 1.2, which gives masses

to W^+, W^- and Z^0 gauge bosons and to the fermions [1, 2].

	T_3	Y	Q
Higgs doublet $\Phi(x) \equiv \begin{pmatrix} \phi^+(x) \\ \phi^0(x) \end{pmatrix}$	$1/2$ $-1/2$	$+1$	1 0

Table 1.2: Higgs doublet and its third component of the weak isospin, hypercharge and electric charge.

The existence of the Higgs boson has not been experimentally confirmed yet and the Higgs mass is one of the free parameters of the SM.

1.2 Strong interaction theory: QCD

The Quantum Chromodynamics (QCD) is the current theory used to describe the strong interaction; it is based on the non-abelian SU(3) gauge group and it governs the dynamics of quarks and gluons.

QCD predictions are well tested at high energies where perturbative approaches are possible because of the smallness of its coupling constant, α_s, see sec. 1.2.1; on the other hand, in the low-energy region QCD becomes a strongly-coupled theory and a perturbative approach can not be applied.

In order to obtain a relativistic quantum field theory of interacting quarks and gluons, one should start from the QCD lagrangian density:

$$\mathcal{L}_{QCD} = -\frac{1}{4} G_a^{\mu\nu} G^a_{\mu\nu} + \sum_f \bar{q}_f [i\gamma^\mu D_\mu - m_f] q_f \tag{1.3}$$

where q stands for the quark field and f for the quark flavours relevant in the interaction, while $G_a^{\mu\nu}$ is the gluon field strength tensor, namely

$$G_a^{\mu\nu} = \partial^\mu A_a^\nu - \partial^\nu A_a^\mu + g f_a^{bc} A_b^\mu A_c^\nu, \tag{1.4}$$

D^μ is the gauge covariant derivative, namely

$$D^\mu = \partial^\mu - i\frac{g}{2} A_a^\mu \lambda^a, \tag{1.5}$$

A_a^μ is the gluon field, f_a^{bc} are the antisymmetric structure constants and g a constant related to α_s via the formula $\alpha_s = g^2/4\pi$.

Quarks and gluons are the fundamental degrees of freedom of the QCD theory; they both carry color charge, so the gluons that mediate the strong interaction can interact among themselves. Free quarks and gluons have never been observed because of the confinement of the color charge. The QCD field equations give rise to the complex world of nuclear and hadronic physics, that is only qualitatively understood by now.

An intrinsic QCD scale, Λ_{QCD}, is set through the standard process of the renormalization in quantum field theory; below the Λ_{QCD} scale the standard perturbation theory is no longer valid because of the running of the coupling constant.
In principle, all the hadron masses could be evaluated in terms of Λ_{QCD}, starting from a normalization parameter left free in the theory. The measured value of the proton mass appears to be a suitable choice for the normalization parameter because it is non-zero in virtue of the energy of the confined quarks and gluons [3].

There is no mathematical description of color confinement but, qualitatively, this is believed to deal with the fact that the quark and gluon bilinears $\bar{q}^a q^a$ and $G^a_{\mu\nu} G_a^{\mu\nu}$ acquire non-zero vacuum expectation values. Even if the QCD Lagrangian is well known and the strong interactions are understood in principle, the features of low transferred momentum QCD phenomena are far to be theoretically predicted. That is why experiments which test QCD in the non-perturbative regime are fundamental to improve our understanding of the strong interactions: they are the basis on which orient further theoretical and experimental researches.

1.2.1 QCD coupling constant

The qualitative understanding of QCD is based on the classical calculation of the dependence of the QCD coupling constant on the renormalization scale of energy, μ. The simplest way to show this dependence is to define the so

called β-function:

$$\beta(\alpha_s) \equiv \frac{\mu}{2}\frac{\partial\alpha}{\partial\mu} = -\frac{\beta_0}{4\pi}\alpha_s^2 - \frac{\beta_1}{8\pi^2}\alpha_s^3 - ... \tag{1.6}$$

where

$$\beta_0 = 11 - \frac{2}{3}n_f \tag{1.7}$$

$$\beta_1 = 51 - \frac{19}{3}n_f \tag{1.8}$$

and n_f is the number of *active quarks*, i.e. the quarks whose mass is less than μ. One introduces the arbitrary scale Λ to provide the μ dependence of α_s and solve the differential equation (1.6).
A solution in the first order of approximation is the following [4]:

$$\alpha_s(\mu^2) = \frac{4\pi}{\beta_0 \ln(\mu^2/\Lambda^2)} + \mathcal{O}\Big(\frac{\ln[\ln(\mu^2/\Lambda^2)]}{\ln^2(\mu^2/\Lambda^2)]}\Big). \tag{1.9}$$

The solution (1.9) shows the two main properties of the theory: the asymptotic freedom

$$\alpha_s \overset{\mu\to+\infty}{\longrightarrow} 0 \tag{1.10}$$

and the strong coupling scale below $\mu \sim \Lambda$.

As one can see from Fig. 1.1, it is possible to roughly divide the physics of the strong interaction into two regions as a function of the energy of the process: the perturbative QCD (high transferred momentum and little α_s) and the non-perturbative QCD (low transferred momentum and high α_s).

The predictions of the QCD in the perturbative region (pQCD), where the standard Feynman rules apply, have been well tested. In the perturbative regime, the magnitude of the coupling constant is the fundamental parameter for pQCD predictions. A multitude of phenomena, such as scaling violations in deep inelastic scattering, high-energy hadron collisions, heavy-quarkonium (in particular bottomonium) decay, jet rates in e^+e^- collisions and in ep collisions depends on the value of QCD coupling constant; for this reason, we can then extrapolate the coupling constant value in a huge range of μ because we are able to measure it for many different processes. The different values

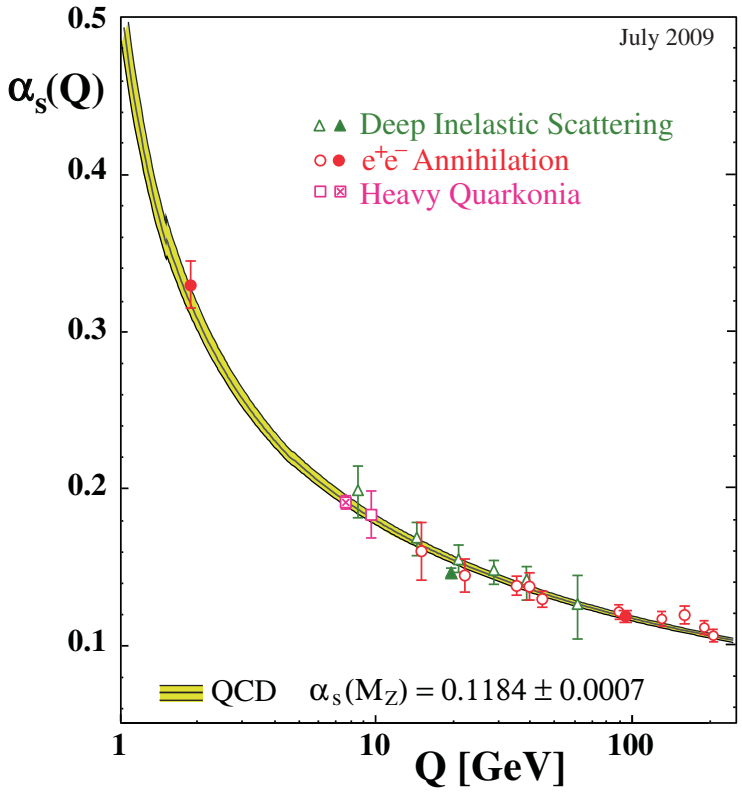

Figure 1.1: The running of the strong coupling constant as a function of the transferred momentum (i.e. scale of energy).

of α_s for the different processes are listed in Fig. 1.2; they are consistent with each other and their average value is [4]:

$$\alpha_s(m^2_{Z^0}) = 0.1184 \pm 0.0007. \tag{1.11}$$

The non-perturbative regime area is quantitatively much less understood: it is the area of the strong nuclear forces and the hadronic resonances, where we still have several unresolved questions.

1.2.2 Lattice QCD and Effective Field Theory

The theoretical approaches to the non-perturbative QCD region are essentially two: the Lattice QCD (LQCD) and the Effective Field Theory (EFT).

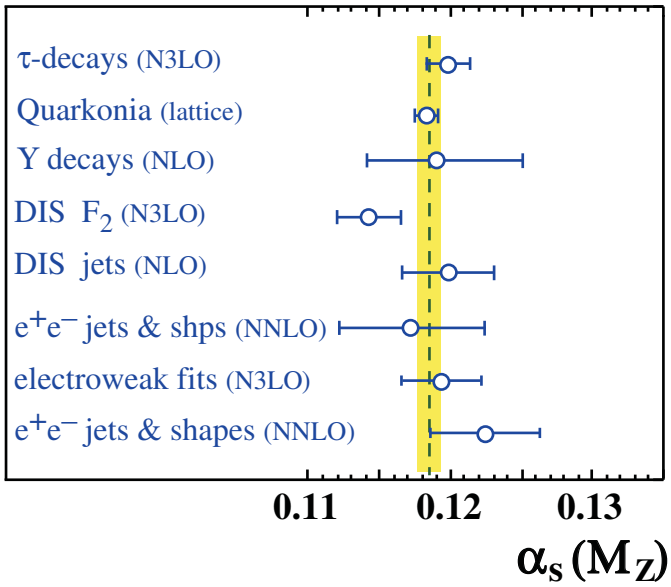

Figure 1.2: Summary of $\alpha_s(m_{Z^0})$ measurements and world average value.

LQCD is a numerical approach. The theoretical idea underlying this framework is to discretize QCD equations of motion on a 4-dimentional space-time lattice and to solve them by a large scale of numerical simulations on big computers. The discretization is removed by letting the lattice spacing tend to zero; the continuum is then restored.
Even if LQCD theoretical principles were originally proposed in 1974, this approach has made enormous progress over the last decades, mainly due to the empowerment of the computer technology.

An EFT is a model equivalent to QCD in a certain energy range that can be formulated under a series of approximations. One typical approximation is the assumption of negligible mass of the up, down and strange quarks with respect to Λ_{QCD} [5]. An EFT can in some cases provide a solution in calculation from QCD where several dynamical scales are involved; for example combining LQCD with EFT technique has turned out to be a very powerful method. In recent years a variety of EFTs with quark and gluon degrees of freedom have been developed.

1.3 *Charm* physics and D mesons

The D mesons family is a family of hadrons containing the c quark. It is formed by the D^0, D^+, D^{*+} and D_s mesons and their antiparticles.

The existence of hadrons with the charm quantum number had been predicted in 1963 because the existence of a further quark was necessary to perform the normalization of the weak interactions in the framework of non-abelian gauge theories [6, 7].

In order to keep the theory consistent and manage consequent possible anomalies, the main features of charm quarks (c) were predicted to be as follows:

- c quarks have the same coupling as u quarks, but their mass is much heavier, namely about 2 GeV/c^2;
- they form charged and neutral hadrons, of which (in the $C = 1$ sector) three mesons and four baryons decay only weakly with lifetimes roughly 10^{-13} s (they are considered indeed stable);
- charm decay produces direct leptons and preferentially strange hadrons.

The researches on the charm physics during the last 50 years have shown how these assumptions were extraordinary reliable.

c quark occupies a unique place among up-type quarks, because it is the only up-type quarks whose hadronization (and the consequent decay) can be studied. This is due to the fact that, on the heavy side of the spectrum, the t quark decays before it can hadronize, while on the lighter side, the u quark can be considered stable. u quark forms only two kinds of neutral hadron which decay weakly, neutrons and pions: the decay of the former is due to the weak decay of quark d and, in the latter, quark and antiquark of the first family annihilate each other.

The charm is an up-type quark, so loop diagrams do not involve the heavy top quark; the SM prediction for charm hadronization and decay is then smaller by many orders of magnitude than the down-type corresponding processes. Intermediate meson-states are expected to contribute at the 10^{-3}

level and thus overshadow the short-distance contributions. As mentioned, SM physics lowers the probability to observe loop-mediated processes; on the contrary, new physics may enhance them and it could be easier to detect in the charm system than in the bottom system. Experimentally, charm shows more distinct signatures than the B-system because c branching fractions into fully reconstructed modes are up to the 10 % level, while the product of branching ratios to fully reconstruct a b decay is typically at the 10^{-4} level. Very specific tags are present in the charm decay; for example, in the $D^{*+} \to D^0\pi^+$ decay, the slow pion tags the D^0 flavor at production with an efficiency of almost 100 %.

Mixing of the neutral mesons can occur in the charm system through box-diagram, just like the kaon and the B systems. These box-diagram can involve only d, s and b quarks because c quark is an up-type quark, thus, again, the large contribution of the heavy t quark is missing.

In the charm framework, the mixing of neutral mesons is studied in the case of $D^0 - \bar{D^0}$ oscillations. The mixing is describe in terms of two parameters: $x_D \equiv \frac{\Delta M_D}{\Gamma_D}$ and $y_D \equiv \frac{\Delta\Gamma_D}{2\Gamma_D}$, where ΔM_D is the mass difference between D^0 and $\bar{D^0}$ ($\Delta M_D \leq 1.3 \times 10^{-13}$ GeV) and $\Delta\Gamma_D$ is the difference between their decay rate. The box-diagram predictions for x_D and y_D are at the 10^{-5} level [8]. New physics should have a little effect on $\Delta\Gamma_D$, but may have significant contributions to ΔM_D up to values of x_D at the 1 % level. Contributions from non-perturbative QCD tend to increase $\Delta\Gamma_D$ but the effect on ΔM_D is small. An observation of the x_D at the percent level together with a strong limit on y_D at the 10^{-3} level would be a strong indication for new physics.

The LHCb collaboration recently announced preliminary evidence for CP violation in D^0 meson decays [9]. They reported a 3.5σ evidence for a non-zero value of the difference between the time-integrated CP asymmetries in the decays $D^0 \to K^+K^-$ and $D^0 \to \pi^+\pi^-$. They evaluated Δa_{CP} to be $\Delta a_{CP} \equiv a_{K^+K^-}$ - $a_{\pi^+\pi^-} = -(0.82 \pm 0.21 \pm 0.11)\%$, where:

$$a_{K^+K^-} = \frac{\Gamma(D^0 \to K^+Ki^-) - \Gamma(\bar{D^0} \to K^+K^-)}{\Gamma(D^0 \to K^+K^-) + \Gamma(\bar{D^0} \to K^+K^-)} \tag{1.12}$$

and

$$a_{\pi^+\pi^-} = \frac{\Gamma(D^0 \to \pi^+\pi^-) - \Gamma(\bar{D}^0 \to \pi^+\pi^-)}{\Gamma(D^0 \to \pi^+\pi^-) + \Gamma(\bar{D}^0 \to \pi^+\pi^-)}. \tag{1.13}$$

The CDF Collaboration is going to publish a similar result soon.

1.4 Charmed hadrons production and D^0 cross section measurements

Recently, thorough experimental and theoretical studies have been made about the inclusive production of charmed hadrons (X_c) at hadron colliders. Important results on the charm physics come from the PHENIX and the STAR experiments at the BNL Relativistic Heavy Ion Collider (RHIC). Both collaborations reported the measure of non-photonic electron production through charm and bottom decays in pp, dAu and AuAu collisions at $\sqrt{s} = 200$ GeV [11, 12]. The STAR Collaboration also presented mid-rapidity open charm spectra from direct reconstruction of decays in dAu collisions and indirect e^+e^- measurements via charm semileptonic decays in pp and dAu collisions at the center of mass energy, $\sqrt{s}$, of 200 GeV [13]. The main disadvantage of these results is that RHIC data only covered a very limited low-p_T range.

The latest result concerning the charm physics is the measurement of the inclusive open charm production in p-p and Pb-Pb collision performed by the ALICE collaboration [14]. A preliminary measurement of the D^0, D^{*+} and D^+ differential cross sections at $\sqrt{s} = 7$ TeV was released. The total charm production cross section was estimate using the extrapolation of the D meson cross section measurements to the full kinematic phase space. Fig 1.3 shows the $pp \to c\bar{c}$ cross section as a function of centre of mass energy for various experiments.

In 2003, the CDF Collaboration published the measurements of the differential cross sections for the inclusive production of charmed hadrons as a function of the transverse momentum for $p_T \geq 5.5$ GeV/c [10], at $\sqrt{s} = 1.97$ TeV. Fig. 1.4 shows CDF differential cross section measurements for the

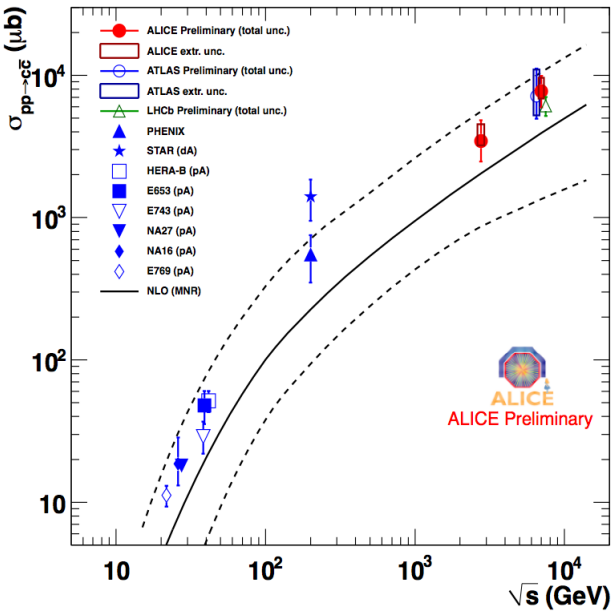

Figure 1.3: Total charm production cross section as a function of centre of mass energy for various experiments [14].

mesons of the D family.

From the theoretical point of view, the cross section for the inclusive production of X_c mesons can be calculated by the convolution of universal parton distribution functions (PDFs) and universal fragmentation functions (FFs) with calculable hard-scattering cross sections via perturbative approach. The non-perturbative part in the form of PDFs and FFs is input by fits from other processes. The PDFs and FFs are universal, so unique predictions for the cross section of the inclusive production of heavy-flavored hadrons are guaranteed.

The results of this method in the case of X_c production at the energy available at the Tevatron [15, 16] were compared to CDF results and a not so good agreement between theory and experiment was found. The experimental central data points tend to overlap the central theoretical prediction in most of the considered p_T range, but in the lower end of the spectrum, they tend to overshoot the prediction, even by a factor of about 1.5. For all meson

species, the experimental and theoretical uncertainties overlap.

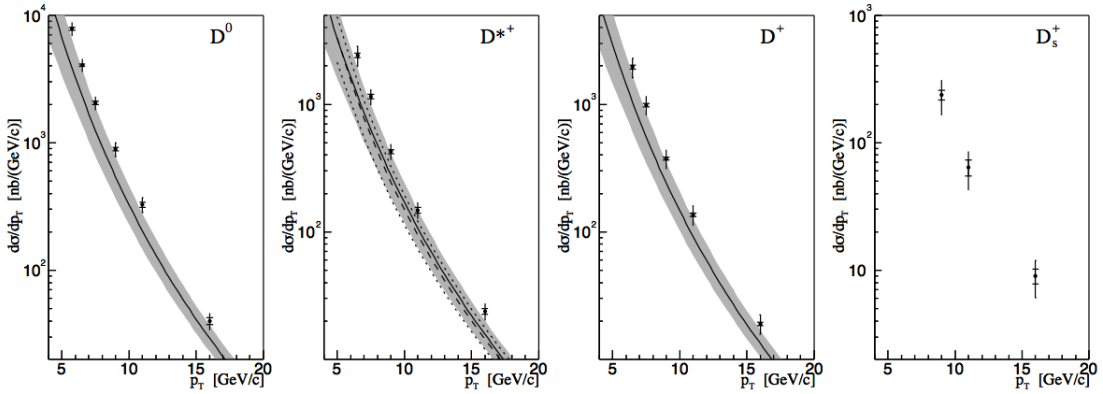

Figure 1.4: The differential cross section measurements for the mesons of the D family at $\sqrt{s} = 1.97$. The inner bars represent the statistical uncertainties; the outer bars are the quadratic sum of the statistical and systematic uncertainties. The solid and dashed curves are the theoretical predictions, with uncertainties indicated by the shaded bands. No prediction was available for the D_S^+ production.

The measurement of the D^0 meson inclusive differential production cross section extended to the low p_T range ($1.5 \leq p_T \leq 9.5$ GeV/c) is going to be published soon. The results of this measurement are shown in Fig. 1.5.

New measurements in the region where α_s becomes too big for perturbative calculation and the color confinement behavior is not well understood are crucial to understand and model non-perturbative QCD. With this work, we want to extend the previous CDF published measurement of $D^0 \to K\pi$ cross section to low p_T and lower center of mass energy, in order to provide an important information about the non-perturbative region.

During the years of operation, the Tevatron collider collected about 10 fb^{-1} of data at $\sqrt{s} = 1.96$ TeV. Before the final shut down, additional scans at lower center of mass energies were performed: $\sqrt{s} = 300$ GeV and $\sqrt{s} = 900$ GeV. To this day, the Tevatron sample with $\sqrt{s} = 900$ GeV is the largest sample at this center of mass energy ever collected in a hadronic collider:

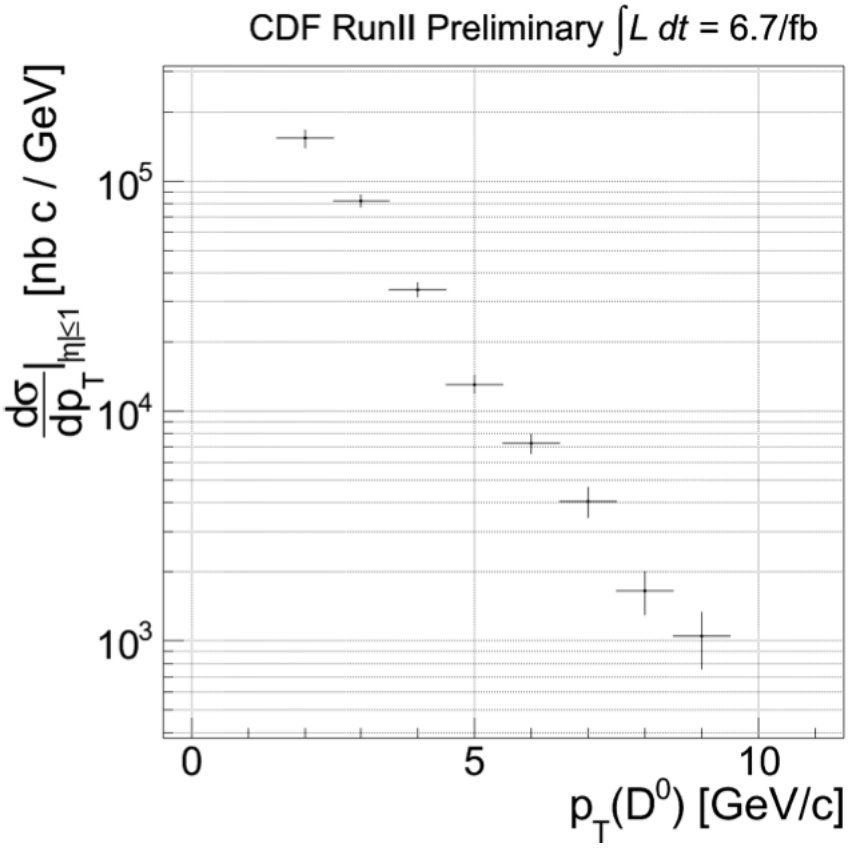

Figure 1.5: D^0 meson inclusive differential production cross section at $\sqrt{s} = 1.97$ TeV as a function of the transverse momentum (only statistical uncertainties are shown).

this give us the chance to perform the measurement of the D^0 production cross section at two different energies.

The Tevatron experimental setup guarantees the uniqueness of this measurement: in fact, even if LHC experiments are able to probe the same p_T range and can run at the same energy, the different initial state means different conditions, implying the possible existence of other processes in the unknown region under exam.

Chapter 2

The Tevatron Collider and the CDF II experiment

2.1 The Tevatron Collider

In the following paragraphs, we will briefly describe the default configuration of the Tevatron Collider. This configuration has been used during almost the whole duration of the Tevatron operation. For this analysis, we used a data sample collected with a special configuration; the differences between the two configurations will be discussed in the next chapter.

The Tevatron Collider is a high energy accelerator located at the Fermi National Accelerator Laboratory (FNAL or Fermilab), about 50 km West from Chicago, Illinois, US.
This collider is a circular superconducting magnets synchrotron, with a 1 km radius. The Tevatron makes bunches of protons (p) collide against bunches of antiprotons ($\bar{p}$) with the same energy: during the years of operation, the Tevatron collected events with a center of mass energy of $\sqrt{s} = 1.96$ TeV, $\sqrt{s} = 1.8$ TeV, $\sqrt{s} = 900$ GeV and $\sqrt{s} = 300$ GeV. In order to reach the final energy in the collision, protons and antiprotons are prepared and accelerated in several steps, which are shown in Fig.2.1.

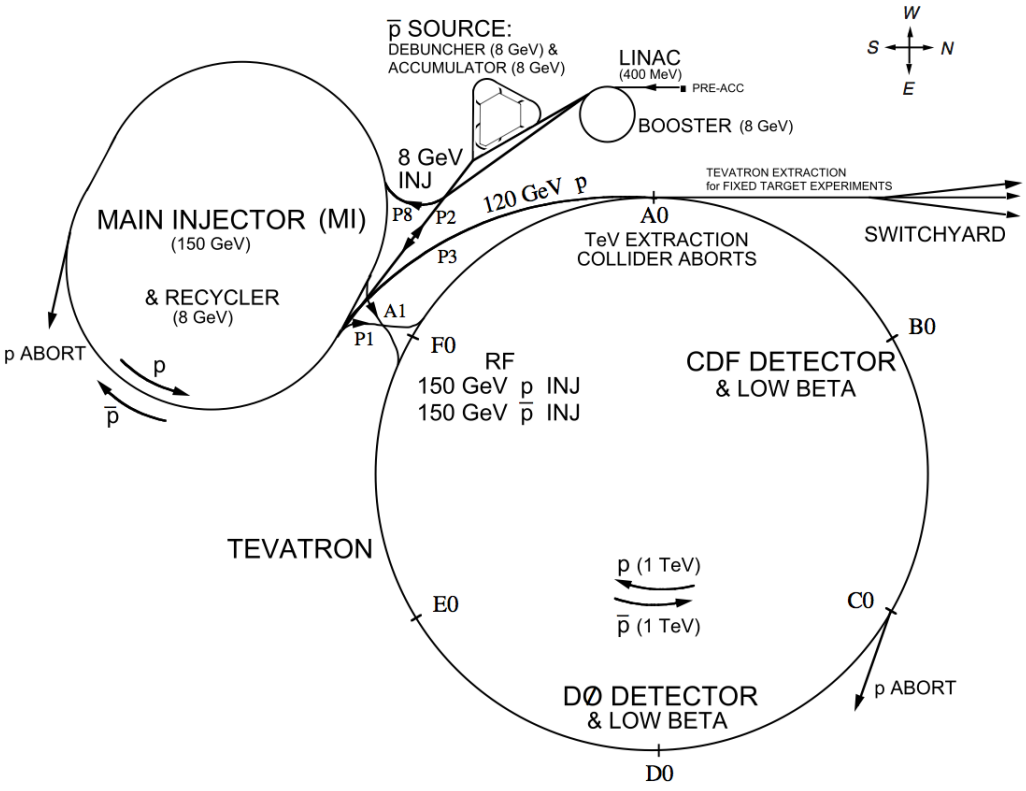

Figure 2.1: View of the Fermilab Tevatron collider.

2.1.1 Luminosity and center of mass energy

The center of mass energy, $\sqrt{s}$, and the instantaneous luminosity, $\mathcal{L}$, are the key parameters that determine the performance of a collider. In the measurement of the cross section of a given process, the luminosity is fundamental because it is the coefficient of proportionality between the rate of the process, R, and its cross section σ:

$$\mathrm{R}\ [\text{events s}^{-1}] = \mathcal{L}\ [\text{cm}^2\text{s}^{-1}] \times \sigma[\text{cm}^2]. \tag{2.1}$$

It is important to notice in equation 2.1 how the rate is achieved: it is the product of σ, which is set by the physics of the process, and $\mathcal{L}$, that is purely due to the machine.

The expected number of events produced, n, in a finite time ΔT is obtained by the time integration of the rate; the cross section is constant in

time, so the introduction of the time integral of the luminosity (*integrated luminosity*) is very usefull, because we can write

$$n(\Delta T) = \sigma \int_{\Delta T} \mathcal{L}(t)\, dt. \tag{2.2}$$

As mentioned above, $\mathcal{L}$ is purely due to the machine, and, assuming an ideal head-on $p\bar{p}$ collision, it is defined as follows in collider experiments:

$$\mathcal{L} = 10^{-5} \frac{N_p N_{\bar{p}} B f \beta_\gamma}{2\pi\beta^* \sqrt{(\epsilon_p + \epsilon_{\bar{p}})_x (\epsilon_p + \epsilon_{\bar{p}})_y}} \mathcal{H}(\sigma_z/\beta^*)\ [10^{30}\mathrm{cm}^{-2}\mathrm{s}^{-1}], \tag{2.3}$$

where N_p and $N_{\bar{p}}$ are the average number of protons ($N_p \approx 2.78 \times 10^{12}$) and antiprotons ($N_{\bar{p}} \approx 8.33 \times 10^{11}$) in a bunch, B is the number of circulating bunches in the ring ($B = 36$), f is the frequency ($f = 47.713$ kHz), ϵ_p and $\epsilon_{\bar{p}}$ are the 95% normalized emittances of the beams ($\epsilon_p \approx 18\pi$ mm mrad and $\epsilon_{\bar{p}} \approx 1\pi$ mm mrad after the injection) and $\mathcal{H}$ is an empiric factor, function of the ratio between the longitudinal r.m.s. width of the bunch ($\sigma_z \approx 60$ cm) and "beta function"[1] calculated at the interaction point ($\beta^* \approx 30$ cm).

The production of $\bar{p}$ has a low efficiency; the creation of collimated $\bar{p}$ bunches and their transfer through the subsequent accelerator stages are difficult: that is why $N_{\bar{p}}$ is the strongest limiting factor of the Tevatron luminosity.

The accessible phase space for the production of resonances in the final state is set by the center of mass energy, $\sqrt{s}$; indeed, $\sqrt{s}$ determines the upper limit for the masses of the particles produced in the $p\bar{p}$ collision.
The highest value of $\sqrt{s}$ reached by the Tevatron Collider is 1.96 TeV. Further details about the Tevatron Collider can be found in [17].

2.1.2 Proton and antiproton beams

The process of protons acceleration develops in gradual stages of acceleration. Gaseous hydrogen is ionized in order to form H^- ions; these ions, after being boosted to 750 keV by a *Cockroft-Walton* accelerator, are injected to

[1] The beta function (or betatron function) is the function that parametrize all the linear properties of the beam.

the *Linac* linear accelerator that increases their energy up to 400 MeV. Then, H^- ions pass through a carbon foil and lose the two electrons. The resulting protons are then injected into a rapid cycling synchrotron, called *Booster*; at this stage protons reach 8 GeV of energy and are compacted into bunches. The next stage of acceleration is the *Main Injector*, a synchrotron which accelerates the bunches up to 250 GeV. In the Main Injector, several bunches are merged into one and used for the injection in the last stage.
The resulting bunches are then transferred to the Tevatron. The protons are forced on an approximately circular orbit by a magnetic field of 5.7 T and they reach the final energy.

Bunches of protons are used also for the production of the antiprotons. When protons bunches in the Main Injector reach 120 GeV, some of them are deviated to a nickel or copper target. Collisions produce spatially wide-spread bunches of antiprotons which are then focused into a beam via a cylindrical lithium lens that separates $\bar{p}$ from other charged interaction products. The bunch structure of the emerging antiprotons is similar to that of the incident protons.
The antiprotons bunches are stored in the *Debuncher* storage ring. In the Debuncher, stochastic cooling stations reduce the spread of the $\bar{p}$ momentum, but a constant energy of 8 GeV is maintained.
At the end of this process, the antiprotons are stored in the *Accumulator* (see Fig. 2.1), where they are further cooled and stored until the cycles of the Debuncher are completed. The $\bar{p}$ are injected into the Main Injector when their current is sufficient to create 36 bunches with the required density. In the Main Injector, the energy of $\bar{p}$ reaches 150 GeV. They are then transferred to the Tevatron where 36 bunches of protons are already circulating in the opposite direction and they reach the final energy.

During the run, the antiproton production and storage does not stop. When the antiproton stack is sufficiently large ($\simeq 4 \times 10^{12}$ antiprotons) and the circulating beams are degraded, the detector high-voltages are switched off, the store is dumped and a new one begins.

The dead time between beam abortion and a new store is typically about

2 hr. During this time, calibrations of the sub-detectors and test runs with cosmics are usually performed.

2.1.3 The luminous region

The $p\bar{p}$ collisions take place at two interaction points: DØ, where the homonym detector is locates, and BØ, home of CDF II. Special quadrupole magnets are located at both extremities of the detectors along the beam pipe in order to maximize the luminosity at the interaction points by reducing the transversal section of the beams. On the longitudinal plane, i.e. along the beam axis, the distribution of the interaction region fits roughly a Gaussian ($\sigma_z \approx 28$ cm) and its center is shifted on the nominal interaction point by the fine tuning of the squeezers. The beam profile in the transverse plane is almost a circumference; its distribution fits roughly two Gaussian with a rms of $\sigma_T \approx 28$ μm.

Only when the beam profile is narrow enough and the conditions are safely stable, the detectors are turned on and the data acquisition starts.

The bunches cross every 396 ns.

The "pile up", i.e. the number of overlapping interactions for each bunch crossing, is a function of the instantaneous luminosity and follows a Poisson distribution (see Fig. 2.2). The average pile up is approximately 10 when the luminosity is at its peak ($\mathcal{L} \approx 3 \times 10^{32}[\mathrm{cm}^{-2}\mathrm{s}^{-1}]$). The luminosity decreases exponentially during the run-time, because of the beam-gas and beam-halo interactions.

2.1.4 Tevatron status

From February 2002 to February 2010, at the center of mass energy $\sqrt{s} =$ 1.96 TeV, about 6.7 fb^{-1} were recorded on tape and the luminosity was, at the beginning of a run, on average about $3.8 \times 10^{32}[\mathrm{cm}^{-2}\mathrm{s}^{-1}]$, with peaks at $4 \times 10^{32}[\mathrm{cm}^{-2}\mathrm{s}^{-1}]$ (See Fig.2.3).

The trend of Tevatron's integrated and initial luminosity as function of

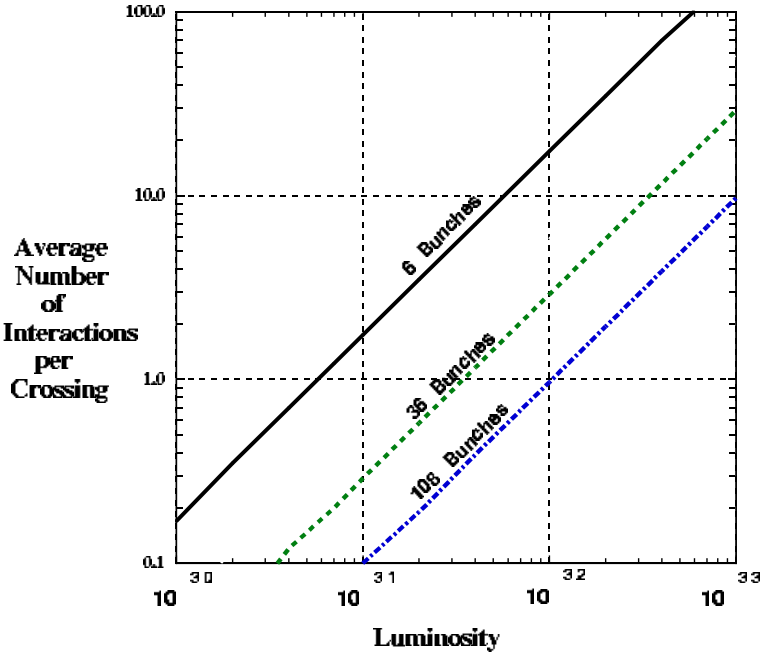

Figure 2.2: Average number of interactions per crossing as a function of the luminosity ($cm^{-2}s^{-1}$) and of the number of bunches circulating in the Tevatron.

store number[2] is shown in Fig. 2.4. The total amount of data collected during the Tevatron activity is about 10.3 fb^{-1} ("acquired" on tape about 8.5 fb^{-1}).

2.2 The CDF II experiment

In the following paragraphs, we will describe the coordinates system and principal notations of the CDF II experiment. An overview of the whole detector and a description of the subtdetectors used in this analysis are then presented.

The CDF II detector is a large multi purpose solenoidal magnetic spectrometer equipped with a tracking system, full coverage projective calorime-

[2]The store number is progressive in time, so the luminosity as a function of the store number is, in practice, the trend of the luminosity over the time.

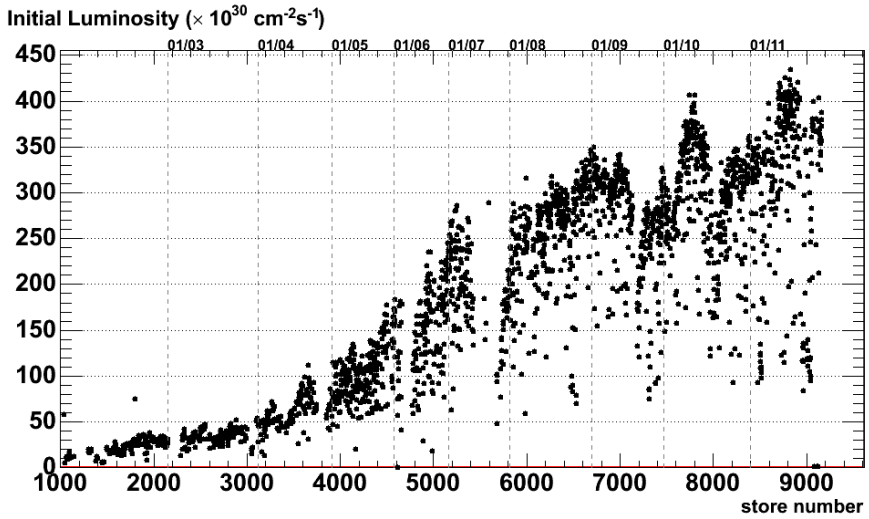

Figure 2.3: Initial luminosity as a function of store number.

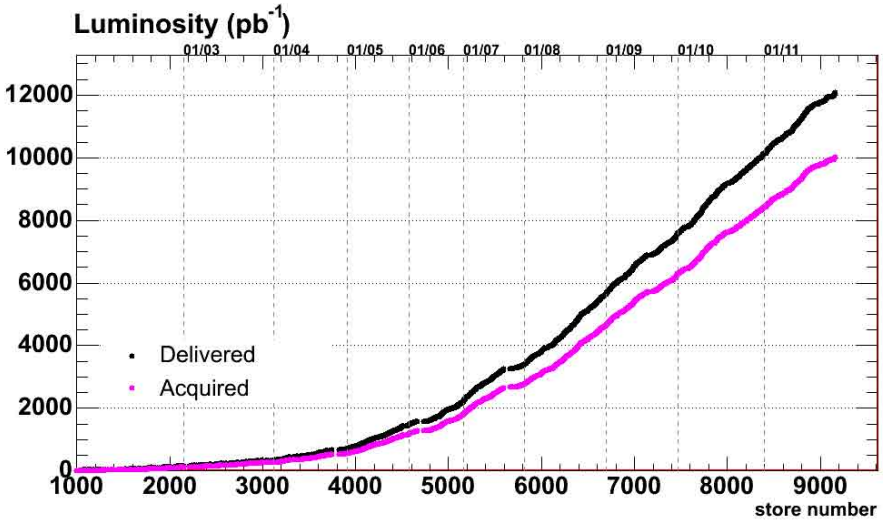

Figure 2.4: Integrated luminosity as a function of store number.

ters and fine-grained muon detectors. The aim of the detector is to determine energy, momentum and, whenever possible, the identity of a broad range of particles produced in the $p\bar{p}$ collisions.

CDF original facility was commissioned in 1985, but the detector has been constantly improved during its activity. After 1995, the operation of the upgraded detector is generally referred to as Run II. Both 2-D and 3-D

representations of CDF II detector are shown in Fig.s 2.5 and 2.6.

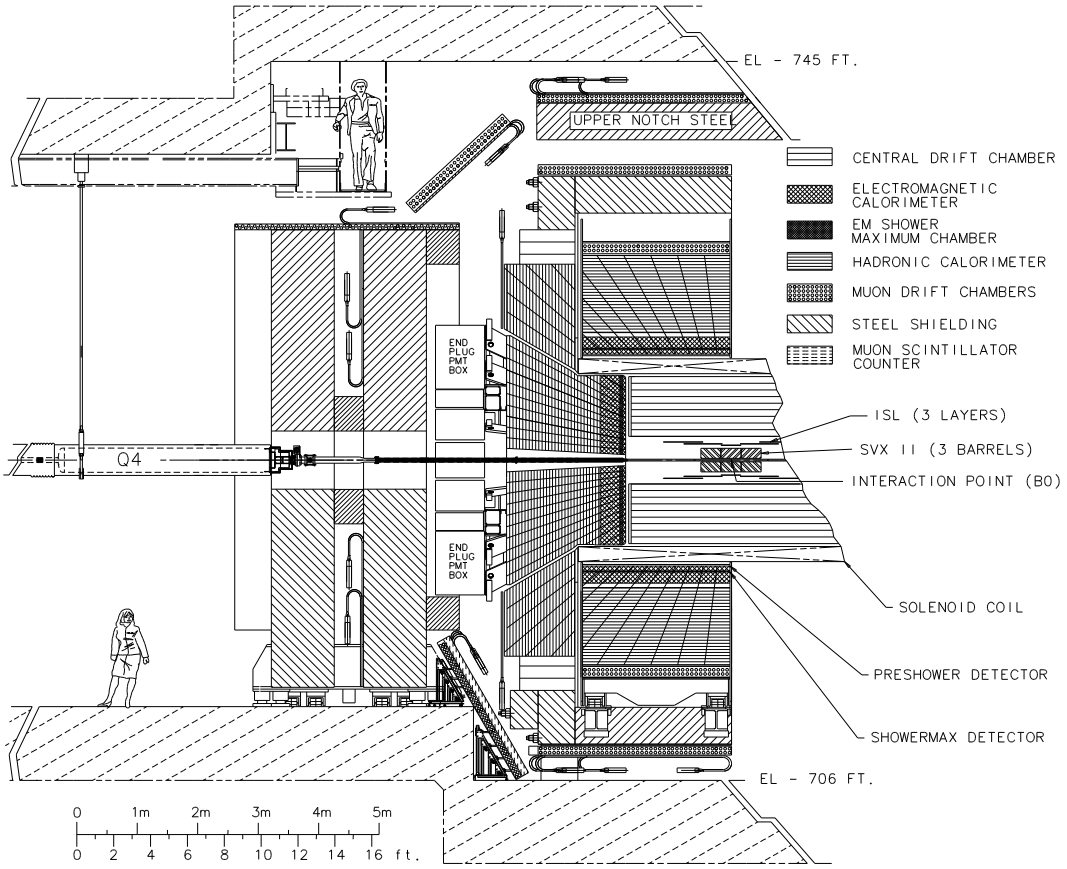

Figure 2.5: View of one half of the CDF II detector in the longitudinal section.

2.2.1 Coordinates system and notations

The Fig. 2.7, shows the right-handed Cartesian coordinates system employed in CDF II. The origin of the frame is assumed to coincide with the BØ nominal interaction point and with the center of the drift chamber.

The proton direction (east) defines the positive z-axis which lies along the nominal beam line. The (x, y) plane is therefore perpendicular to both protons and antiprotons beams. The positive y-axis points vertically upward and the positive x-axis points radially outward with respect to the center of the ring, in the horizontal plane of the Tevatron. Neither the protons

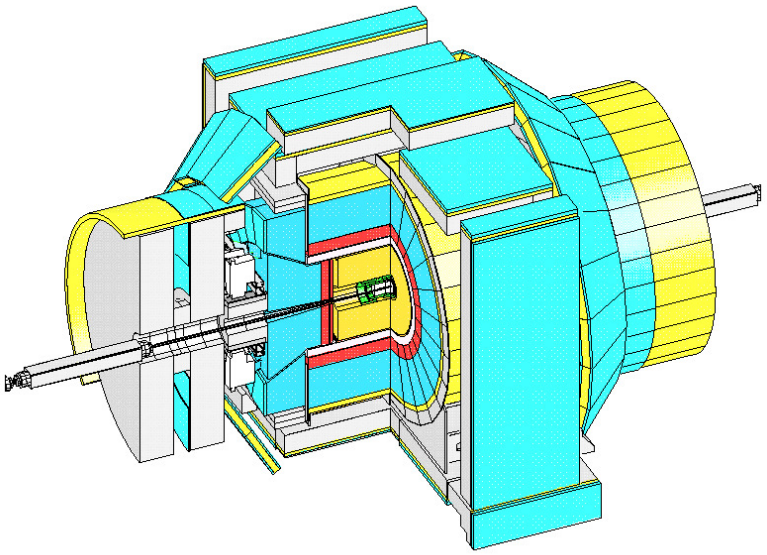

Figure 2.6: 3D view of the CDF II detector.

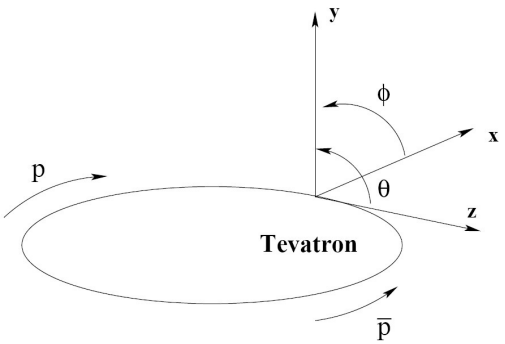

Figure 2.7: CDF II Cartesian coordinates system.

beam nor the antiprotons beam is polarized. As a consequence, the resulting physical observations are invariant under rotations around the z-axis. This invariance makes a description of the detector geometry in cylindrical (r, ϕ, z) coordinates system very convenient. Throughout this thesis,we use the word *longitudinal* to indicate the positive direction of the the z-axis and the word *transverse* to indicate the plane perpendicular to the proton direction, i.e. $(x, y) \equiv (r, \phi)$ plane.

Protons and antiprotons are composite particles, so the actual interaction

occurs individually between their partons, that is between gluons, valence or sea quarks. Even if the energy of the colliding (anti)proton is well know, each parton carries a fraction of the (anti)proton momentum which is not measurable on an event-by-event basis. The momenta of the colliding partons along $\hat{z}$ can be thus very different: as a consequence, the center-of-mass of the parton-level interaction may gain a large speed in the longitudinal component.

In collision experiments, the variable *rapidity* is often used. Rapidity is defined in Eq. 2.4

$$y = \frac{1}{2} \ln \left[\frac{E + p \cdot \cos(\theta)}{E - p \cdot \cos(\theta)} \right], \tag{2.4}$$

where $(E, \vec{p})$ is the energy-momentum four-vector of the particle. Rapidity is invariant under $\hat{z}$ boosts and it can be used as an unit of relativistic phase-space. It transforms linearly under a $\hat{z}$ boost to an inertial frame with speed β. In fact, $y \rightarrow y' \equiv y + \tanh^{-1}(\beta)$, therefore y is invariant since $dy \equiv dy'$. However, from the definition 2.4 it is clear that the measurement of the rapidity requires a detector capable of accurately measuring energy and identifying particles, because of the mass term entering E. In order to put mass out of the equation, when the ultrarelativistic ($p \gg m$) limit is satisfied, it is preferred to use the approximate expression η instead of y, usually valid for products of high-energy collisions:

$$y \xrightarrow{p \gg m} \eta + \mathcal{O}(m^2/p^2), \tag{2.5}$$

in fact, the *pseudo-rapidity* η is only function of θ:

$$\eta = -\ln \tan \left(\frac{\theta}{2} \right). \tag{2.6}$$

As already mentioned, along the z-axis, the actual interaction region is distributed around the nominal interaction point with about 28 cm r.m.s width, so it is necessary to distinguish the *detector pseudo-rapidity*, η_{det}, measured with respect to the (0,0,0) nominal interaction point, from the *particle pseudo-rapidity*, η, measured with respect to the position of the real vertex where the particle originated.

An other commonly used variable is the transverse component of the momentum with respect to the beam axis (p_T)

$$\vec{p_T} \equiv (p_x, p_y) \rightarrow p_T \equiv p \cdot \sin(\theta). \tag{2.7}$$

2.2.2 Detector overview

A comprehensive description of the detector and its subsystems is given in [18].

As one can see in Fig. 2.5, CDF II is an approximately cylindric assembly of sub-detectors. Its dimensions are about 15 m in length, about 15 m in diameter and its weight about 5000 ton.

An accurate description of the final state's particle in energetic hadronic collisions is quantitatively well obtained by the use of (pseudo)rapidity, transverse component of the momentum and azimuthal angle around this axis: this is the reason for the CDF II cylindrical symmetry both in the azimuthal plane and in the *forward* ($z > 0$) – *backward* ($z < 0$) directions.

Each CDF II sub-system is designed to perform a different task. The principal subsystems are listed below from the inner to the outer of the detector:

- Tracking system: it performs the 3-D reconstruction of charged tracks path throught an integrated system consisting of three silicon inner subdetectors and a large outer drift chamber, all contained in a superconducting solenoid.

- Time Of Flight system: it is a cylindrical array made of scintillating bars that allows particle identification via the time of flight method. The TOF is also contained in the solenoid.

- Calorimeters: outside the solenoid, electromagnetic and hadronic calorimeters measure respectively the energy of photons and electrons and

the energy of hadronic particles using the *shower sampling* technique. The basic structure consists of alternating layers of passive absorber and plastic scintillator.

- Muon system: it is CDF II outermost system and performs muons identification. It consists in scintillating counters and drift tubes.

The set of all these components guarantees the possibility of CDF II to perform a wide range of measurements, including high resolution tracking of charged particle, electron and muon identification, low momentum π/K separation, precise secondary vertices proper time measurements, finely segmented sampling of energy flow coming from final state hadrons, electrons or photons, identification of neutrinos via transverse energy imbalance.

Another fundamental feature of CDF II is the capability to monitor the instantaneous luminosity. This is achieved by the use of Cherenkov Luminosity Counters (CLC).

CDF II solenoid produces a solenoidal magnetic field of 1.4 T in the region with $r \leq 150$ cm and $|z| \leq 250$ cm.

The detector is conventionally divided into two main sections of pseudorapidity: the *central region*, where the tracking is contained, and the *forward region*. In the following, if not otherwise stated, we shall refer to the central region as the volume contained in $|\eta_{\text{det}}| < 1$, while the forward region indicates the detector volume comprised in $1 < |\eta_{\text{det}}| < 3.6$.

2.2.3 Tracking system

Fig. 2.8 shows CFD II tracking apparatus: the three-dimensional tracking of charged particle is performed through an integrated system consisting of three silicon inner subdetectors (LØØ, SVX II and ISL) and a large outer drift chamber (COT). These subdetectors are all contained in the superconducting solenoid.

2.2.3.1 Layer ØØ (L ØØ)

The layer of the microvertex silicon detector closest to the beam pipe is Layer ØØ (LØØ) (see Fig. 2.9). It consists of single-sided, radiation-

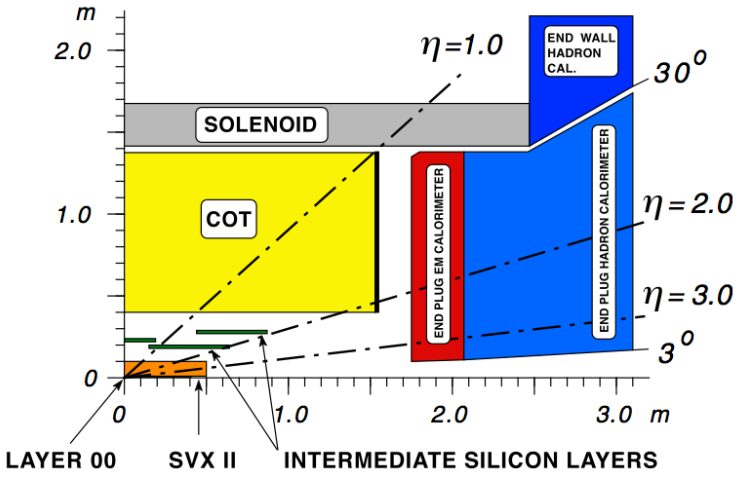

Figure 2.8: Elevation view of one quadrant of the inner portion of the CDF II detector showing the tracking volume surrounded by the solenoid and the forward calorimeters.

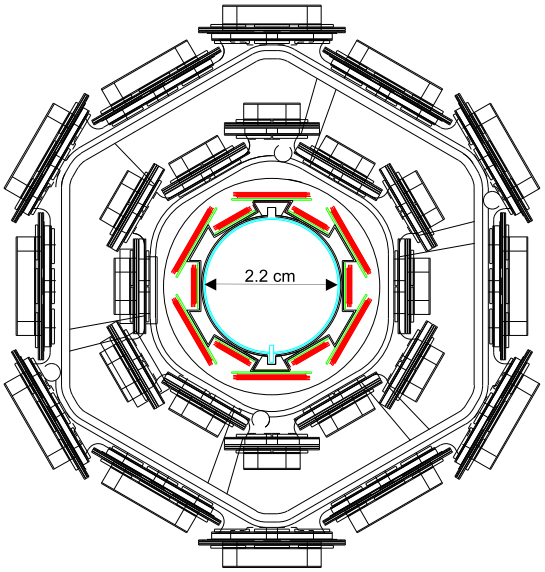

Figure 2.9: LØØ arrangement in transversal view.

tolerant, AC-coupled silicon strip detectors.LØØ covers longitudinally the beryllium beam pipe along 80 cm. Layer ØØ provides excellent coverage with minimal material inside the tracking volume, improving the impact parameter resolution and the B-tagging efficiencies.

The silicon sensors of LØØ can be biased to very high voltages that mantain a good signal-to-noise ratio even after high integrated radiation dose ($\mathcal{O}$(5 MRad)).

The sensors are installed at radii of 1.35 cm and 1.62 cm in direct contact with the beam pipe. The proximity to the beam pipe, which guarantees high resolution measurements of the primary and decay vertexes, is allowed by the radiation hardness of such sensors.

The LØØ strips are located parallel to the beam axis and provide the first sampling of tracks in the $r-\phi$ plane. The resolution of the $r-\phi$ impact point for charged particles is about 10 μm.

The LØØ mass is about $0.01 \cdot X_0$ in the region with the cooling pipes, while it reduces to $0.006 \cdot X_0$ in the region with sensors only.

2.2.3.2 Silicon VerteX detector II (SVX II)

The Silicon VerteX detector II (SVX II) is a fine resolution silicon microstrip vertex detector which provides five 3D samplings of tracks in the transversal region between 2.4 and 10.7 cm from the beam (see Fig. 2.8).

Fig. 2.10a shows SVX II geometry: the detector is cylindrical, coaxial with the beam and segmented along z into three 32 cm long *mechanical barrels*. The total length of 96 cm assures a complete geometrical coverage within $|\eta_{\text{det}}| < 2$.

Each barrel comprises 12 azimuthal wedges each of which subtends approximately 30°. In order to allow the wedge-to-wedge alignment, the edges of two adjacent wedges slightly overlap. Each wedge consists of 5 concentric and equally spaced silicon layers sensors installed at radii 2.45 (3.0), 4.1 (4.6), 6.5 (7.0), 8.2 (8.7) and 10.1 (10.6) cm from the beam as shown in Fig. 2.10b[3].

Independent readout units, called *ladders* host sensors in a layer. Each ladder is composed by two double sided rectangular 7.5 cm long sensors and

[3]Half of the wedges are closer to the beam than the other half because their edges must overlap. The numbers in brackets indicate the distance from the beam of the further wedges' layers.

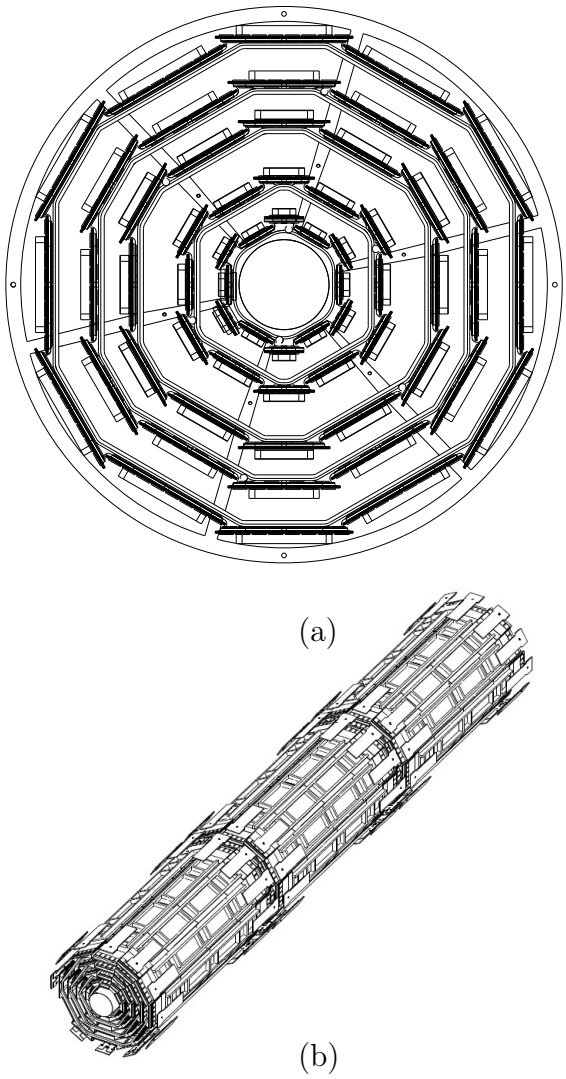

Figure 2.10: (a) SVX II view in the (r, ϕ) plane. (b) view of SVX II three instrumented mechanical barrels.

by the read out electronics unit.

SVX II active surface consists of double-sided, AC-coupled silicon sensors. In each sensor's side, the different possible orientations of strips are three:

- strips oriented parallel to the beam axis, called $r - \phi$ (axial).
- strips rotated by 1.2° with respect to the beam axis, called Small Angle Stereo (SAS).

- strips oriented in the transverse plane, called 90° stereo.

All the five layers have axial strips on one side, three have 90° stereo on the other side and two have SAS strips.

A radiation-hard front-end chip, called *SVX3D*, collects the charge pulse from the strips. Only signals above a threshold are processed: SVX3D operates readout in "sparse-mode". When a channel is over the threshold, the signal of the neighbor channels is also processed in order to cluster the hits.

SVX II single hit efficiency greater than 99% and the measured average signal-to-noise ratio is S/N $\geq$ 10, while the resolutions of the impact parameter for central high momentum tracks are $\sigma_\phi < 35$ μm and $\sigma_z < 60$ μm.

The average mass of SVX II corresponds to $0.05 \cdot X_0$.

2.2.3.3 Intermediate Silicon Layer (ISL)

On the outside of SVX II, an other silicon tracker is placed: the Intermediate Silicon Layer detector, ISL (see Fig. 2.11). ISL covers the polar region of $|\eta_{\text{det}}| < 2$, the same region covered by SVX II.

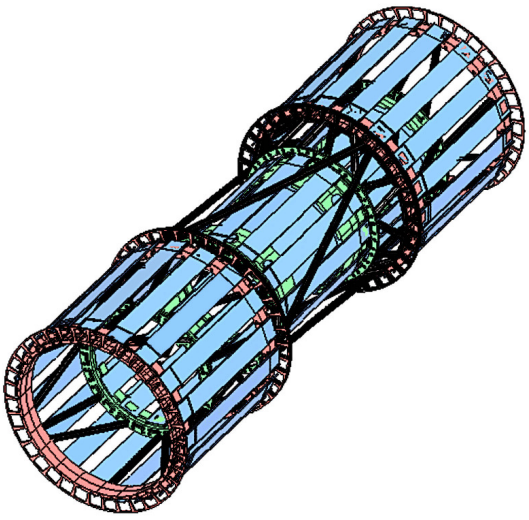

Figure 2.11: View of ISL three instrumented mechanical barrels.

ISL can be roughly divided in three regions: a central region and two forward regions. The central region consists of a single layer of silicon installed over a cylindrical barrel at radius of 22 cm, while the forward regions consist of two layers of silicon installed on concentric barrels at radii of 20 and 28 cm. In order to match SVX II wedge, each silicon layer of ISL is azimuthally divided into 30° wedge.

By analogy with SVX II, ISL basic readout unit is the ISL *ladder*. The main difference between these two types of ladders is that ISL ladder is made with three sensors wire bonded in series, instead of the SVX II two. Thus, the resulting total active length of ISL ladder is 25 cm. ISL sensors are double sided AC-coupled, with axial strips on one side and SAS strips on the other. The sensors dimensions are 5.7×7.5 cm^2 wide and 300 μm thick. As in SVX II, the charge pulse from each strip is read by SVX3D chips.

ISL average mass is $0.02 \cdot X_0$ for normally incident particles.

2.2.3.4 Central Outer Tracker (COT)

Fig.2.12 shows the outermost tracking subdetector of CDF II: a large open cell drift chamber called the Central Outer Tracker (COT).

The COT is a cylindrical detector, coaxial with the beam and it extends radially, within the central region, between the radius of 40 cm and 138 cm from z-axis.

The chamber contains 96 radial layers of wires arranged into 8 *superlayers* (SL), see Figure 2.12. Each SL contains 12 sense wires (anode) spaced 0.762 cm apart, so it samples the path of a charged particle at twelve radii. The wires of the 8 SL are not oriented all in the same way: in order to reconstruct the path of a charged particle in the $r - z$ volume, the wires of four SL are oriented parallely to the beam axis (*axial* SL) and the wires of the remaining four SL are oriented either +3° or -3° with respect to the beamline (*stereo* SL). The axial SL are radially interleaved with the stereo SL.
Each superlayer is azimuthally segmented into open drift cells. Figure 2.13 shows the view of a drift cell: a row of 12 sense wires alternating with 13 potential wires. The potential wires optimize the electric field intensity in the SL controlling the gain on the sense wires. The field panel closes the

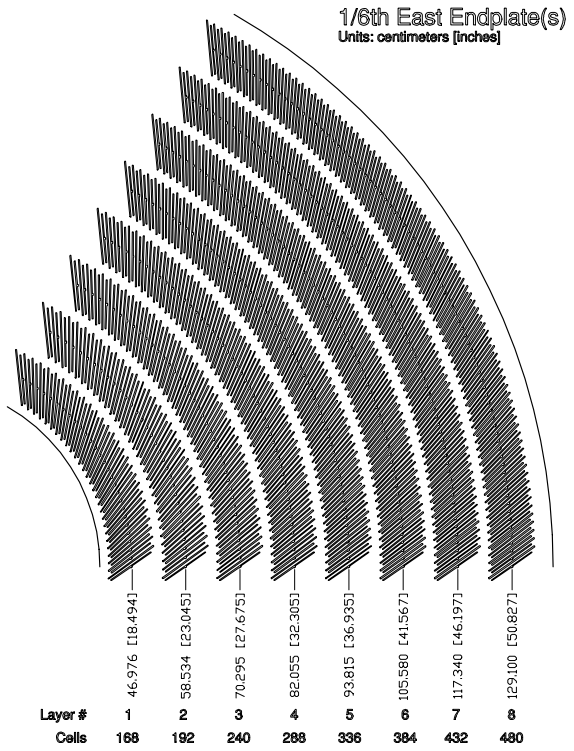

Figure 2.12: A 1/6 section of the COT end-plate. The enlargement shows in details the slot were wire planes (sense) and field sheet (field) are installed.

cell along the azimuthal direction and defines the fiducial volume of a cell: it is the cathode of the detection circuit. Mylar strips carrying field-shaping wires, called *shaper panels*, close mechanically and electrostatically the cells at the radial extremities. The electric field strength in the cell is 2.5 kV/cm.

In the chamber, the crossed electrical and magnetic field as well as the characteristics of the gas mixture cause an angular shift of the particle drift path. In order to balance this shift, the wire planes are 35° azimuthal tilted with respect the radial direction. The tilted-cell geometry shows other benefits: the calibration of the drift-velocity is easier and the left-right ambiguity for tracks coming from the origin is removed. An overview of the COT main characteristics is presented in Tab 2.1.

A preamplifier shapes and amplifies the analog pulses from the COT sense wires. To perform the dE/dx measures, the discriminated differential output

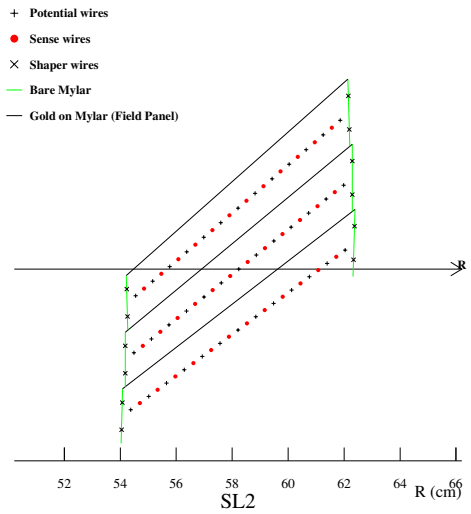

Figure 2.13: A view of an axial section of three cells in super-layer 2. The arrow shows the radial direction.

Gas Mixture	Ar(50%)/Ethane(35%)/CF_4(15%)
Electron drift speed	about 100 μm/ns
Maximum drift time	about 100 ns
Track efficiency	99%
Single hit resolution	$\sigma_{\text{hit}} \simeq 140$ μm
p_t resolution	$\sigma_{p_T}/p_T^2 \simeq 0.0015$ c/GeV
Mass	0.016 $\cdot X_0$ for normally incident particle

Table 2.1: COT characteristics.

is used because it encodes charge information in its width. A TDC is used to record the leading and trailing edges of the signals in 1 ns bins.

2.2.3.5 Tracking performance.

In the tracking system, a uniform axial magnetic field is present, so the trajectory of a charged particle produced in the interaction point with non-zero velocity is described by an helix with the axis parallel to the magnetic field.

Fig. 2.14 shows a view of the helix parametrization, which requires the definition of five parameters:

- C: signed helix half-curvature, defined as $C \equiv \frac{Q}{2R}$, where Q is the sign of the electric charge of the particle and R is the radius of the helix. The relation between C and the transverse momentum is: $p_T = \frac{cB}{2|C|}$ (where B is the intensity of the magnetic field).
- φ_0: direction of the track at the point of closest approach to the beam.
- d_0: signed impact parameter, i.e. the distance between helix and the origin at closest approach, defined as

$$d_0 \equiv Q \cdot (\sqrt{x_c^2 + y_c^2} - R), \tag{2.8}$$

  where (x_c, y_c) are the coordinates of the primary vertex of interaction in the transverse plane.
- $\cot(\theta)$: cotangent of the polar angle at closest approach distance. This is directly related to the longitudinal component of the momentum: $p_z = p_T \cdot \cot(\theta)$.
- z_0: z position of the point of closest approach to the origin.

The trajectory of a charged particle satisfies the following equations:

$$x = r \cdot \sin(\varphi) - (r + d_0) \cdot \sin(\varphi_0) \tag{2.9}$$

$$y = -r \cdot \cos(\varphi) + (r + d_0) \cdot \cos(\varphi_0) \tag{2.10}$$

$$z = z_0 + s \cdot \cot(\theta) \tag{2.11}$$

where s is the projected length along the track, $r = 1/2C$ and $\varphi = 2Cs + \varphi_0$.

When a charged particle passes through the tracking system, the detector reconstructs, along the physical trajectory of the particle, a set of spatial measurements ("hits") by clustering and pattern-recognition algorithms. In

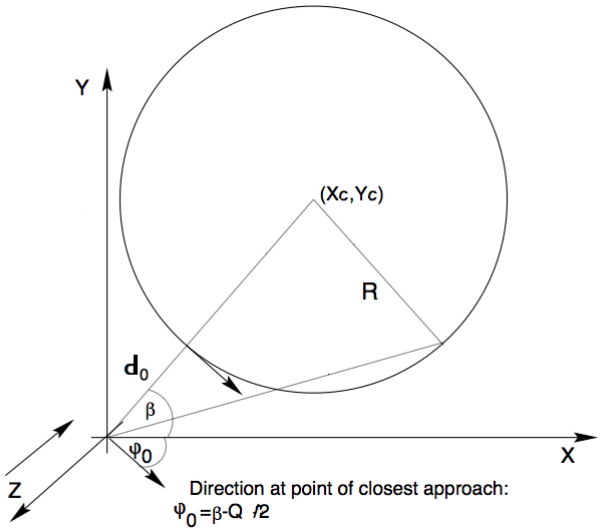

Figure 2.14: View of the helix parametrization

order to reconstruct the trajectory, the hits are fitted with a helical fit, which determines the five above parameters and finally define a "track" object. The helical fit takes into account non-uniformities of the magnetic field and scattering in the detector material.

Only tracks reconstructed with both silicon and COT hits (*SVX+COT* tracks) were used for this analysis. The track fitting for all SVX+COT tracks starts with the fit in the COT: the fit is then extrapolated inward to the silicon. In the COT the track density is lower than in the silicon, because of its greater radial dimension, consequently the probability of hits accidental combination in the track reconstruction is smaller. This way of performing the fit is fast and efficient; the resulting tracks have high purities.

COT performance. The COT efficiency for tracks is typically 99% and all the COT channels worked properly until the last the Tevatron run. Cosmic rays are exploited to mantain the internal alignments of the COT cells within 10 μm. The wires mechanical curvatures effects due to gravitational and electrostatic forces are kept under control within 0.5% by equalizing the

difference of E/p between electrons and positrons as a function of $\cot(\theta)$. The single-hit resolution is about 140 μm, including a 75 μm contribution from the uncertainty on the measurement of the $p\bar{p}$ interaction time. The typical resolutions on track parameters for tracks fit with no silicon information or beam constraint are listed in Tab 2.2

resolution	value
σ_{p_T}/p_T^2	0.0015 c/GeV
σ_{φ_0}	0.035°
σ_{d_0}	250 μm
σ_θ	0.17°
σ_{z_0}	0.3 cm

Table 2.2: COT resolution on track parameters.

Performance with the silicon detectors. The reconstruction of the hits in the silicon detector is fundamental to improve the impact parameter resolution of tracks. In fact, with the measure in the silicon, the resolution may reach $\sigma_{d_0} \approx 20$ μm (not including the transverse beam size)[4]. This value and the value of the transverse beam size ($\sigma_{\mathrm{T}} \approx 28$ μ) are ones of the most important factors for the study of the transverse decay-lengths of heavy flavors. In fact, these resolutions are sufficiently small with respect to the typical transverse decay-lengths (a few hundred microns) to allow separation between the decay vertices and the primary vertices of the collisions.

With the use of the silicon tracker, also the stereo resolutions are improved up to $\sigma_\theta \approx 0.06°$, and $\sigma_{z_0} \approx 70$ μm. On the contrary, the transverse momentum and the azimuthal resolutions remain approximately the same of COT-Only tracks.

2.2.4 Other CDF II subdetectors

For an accurate description of the CDF II subdetectors not used in this analysis (TOF system, calorimeters and muon system) see [18].

[4]The smallness of σ_{d_0} depend on the number and radial distance of the silicon hits.

2.2.5 Cherenkov Luminosity Counters (CLC)

The luminosity ($\mathcal{L}$) is a fundamental parameter to measure the physical processes cross sections.

Given the the average number of inelastic interactions per bunch crossing ($< N >$), the luminosity is inferred according to:

$$\mathcal{L} = \frac{< N > \cdot f_{\text{b.c.}}}{\sigma_{TOT}} \tag{2.12}$$

where $f_{\text{b.c.}}$ is the bunch-crossing frequency and σ_{TOT} is the total $p\bar{p}$ cross-section at $\sqrt{s} = 1.96$ TeV. $f_{\text{b.c.}}$ is precisely known from the Tevatron radio frequency. The total cross section at $\sqrt{s} = 1.96$ TeV is calculated from the averaged CDF and E811[5] luminosity-independent measurements at $\sqrt{s} = 1.8$

[5]E811 is an experiment about p-$\bar{p}$ elastic scattering, situated at hall EØ of the Tevatron beam line.

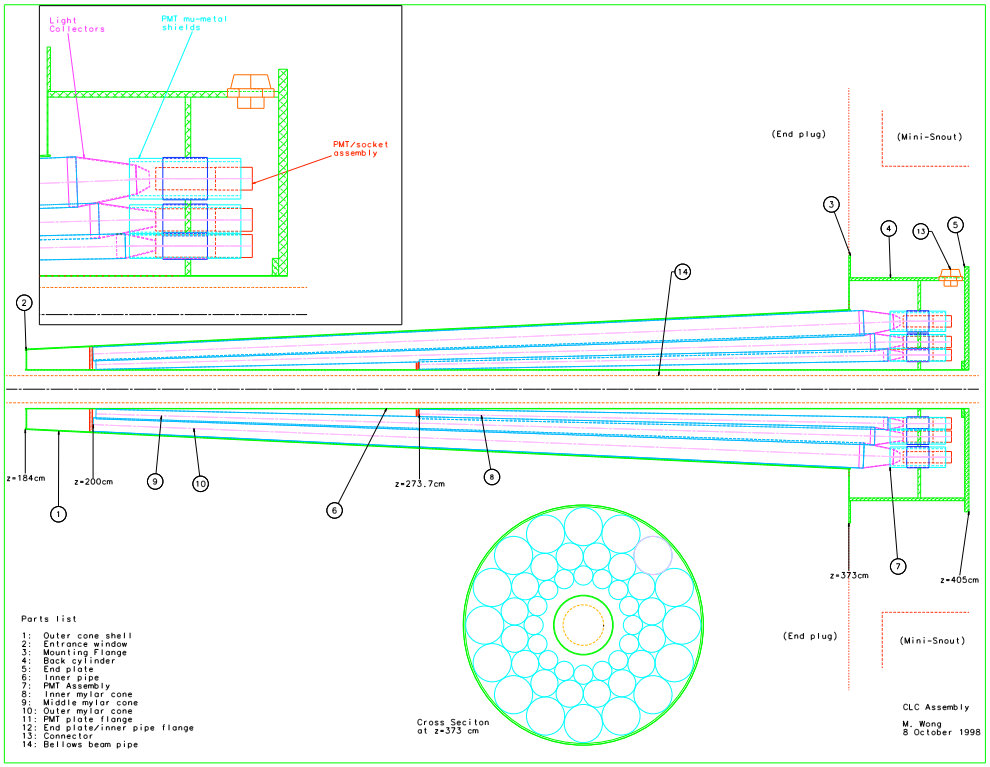

Figure 2.15: Views of the CLC system in the longitudinal and transverse plans.

TeV [19, 20] and extrapolated to $\sqrt{s} = 1.96$. Its value is $\sigma_{TOT} = 81.90 \pm 2.30$ mb [21].

The measurement of $< N >$ is performed at CDF through the Cherenkov Luminosity Counters (CLC). These sub-detectors are two separate modules, symmetrically placed in CDF II forward and backward regions: they cover the $3.7 \leq |\eta_{\rm det}| \lesssim 4.7$ range (see Fig. 2.15).

Each module is composed by conical Cherenkov counters arranged in three concentric layers around the beam-pipe. The Cherenkov counters point to the nominal interaction region; they are 48 thin, 110–180 cm long, filled with isobutane.

CLC Cherenkov angle, $\theta_C = 3.4°$, determines the momentum thresholds for light emission: 9.3 MeV/c for electrons and 2.6 GeV/c for charged pions. In the CLC, the signal due to the $p\bar{p}$ interaction is generally larger than the signal due to the beam halo or to secondary interactions because prompt charged particles from the $p\bar{p}$ interaction are more likely to walk through the full counter length. Moreover, different particle multiplicities entering the counters cause distinct peaks in the signal amplitude distribution. For this reasons, the CLC measurement of $< N >$ has 4.4% relative uncertainty in the luminosity range $10^{31} \leq \mathcal{L} \leq 10^{32}$ [cm^{-2}s^{-1}]. Combining this accuracy with the relative uncertainty on the inelastic $p\bar{p}$ cross-section, one finds that the instantaneous luminosity is inferred with 5.8% relative uncertainty.

2.2.6 Trigger and Data AcQuisition (DAQ) system

An event is written on tape when at least one of the CDF II triggers fires. Events are grouped into *runs* that are progressively labeled with a *Run Number*; a run is a period of continuous operation of the CDF II Data Acquisition (DAQ).

Starting from partial information provided by the detector in real time, the trigger system discards the uninteresting events. The production cross section of physics of interest is way smaller than the total $p\bar{p}$ inelastic one. The task of separating the great majority of background events from the

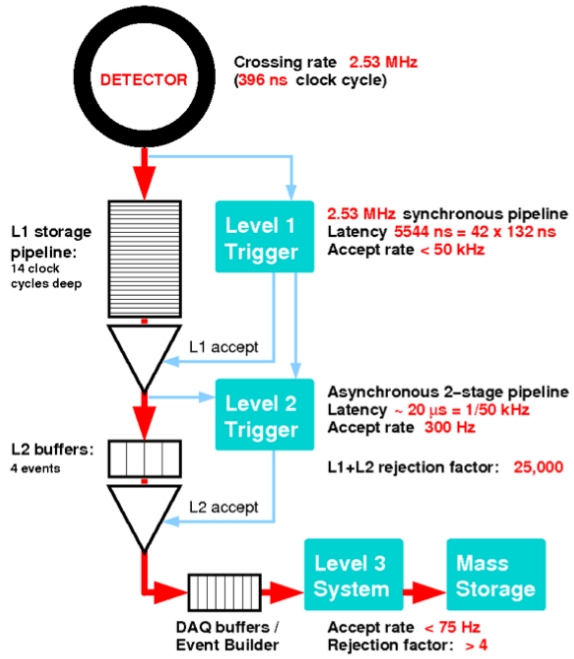

Figure 2.16: Functional block diagram of the CDF II system.

fraction of interesting events is fundamental.

The writing of events on permanent memories has a maximum rate of about 100 Hz, while the Tevatron has an average collision rate of about 1.7 MHz, due to the 396 ns interbunch spacing; the CDF II trigger reduces this acquisition rate, without losing the majority of events with a physical interest.

The CDF II trigger is a multi-stage system: it is divided into three levels, as one can see in Fig. 2.16. Each level has more accurate detector information and more time for processing than the previous one; thus, it can choose whether discarding the event received from the previous level or sending it to the next level. The detector front-end electronics sends data directly to Level-1; an event is permanently stored to memory if it passes the Level-3.

The read-out of the entire detector takes about 2 ms on average. When the trigger is busy processing an event, it cannot record other events: this causes the so called *trigger deadtime*. At the maximum luminosity, the percentage of events rejected because of the trigger deadtime is around 5%.

2.2.6.1 Level 1 (L1)

Level 1 (L1) stage has the same clock of the Tevatron (about 1.7 MHz).A fully pipelined front-end electronics for the whole detector is employed: every 396 ns, the buffer of a 42-cell long pipeline is written with the signal of each CDF II channel. This method gives L1 more time to make its decision before the buffer is cleared and the data are lost: 396×42 ns $\simeq$ 16 μs.

L1 makes its decision processing on a simplified subset of data. A custom-designed hardware reconstructs coarse information from the COT, the calorimeters and the muon system, using three parallel streams. For each event, two-dimensional tracks in the transverse plane, the total energy and and the presence of muon are identified; these physical objects are called "primitives", because of their low resolution.

In the decision stage, the information from the "primitives" is analyzed and more sophisticated objects, like muons, electrons or jets are formed.

The COT channels are processed by the eXtremely Fast Tracker (XFT). In time with the L1 decision, XFT custom processor identifies two-dimensional tracks in the (r, ϕ) plan of the COT. In order to do so, short segments of track are firstly identified by a pattern matching. Then, if a coincidence between segments crossing four super-layers is found, they are linked together into full-length, two-dimensional tracks. The pattern matching consists in comparing a possible segment with a set of about 2,400 predetermined patterns. These patterns are determined by the correspondence to all tracks with $p_T \gtrsim$ 1.5 GeV/c originating from the beam line.

At $\mathcal{L} \approx 10^{32}$ [cm^{-2}s^{-1}], the track-finding efficiency and the fake-rate with respect to the off-line tracks are measured to be respectively 96% and 3% for tracks with $p_T \gtrsim 1.5$ GeV/c. Of course, this parameters depend on the instantaneous luminosity. For these 2-D tracks, the observed momentum resolution is $\sigma_{p_T}/p_T^2 \approx 0.017$ c/GeV.

To keep or to reject an event, different combinations of requirements on the reconstructed objects can be submitted to L1.

2.2.6.2 Level 2 (L2) and Level 3 (L3)

The Level-2 (L2) trigger fulfills two subsequent tasks, the *Event building* and the *Decision*.
L2 detector information is more complete than L1 detector information; thus, the Event building reconstructs the event with L2 information. The Event building process in parallel the calorimetric information and the tracking information. Its clock is 10 μs.

Decision combines the outputs from L1 and L2 in order to decide whether or not an event is sent to Level-3.
The maximum decision-making time (*latency*) of L2 is 20 μs for each event and the output rate is about 300 Hz.

Level-3 (L3) is exclusively software-based. At L3, the events selected by L2 are reconstructed, with full detector resolution. L3 codes and the offline reconstruction codes are very similar to each other.

About 191 *trigger paths* can be implemented at L3: the trigger path is the tool to define any particular sequence of L1, L2 and L3 selections. An event that satisfied all the 3 levels requests is flagged with a particular trigger path. Two events with different trigger paths fulfill different level requests, even if same level request can be used by the two trigger paths.
Once the event is fully reconstructed and the integrity of its data is checked, L3 decides whether or not the event is written on tape.
The size of an event is typically about 150 kbytes. The maximum storage rate is about 20 Mbyte/s.
At the end of the three stages, the event output rate is about 75 Hz.

2.2.7 Operations and data quality

During the runs, the operation of the detector and the quality of the on-line data taking was continuously controlled.

The main causes of data taking inefficiencies are two. At the beginning of the runs, the detector was not empowered since the beam was proved to be stable. In addition, problems related to trigger dead time, to detector or

to DAQ may occur. The average data-taking efficiency was about 85%.

Quality inspections were applied on each run in order to guarantee homogeneous data-taking conditions. The running condition must undergo some physics-quality standards; for these reasons, the fractions of data valid for physics analysis were certified for each run.

The data-taking was immediately stopped if a malfunction of the detector was registered. Then, corrupted data are more likely contained in very short runs that are usually excluded on-line from physics analysis.

The CLC were operative during the whole data-taking of the physics-quality data, thus an accurate integrated luminosity measurement has been guaranteed; a set of luminosity and beam-monitor probe quantities were constantly controlled to be within the expected ranges during the data taking. On-line, shift operators ensured that L1, L2 and L3 triggers work correctly. The operators also controlled other higher level quantities to be within the expected ranges.

After the recording on tape of the data, all the data manipulations are referred to as *off-line* processes.

2.2.8 Event reconstruction and analysis framework

The events collected by the DAQ and the simulated samples are stored on tapes and analyzed with the *Production* reconstruction program.

The production process is the main off-line operation: high-level physics objects (e.g. tracks, vertices, muons, electrons, jets, etc.) are reconstructed by a centralized analysis from low-level information (e.g hits in the tracking subdetectors, muon stubs, fired calorimeter towers, etc.).

Precise information about the detector such as calibrations, beam-line positions, alignment constants, masks of malfunctioning detector-channels, etc. etc. and more sophisticated algorithms are available during the production. After the production, the size of an event typically increases of the 20% because of the added information.

The production processing of all the data sets has been repeated every time that improved detector information or new reconstruction algorithms became

available.
Off-line, the exclusion of runs with software crashes during the production or with generic problems takes place.

Analysis groups creates a set of ntupes in order to reduce the total amount of data to a smaller data-set of interest.

The ROOT framework [24] is used to create these ntuples. The ROOT framework is a tool of analysis written in C++ and commonly used by several HEP experiments; it is the same environment used for all the analyses preformed at CDF.

The ntuples used in this work are the Standard Ntuples (Stntuples) that are used by the QCD group by default. Stntuples contains the events collected by the triggers suitable for this analysis.

Chapter 3

Data selection

3.1 Low energy scans

With a view to the final shut down, the Tevatron collider performed a series of scans at lower center of mass energies, especially addressed to QCD studies.

The data taking lasted a week and collected data at two different center of mass energies: $\sqrt{s} = 900$ GeV and $\sqrt{s} = 300$ GeV. The sample at the energy of $\sqrt{s} = 900$ GeV is the largest sample ever collected at a hadronic collider in these experimental conditions; these are the data used for the present analysis.

The main features of these runs operation remained the same as the default operation, but some configuration were changed. The number of bunches per run was decreased to 3 bunches of protons and 3 bunches of antiprotons. The instantaneous luminosity decreased as well. The decreasing of the luminosity entails a diminishing of the pile up: for the low energy runs the pile up is approximately zero. In addition, the trigger tables were optimized for QCD studies in these new configurations.

3.1.1 Luminosity

As described in Sec. 2.2.5, the rate of the inelastic $p\bar{p}$ events measured by the CLCs provides the instantaneous luminosity.

The CLCs measure the average number of primary interactions, $< N >$;

this quantity is related to the instantaneous luminosity $\mathcal{L}$ as stated in Eq. 2.12. In the low energy scan, the Tevatron average bunch crossing rate $f_{b.c.}$ is about 48 kHz, while the total $p\bar{p}$ cross section at the energy of 900 GeV is determined according to data provided by the Particle Data Group [4, 25].

The total, elastic and inelastic cross sections at the energy of 900 GeV are listed in Tab. 3.1. At this center of mass energy, the total cross section is estimated by performing a linear interpolation [21].

$\sqrt{s}$	900 GeV
$\sigma_{el.}$ (mb)	$13.7 \pm 1.4 \pm 0.0$
$\sigma_{inel.}$ (mb)	$51.6 \pm 1.6 \pm 2.3$
σ_{TOT} (mb)	$65.3 \pm 0.7 \pm 2.3$

Table 3.1: Elastic, inelastic and total cross section for $p\bar{p}$ scattering at $\sqrt{s} =$ 900 GeV [25]. The first uncertainty is statistical, the second systematic.

3.2 Online

The events used in this analysis are collected with the `ZEROBIAS` (ZB) and the `MINBIAS` (MB) trigger paths; the features of these trigger paths are described in detail in the following sections. With these two paths, no trigger-related bias is introduced in the measured variables. On the contrary, in the published CDF measurement of the D^0 cross section [10], a trigger selection with hard requests in terms of the transverse momentum of the decay products was used: because of this bias, the minimum $p_T(D^0)$ was set to 5.5 GeV/c.

3.2.1 Zero Bias trigger

The first trigger path used to collect events for this analysis is the `ZEROBIAS`. Any bunch crossing fires L1, but its rate is reduced by a prescale factor to limit its output to disk. No further requests are applied at L2 and L3. This trigger path do not use any CDF II sub-detector to fire; L1 fires whether or not a hard scattering collision occurs. The data taking depends exclusively on the Tevatron bunch crossing frequency. The combination of the prescale

factor and the bunch cross rate gives a final output rate at L3 of about 50 Hz. About 6.6 millions of events were collected by this path.

3.2.2 Minimum Bias trigger

The second path used is `MINBIAS`. Unlike the `ZEROBIAS`, the `MINBIAS` requires at least an inelastic $p\bar{p}$ collision to trigger an event. At L1, Cherenkov Luminosity Counters (CLC) are exploited to check if a collision occurs: `MINBIAS` requires the coincidence of a signal[1] in at least one East CLC and one West CLC. No further requests are applied at L2 and L3.
The output rate at each trigger level is limited by prescale factors: their combination gives a final output rate at L3 of about 400 Hz.
About 46.6 millions of events are collected by this path.

3.2.3 Samples overlap

During the data taking, all CDF trigger paths operate at the same time; then, events might be triggered by both our paths, appearing twice in the data sample. However, considering the effect of the prescale, the sample overlapping has a negligible effect on our analysis key variables with respect to their uncertainties; we find an overlap of the order of one event every 10,000. Our analysis checks for these occurrences and filters out the duplicate events.

3.3 Offline

3.3.1 Good Run List

In Sec. 2.2.7 we described the standard CDF data-quality requirements that define which runs can be used for physics analyses. The "good" runs are grouped in the so called Good Run List (GRL).
Several GRLs are released by the analysis groups, depending on which subdetectors properly worked during the data-taking. The official list that contains only runs where SVX II and the COT were working properly is used for

[1] The minimum threshold for claiming a CLC signal is 250 ADC counts.

this analysis, because only SVX+COT tracks were employed. In fact, on one hand COT stand-alone tracking do not provide a sufficient impact parameter resolution of our aim; on the other hand, silicon stand-alone tracking is useful in the region $1 \leq |\eta| \leq 2$, where the COT coverage is incomplete. In this analysis, however, we reject tracks with $|\eta| > 1$, because the reconstruction efficiency is too low. In the central region of interest, only track with a p_T < 0.28 GeV/c have SVX-Only informations, but this p_T value is well below our minimum request.

The ZB and MB sample are reduced after the GRL request: to about 6.0 millions (ZB sample) and to about 42.0 millions (MB sample).

3.4 $D^0 \to K\pi$ at CDF II

The aim of this work is to identify the signal of the D^0 mesons decay in the channel $D^0 \to K\pi$; with this notation, we consider both the charged conjugated: $D^0 \to K^-\pi^+$ and $\bar{D}^0 \to K^+\pi^-$. This is the first step to measure the differential production cross section, defined as follows:

$$\frac{d\sigma_{D^0 \to k\pi}}{dp_T}(p_T; |y| \leq 1) = \frac{\frac{N_{D^0}+N_{\bar{D}^0}}{2}(p_T)}{\mathcal{L} \cdot \epsilon_{trig} \cdot \epsilon_{rec}(p_T) \cdot Br(D^0 \to K\pi)}\Big|_{|y|\leq 1} \tag{3.1}$$

where:

- N_{D^0} and $N_{\bar{D}^0}$ are the yields of the D^0 and $\bar{D}^0$ signals. Experimentally, we count the sum of D^0 and $\bar{D}^0$ yields. We assume charge invariance in the production process through strong interaction, thus the cross section for D^0 mesons only is the average cross section for D^0 and $\bar{D}^0$ mesons.
- $|y| \leq 1$ is the range of rapidity considered.
- $\mathcal{L}$ is the integrated luminosity of the data sample.
- ϵ_{trig} is the trigger efficiency.

- ϵ_{rec} is the global efficiency of the reconstruction of our candidates. This parameter accounts for the geometrical and kinematical acceptances as well as the detector reconstruction efficiency of the signal.
- $Br(D^0 \to K\pi)$ is the decay branching ratio of the channel studied.

We refer to the decay products, K and π, as the D^0 "daughters".

3.4.1 Measurement strategy

The $D^0 \to K\pi$ channel represents one of the simplest topology that we can study at CDF II to detect this charmed neutral meson: $D^0 \to K\pi$ has a relatively high branching ratio (about 3.9 %) and it is fully detected by the tracking system (the daughters are two charged particles). We are then able to identify this heavy meson concealed by a background of light particles (mainly pions and kaons) several orders of magnitude larger.

To unfold the D^0 signal from the background we apply the following procedure for each event:

- apply quality requirements on the tracks, in terms of hits produced inside the tracking system (see Sec. 6.1) to reduce the contamination of fake reconstructions;
- combine together all the possible couples of the selected tracks with opposite charges;
- require geometrical conditions between the two considered tracks to reduce the combinations coming from unrelated tracks;
- fit the tracks' helices looking for an intersection point. If the fit returns a possible common origin for them, a D^0 **candidate** is defined;
- select only candidates with a decay vertex displaced from the primary vertex of interaction (to reduce the combinatorial background) and in the rapidity region of interest.

We then evaluate the candidate's invariant mass and study its distribution for all the candidates found in the sample; we search a signal at the expected D^0 mass (about 1.864 GeV/c^2). More details of the measurement strategy will be described in Sec. 6.1.

3.4.2 $D^0 \to K\pi$ topology

The D^0 lifetime is $\tau \sim 410 \cdot 10^{-15}$ s, that correspond to a decay length of $c\tau \sim 123\ \mu m$. Thus, the D^0 travels a path, away from the primary vertex of the $p\bar{p}$ collision that originates it, that is measured thanks to the resolution of the silicon tracker SVX II (see Section 2.2.3.2).

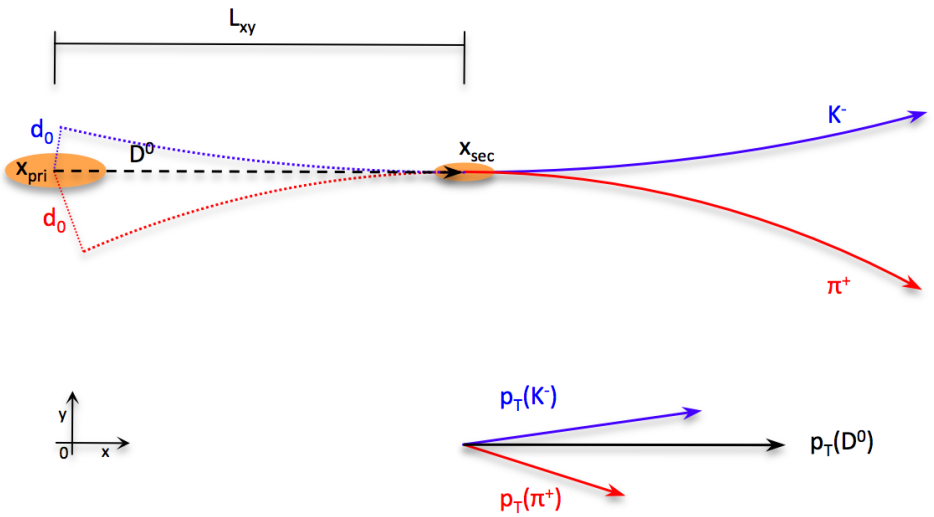

Figure 3.1: Scheme of the topology of the D^0 decay in the transverse plane for the $K^-\pi^+$ channel .

Fig. 3.1 shows the topology of the $D^0 \to K^-\pi^+$ decay. The figure also shows some of the fundamental quantities used in this analysis:

- $\vec{x}_{pri}$, the *primary vertex*, is the point where the $p\bar{p}$ collision takes place. It is the D^0 origin vertex.
- $\vec{p}_T$, the *transverse momentum*, is the projection of the momentum vector to the transverse plane (we refer to its magnitude as p_T).

- $\vec{x}_{sec}$, the *secondary vertex*, is the D^0 decay vertex.

- L_{xy}, the *transverse decay length*, is the signed distance between the primary and the secondary vertices projected to the transverse plane. It is defined as follows:

$$L_{xy} = \frac{(\vec{x}_{sec} - \vec{x}_{pri}) \cdot \vec{p}_T}{p_T} \tag{3.2}$$

  where $\vec{p}_T = (p_x; p_y; 0)$

- d_0, the *impact parameter*, is the signed distance between the origin vertex and the helix of a daughter at their closest approach. It is defined as stated in Eq. 2.8.

- Δz_0, the *longitudinal distance*, is the difference in the z coordinate of the two daughters at their closest approach to the beam, (not shown in figure, see Sec. 2.2.3.5).

- $\Delta\varphi_0$, the *transverse opening angle*, is the difference of the φ_0 angle of the two daughters at their closest approach to the beam, (not shown in figure, see Sec. 2.2.3.5).

Chapter 4

Beam position reconstruction

4.1 Importance of beam reconstruction

The beam position reconstruction is mandatory in order to extract the D^0 signal from the combinatorial background; for this task, the main step consists in performing a selection able to distinguish between prompt and secondary particles. Thanks to the spatial resolution of the CDF II tracking system (see Sec. 2.2.3.5), we can identify the particles produced in the D^0 decay from the prompt mesons produced in the event by looking at their impact parameter. The impact parameter is closely related to the beam position. In fact, the impact parameter of a track, d_0, is the distance in the transverse plane between the track and the primary vertex; it is defined as stated in Eq. 2.8 .

The $p\bar{p}$ interaction happens on the beam trajectory, so we can identify the coordinates of the primary vertex of interaction (x_c, y_c, z_c) with the beam position at the z_c coordinate of the vertex. We exploit this assumption to evaluate the beam position. Once the beam position is found, the d_0 value for each track comes straight from the definition 2.8. It is then clear that the definition of the beam position affects the reconstruction of d_0, becoming crucial for our analysis.

For the high energy runs ($\sqrt{s} = 1.96$ TeV), the beam position is reconstructed by the CDF offline software; however, this information is missing for the low energy runs ($\sqrt{s} = 900$ GeV).

In what follows, we describe the procedure we applied to obtain the parameterization of the beam for the runs used in this analysis; we tested our procedure against some high energy runs to be sure that our result is compatible with the official one.

4.2 Reconstruction procedure

The transverse profile of the luminous region inside CDF can be described by two Gaussian functions in x and y. The mean of these Gaussians defines the beam position. Their width is approximately $\sigma_T \approx 28\ \mu$m. Unfortunately, the beam is not centered with respect to the detector nor parallel to the detector z-axis. The dependence of the x and y position of the beam on z can be described, at a first order of approximation, by a linear function:

$$x = \frac{dx}{dz} \cdot z + x_0 \qquad\qquad y = \frac{dy}{dz} \cdot z + y_0, \tag{4.1}$$

where x_0 and y_0 are the position of the beam at $z = 0$ ("offset") in the transverse plane, while $\frac{dx}{dz}$ and $\frac{dy}{dz}$ are the slopes of the beam in the $0xz$ and $0yz$ planes, respectively.
Generally, run by run the orbits of protons and antiprotons beams vary a little; we have then to fit the beam position independently for each run.

As can be found in [26], two different algorithms can be used to obtain the beam position.
The first algorithm is based on the 3D reconstruction of the primary vertices[1]. The beam line will be described by the straight line that best fits their positions. The reconstruction of the beam position in the high energy runs is obtained using this algorithm.
The second algorithm is instead based directly on tracks[2]. If the beam was in its nominal position ($x_0 = 0$, $y_0 = 0$, $\frac{dx}{dz} = 0$, $\frac{dy}{dz} = 0$), the distribution of the tracks' impact parameter would be (to a first order approximation) a gaussian centered in $d_0 = 0$ and flat in φ_0, because the production of the tracks within the collision is invariant for rotation on the z-axis. The beam offset and slope

[1] We further refer to this algorithm as the vertices algorithm
[2] We further refer to this algorithm as the $d_0 - \varphi_0$ algorithm.

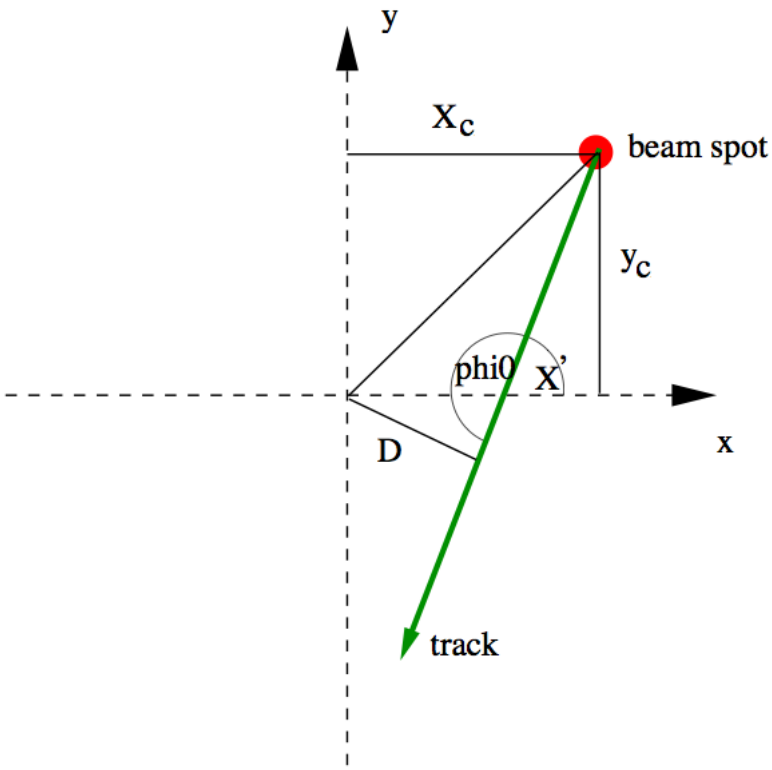

Figure 4.1: Scheme of the correlation between the impact parameter and the angle φ_0 of a track.

affect the raw d_0 versus φ_0 distribution and a correlation between the two variables arises. This correlation comes from a rototranslation of the beam with respect to the "ideal" spatial reference system described before.

As can be seen in Fig. 4.1, the impact parameter d_0 of a track coming from a primary vertex at (x_c, y_c) can be parameterized to the first order using the track parameterization of CDF [27]:

$$d_0(x_c, y_c, \varphi_0) = -x_c \sin\varphi_0 + y_c \cos\varphi_0. \tag{4.2}$$

Introducing the z position and exploiting the equations 4.1, we write the impact parameter as a function of the 4 parameters that describe the beam line:

$$d_0(z, \varphi_0) = -x_0 \sin\varphi_0 + y_0 \cos\varphi_0 - z \cdot \frac{dx}{dz} \sin\varphi_0 + z \cdot \frac{dy}{dz} \cos\varphi_0. \tag{4.3}$$

To obtain x_0, y_0, $\frac{dx}{dz}$, $\frac{dy}{dz}$, we have to do what follows:

- sample the z coordinate into several ranges;
- for each range:
  - select only tracks that satisfy minimal quality requests:
    - SVX II small angle stereo hits ≥ 1;
    - SVX II stereo hits ≥ 2;
    - SVX II axial hits ≥ 3;
    - COT stereo hits ≥ 25;
    - COT axial hits ≥ 25;
    - $p_T \geq 0.9$ GeV/c;
    - $|\eta| \leq 1.2$.
  - plot the d_0-φ_0 distribution for the selected tracks;
  - fit the distribution using the parameterization on Eq. 4.4

$$d_0(x, y, \varphi_0) = -x \sin \varphi_0 + y \cos \varphi_0, \tag{4.4}$$

- plot the x and y obtained through the fits as a function of z (the center of each range is used);
- fit both x and y distributions with a line (see Eq. 4.3).

4.3 High Energy test

We tested our procedure on four (arbitrarily chosen) high energy runs (see Tab. 4.1), comparing our result with the official beam line measurement.

We decided to divide the z-range into 12 equal sub-ranges, 8 cm long from -48 to 48 cm. For each sub-range, all the tracks with the corresponding z_0 that pass the quality requirements are used in the d_0-φ_0 plots. Fig. 4.2 shows an example of d_0-φ_0 distributions in six ranges within $0 < z \leq 48$ cm.

Some of the plots in Fig. 4.2 show blank areas, e.g. in Fig. 4.2 (f), a large blank strip is visible between $100° < \varphi_0 < 130°$. This blanks are due

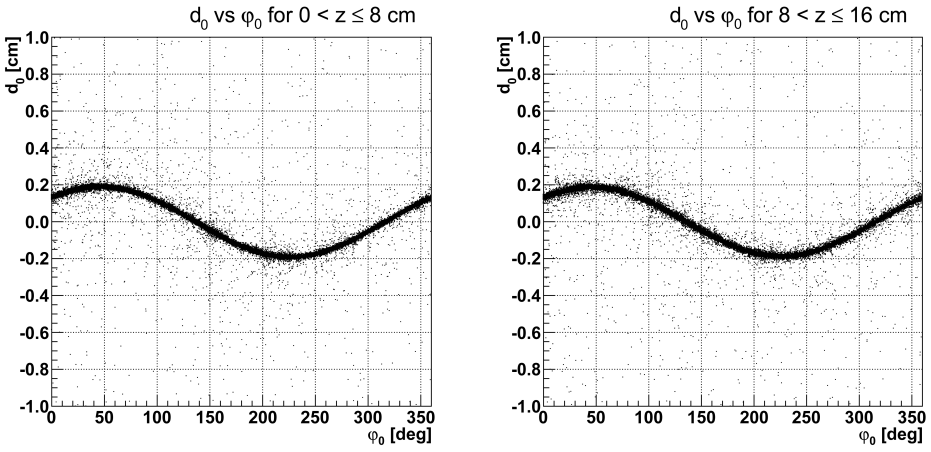

(a)

(b)

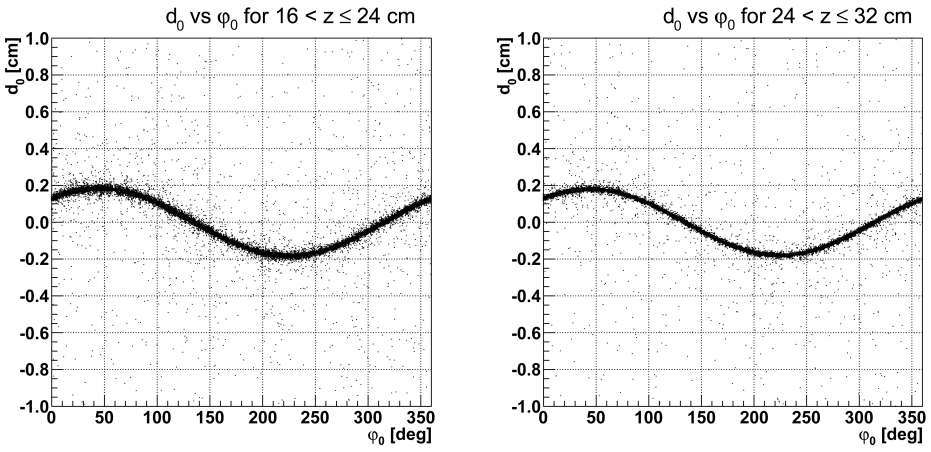

(c)

(d)

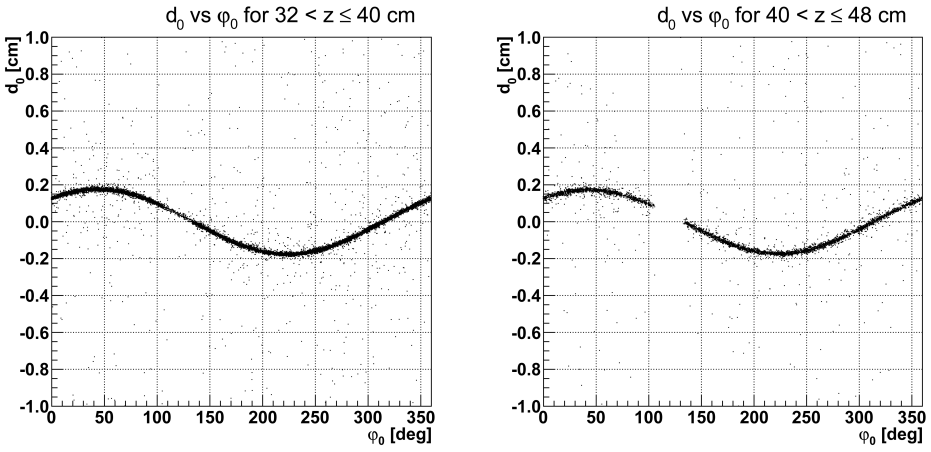

(e)

(f)

Figure 4.2: d_0 versus φ_0 in 6 z sub-ranges, run 289274.

RunNumber	Maximum Luminosity	Integrated Luminosity	MB Events
289274	249.036 $\times 10^{30}$ cm^{-2} s^{-1}	6,191.039 nb^{-1}	860,362
289331	308.152 $\times 10^{30}$ cm^{-2} s^{-1}	6,874.450 nb^{-1}	1,024,869
289384	178.287 $\times 10^{30}$ cm^{-2} s^{-1}	3,758.349 nb^{-1}	499,942
289461	295.268 $\times 10^{30}$ cm^{-2} s^{-1}	6,655.777 nb^{-1}	980,190

Table 4.1: Maximum, integrated luminosity and number of events triggered for the four high energy runs used in the test.

to blind spots in the detector tracking.

For each scatter plot, the projection of each φ_0 bin on the d_0-axis is described, to a first order approximation, by a gaussian function. For each scatter plot, we fill a corresponding "profile" plot with the mean value of d_0 in each φ_0 bin, assigning the gaussian width as the associated uncertainty. We fit these new plots instead of fitting the scatter plots. Fig. 4.3 shows the application of this method on the scatter plot (b) of Fig. 4.2. The fit of the profile plot is performed using Eq. 4.4; x and y are the free parameters that give the beam position in the transverse plane at the center of the corresponding z sub-range.

The parameters x and y of each sub-range are then plotted versus z and the beam profile in $0xz$ and $0yz$ planes is found. Fig. 4.4 shows the beam position in the $0xz$ and $0yz$ planes for the four considered runs; the black continuous lines represent the results of our fits; the black dashed lines show the systematic uncertainty due to the beam transverse width. The red lines represent the beam positions reconstructed by the official algorithm.

For each run, our result is compatible with the official one: the offset is within 8 microns (well below the minimal transverse width of the beam ≈ 28 μm) and the slope is in perfect agreement.
The procedure is therefore proved to be reliable and has been adopted in this analysis for the low energy scans.

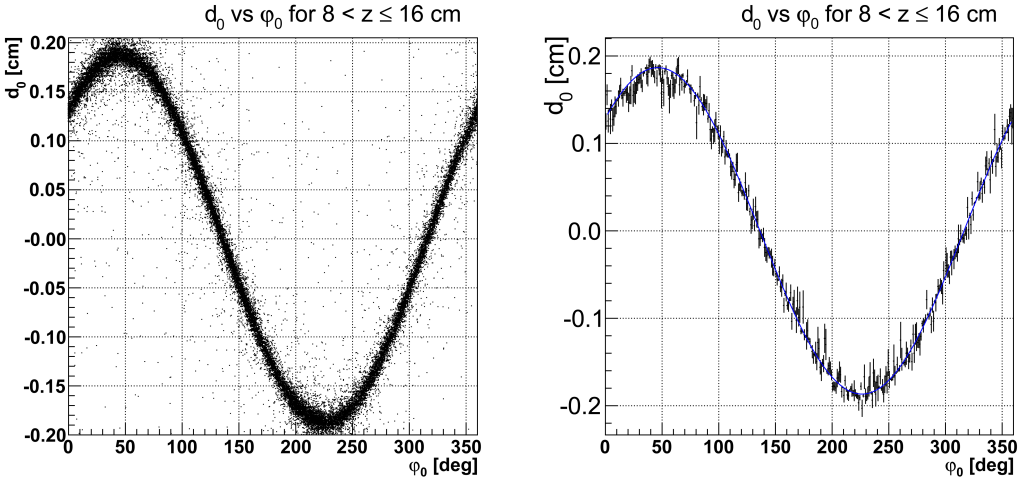

Figure 4.3: Comparison between the d_0 versus φ_0 scatter plot and the d_0 versus φ_0 profile in $8 < z \leq 16$ cm region, run 289274.

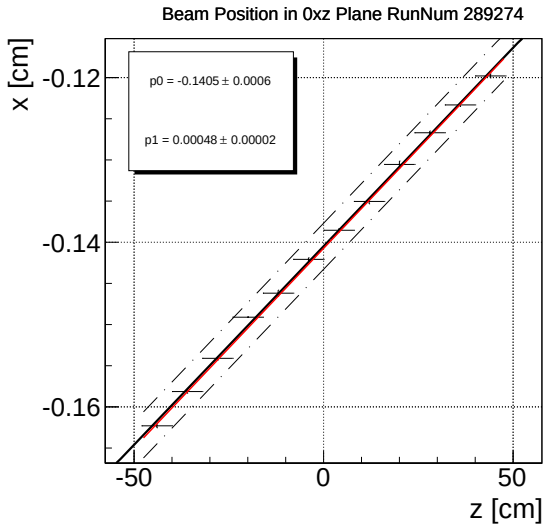

(a) Run 289274 beam position in 0xz plane.

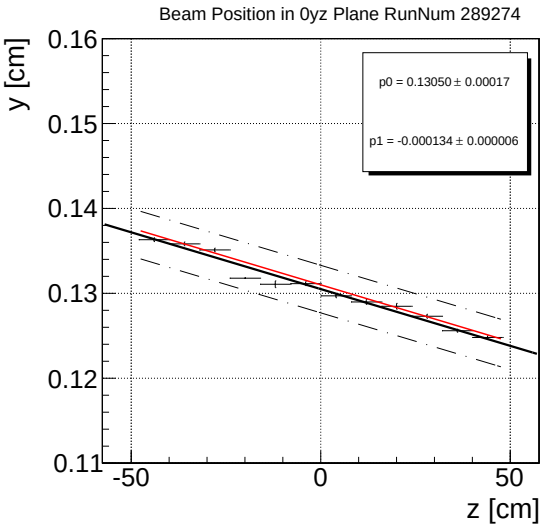

(b) Run 289274 beam position in 0yz plane.

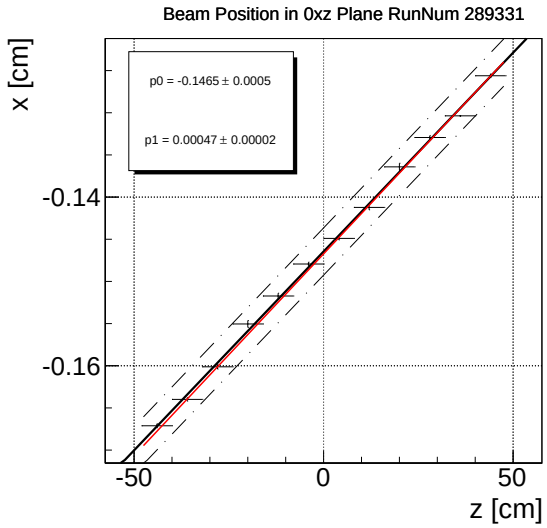

(c) Run 289331 beam position in 0xz plane.

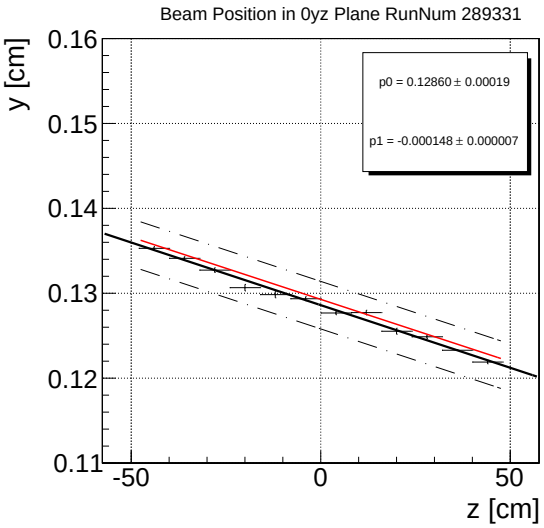

(d) Run 289331 beam position in 0yz plane.

Figure 4.4: Beam position in 0xz and 0yz planes and comparison with the official reconstruction for the four runs under exam. The black continuous lines represent the results of our fits; the black dashed lines show the systematic uncertainty due to the beam width. The red lines represent the beam position reconstructed by the official algorithm.

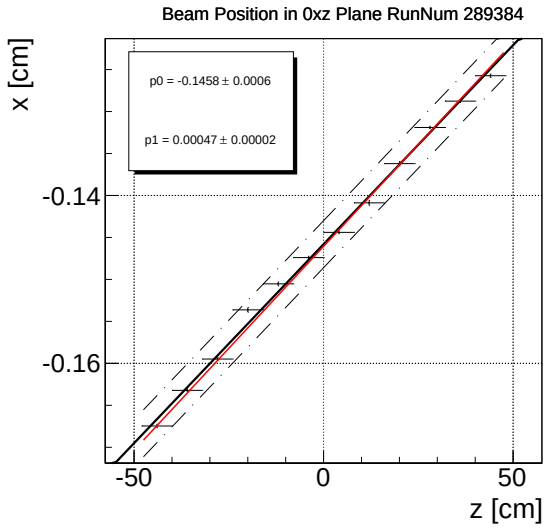

(e) Run 289384 beam position in 0xz plane.

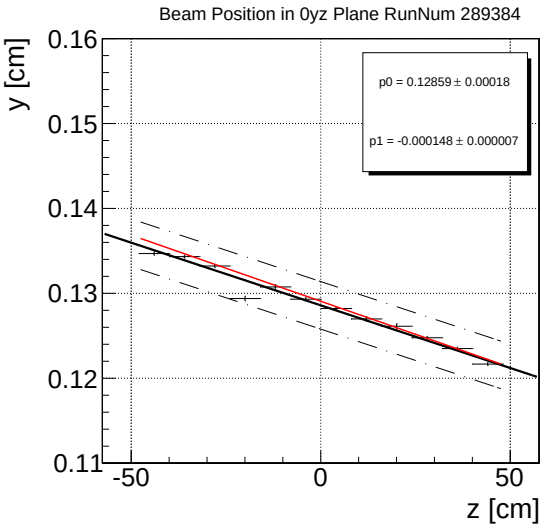

(f) Run 289384 beam position in 0yz plane.

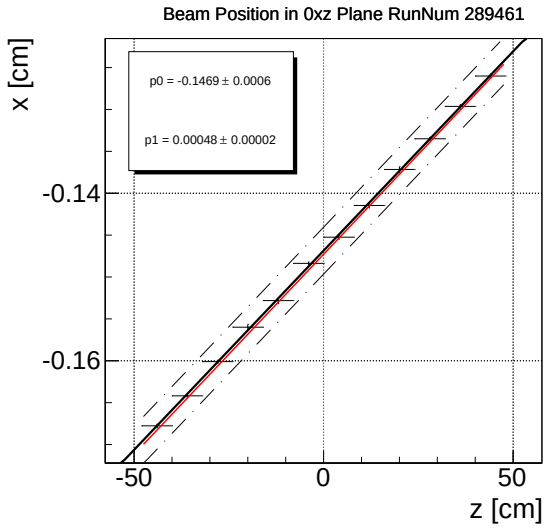

(g) Run 289461 beam position in 0xz plane.

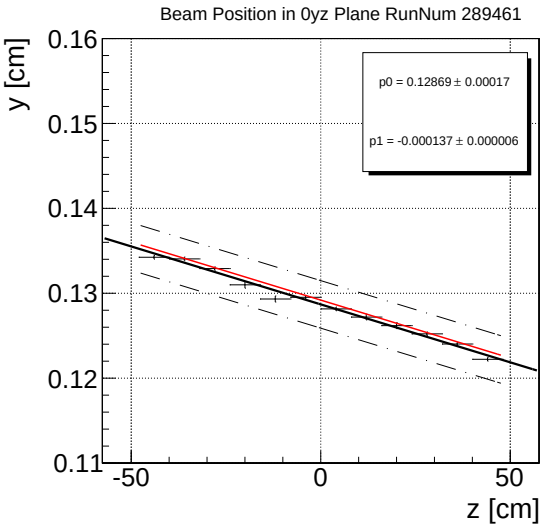

(h) Run 289461 beam position in 0yz plane.

Figure 4.4: Beam position in 0xz and 0yz planes and comparison with the official reconstruction for the four runs under exam. The black continuous lines represent the results of our fits; the black dashed lines show the systematic uncertainty due to the beam width. The red lines represent the beam position reconstructed by the official algorithm.

4.4 Low energy beams

The list of the eleven low energy runs used in this analysis is shown in Tab. 4.2.

For the reconstruction of the beam position, we apply the procedure described in the previous paragraphs to each low energy run. Fig. 4.5 shows a typical scatter plot and a typical profile plot for the $8 < z \leq 16$ cm range of a low energy run. Fig. 4.6 shows the beam position reconstruction in the $0xz$ and $0yz$ planes for the eleven low energy runs. The black continuous lines represent the results of our fits; the black dashed lines show the systematic uncertainty due to the beam width. For each low energy run, Tab. 4.3 summarizes the beam position measured using our custom procedure.

RunNumber	Maximum Luminosity	Integrated Luminosity	MB Events
311662	0.848 $\times 10^{30}$ cm^{-2} s^{-1}	4.439 nb^{-1}	2,254,669
311664	0.610 $\times 10^{30}$ cm^{-2} s^{-1}	0.603 nb^{-1}	386,554
311713	0.496 $\times 10^{30}$ cm^{-2} s^{-1}	1.590 nb^{-1}	1,548,586
311714	0.284 $\times 10^{30}$ cm^{-2} s^{-1}	0.585 nbs^{-1}	874,005
311730	1.338 $\times 10^{30}$ cm^{-2} s^{-1}	5.206 nb^{-1}	2,959,258
311825	0.717 $\times 10^{30}$ cm^{-2} s^{-1}	1.177 nb^{-1}	2,429,437
311835	0.837 $\times 10^{30}$ cm^{-2} s^{-1}	8.937 nb^{-1}	5,212,267
311910	1.132 $\times 10^{30}$ cm^{-2} s^{-1}	15.192 nb^{-1}	11,261,445
311956	0.866 $\times 10^{30}$ cm^{-2} s^{-1}	14.112 nb^{-1}	9,205,682
311976	0.891 $\times 10^{30}$ cm^{-2} s^{-1}	12.124 nb^{-1}	7,572,947

Table 4.2: Low energy runs list. The ratios of the integrated luminosity and the number of Minimum Bias events in this Table seems to be inconsistent with the ones in Tab. 4.1. This is due to the different prescales (i.e output rate) used in the two configurations.

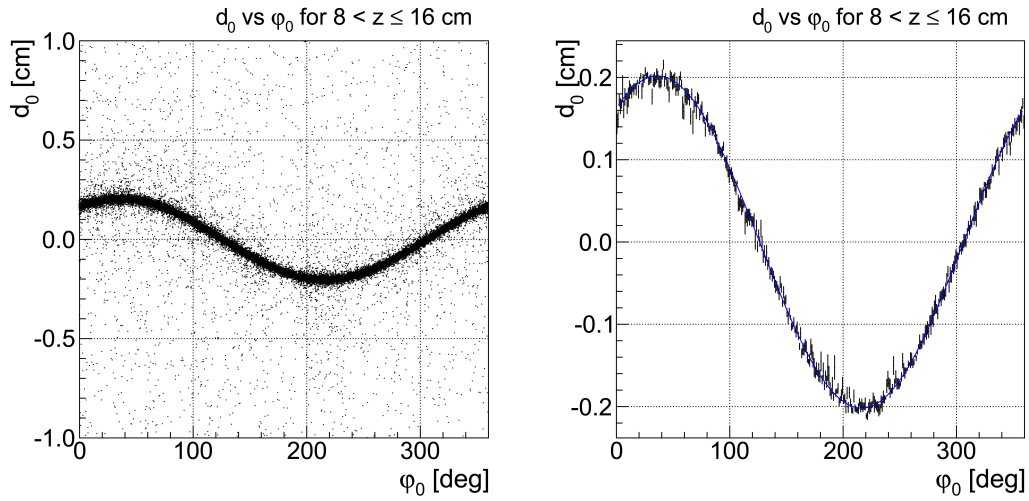

Figure 4.5: Comparison between the d_0 versus φ_0 scatter plot and the d_0 versus φ_0 profile in $8 < z \leq 16$ cm region, run 311714.

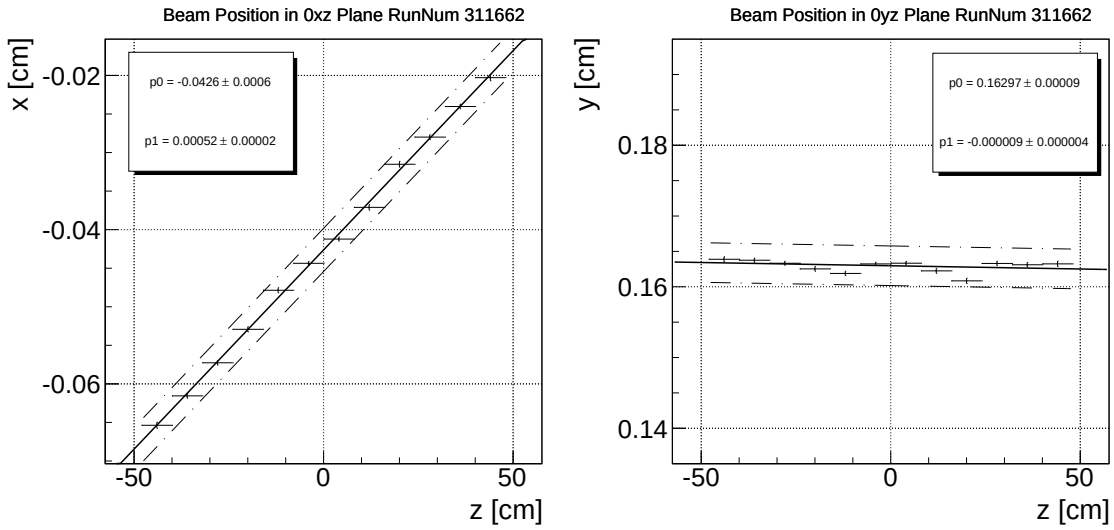

(a) Run 311662 beam position in 0xz plane.

(b) Run 311662 beam position in 0yz plane.

Figure 4.6: Beam position in 0xz and 0yz planes for low energy runs. The black continuous lines represent the results of our fits; the black dashed lines show the systematic uncertainty due to the beam width.

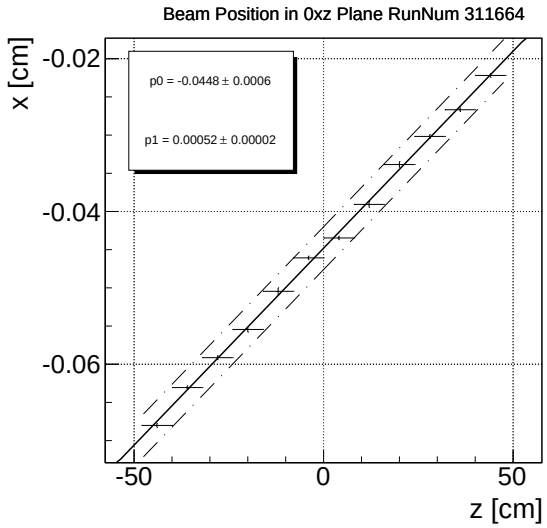

(c) Run 311664 beam position in 0xz plane.

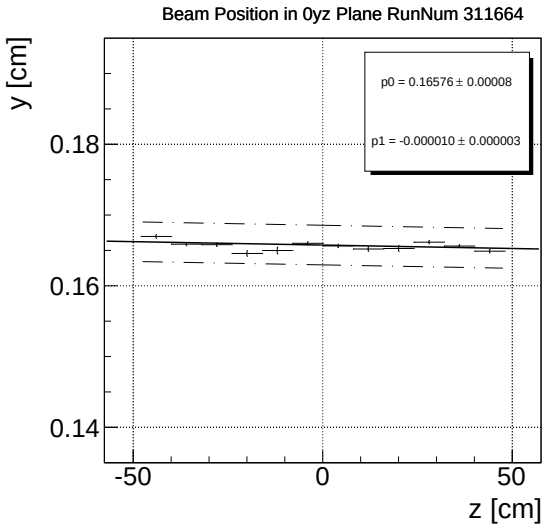

(d) Run 311664 beam position in 0yz plane.

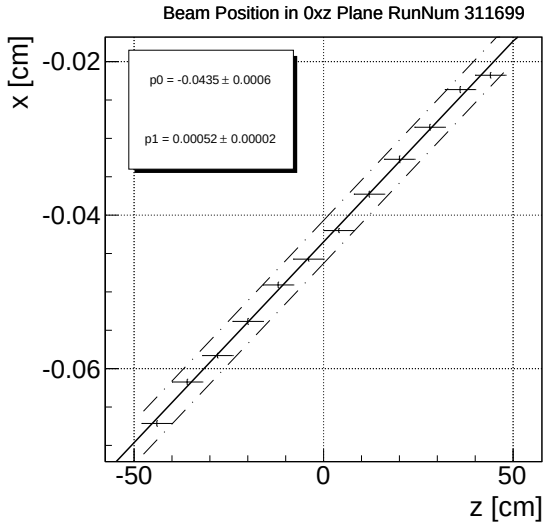

(e) Run 311699 beam position in 0xz plane.

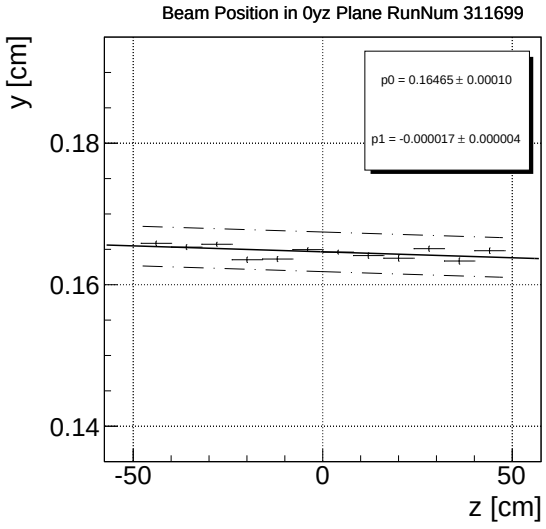

(f) Run 311699 beam position in 0yz plane.

Figure 4.6: Beam position in 0xz and 0yz planes for low energy runs. The black continuous lines represent the results of our fits; the black dashed lines show the systematic uncertainty due to the beam width.

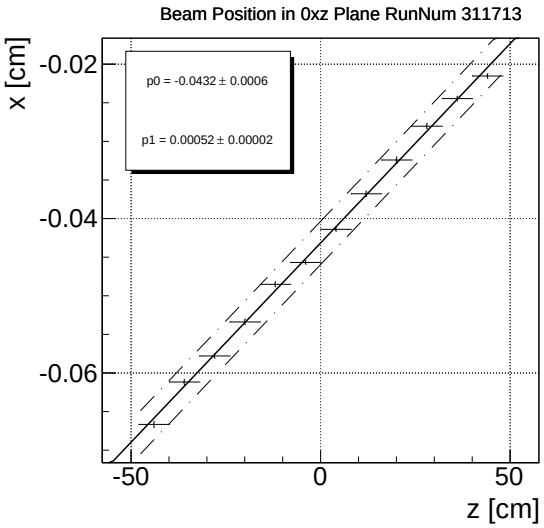

(g) Run 311713 beam position in 0xz plane.

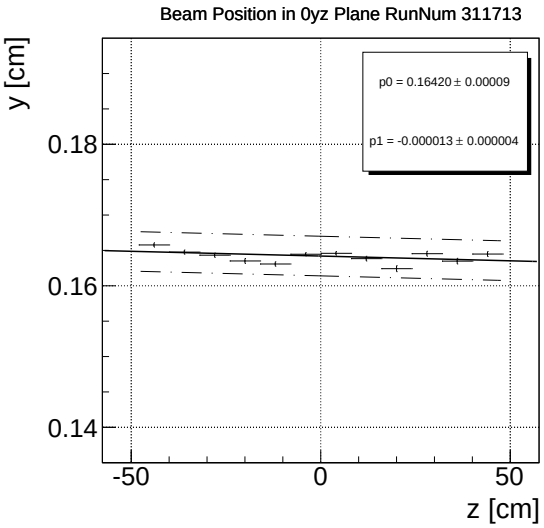

(h) Run 311713 beam position in 0yz plane.

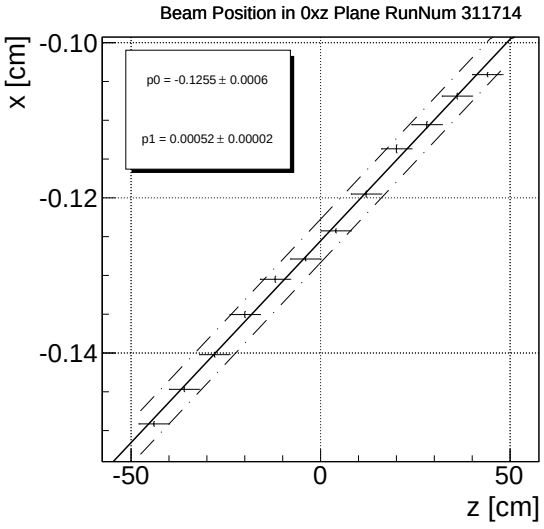

(i) Run 311714 beam position in 0xz plane.

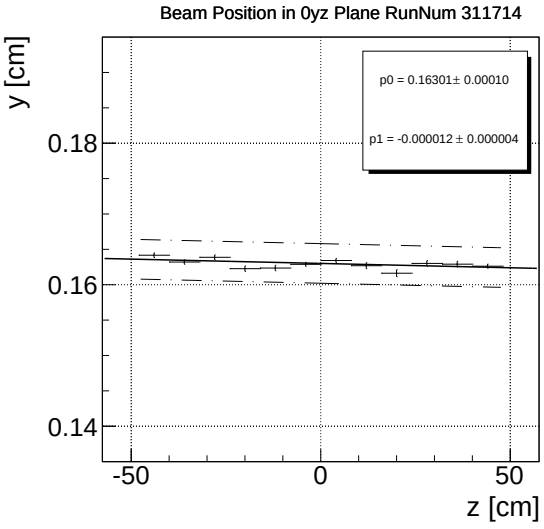

(j) Run 311714 beam position in 0yz plane.

Figure 4.6: Beam position in 0xz and 0yz planes for low energy runs. The black continuous lines represent the results of our fits; the black dashed lines show the systematic uncertainty due to the beam width.

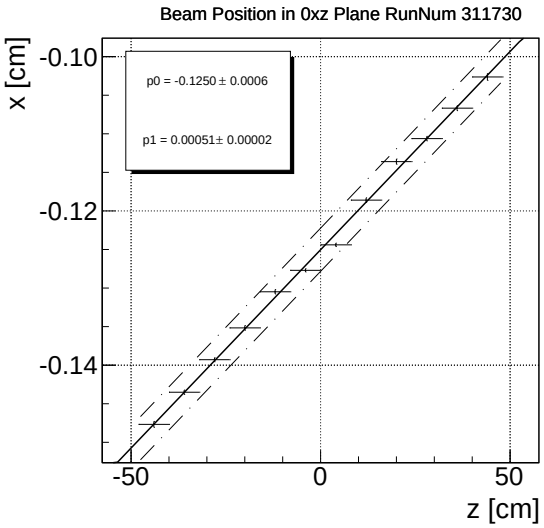

(k) Run 311730 beam position in 0xz plane.

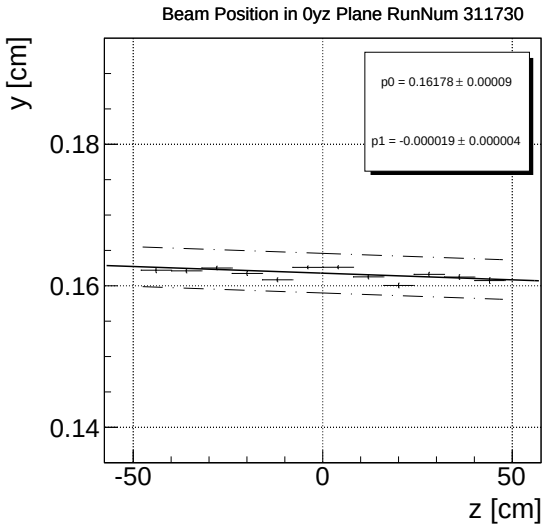

(l) Run 311730 beam position in 0yz plane.

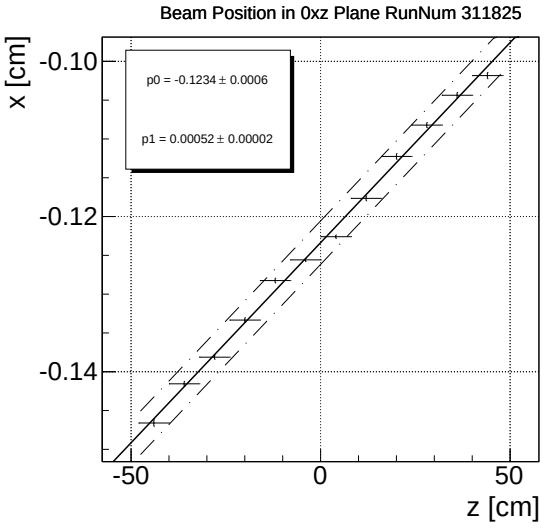

(m) Run 311825 beam position in 0xz plane.

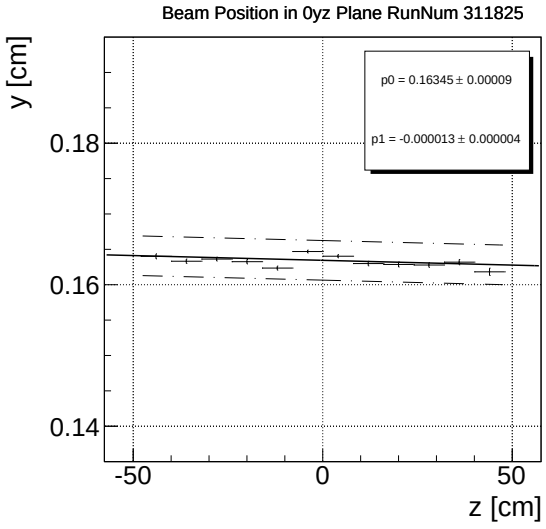

(n) Run 311825 beam position in 0yz plane.

Figure 4.6: Beam position in 0xz and 0yz planes for low energy runs. The black continuous lines represent the results of our fits; the black dashed lines show the systematic uncertainty due to the beam width.

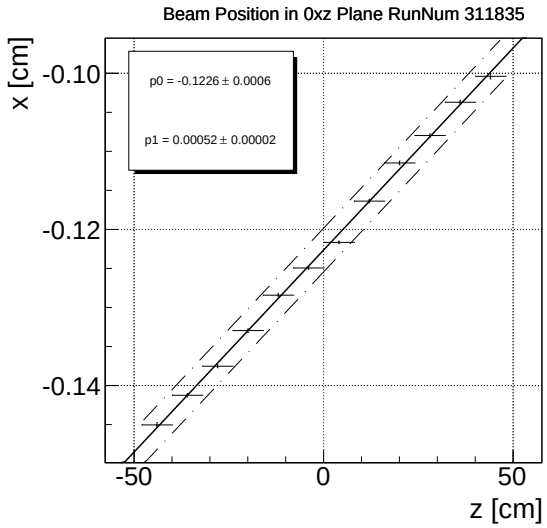

(o) Run 311835 beam position in 0xz plane.

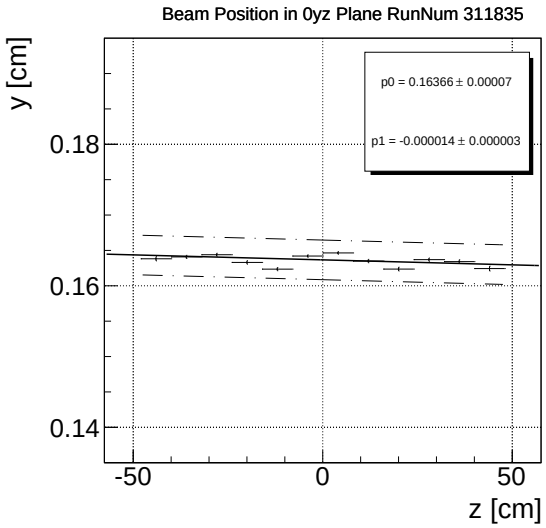

(p) Run 311835 beam position in 0yz plane.

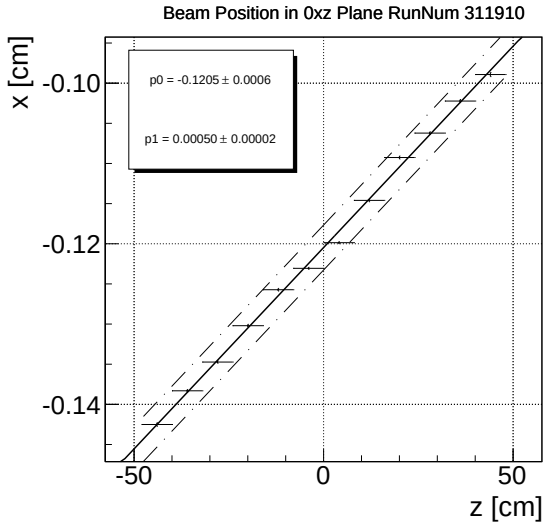

(q) Run 311910 beam position in 0xz plane.

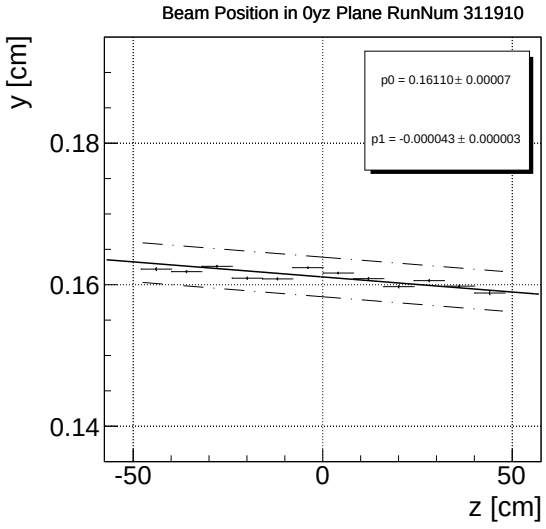

(r) Run 311910 beam position in 0yz plane.

Figure 4.6: Beam position in 0xz and 0yz planes for low energy runs. The black continuous lines represent the results of our fits; the black dashed lines show the systematic uncertainty due to the beam width.

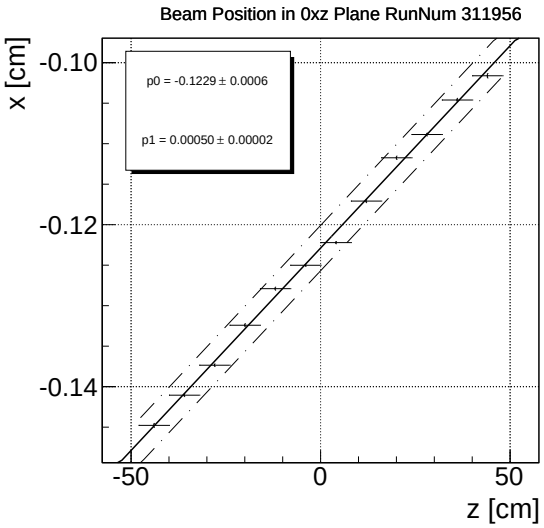

(s) Run 311956 beam position in 0xz plane.

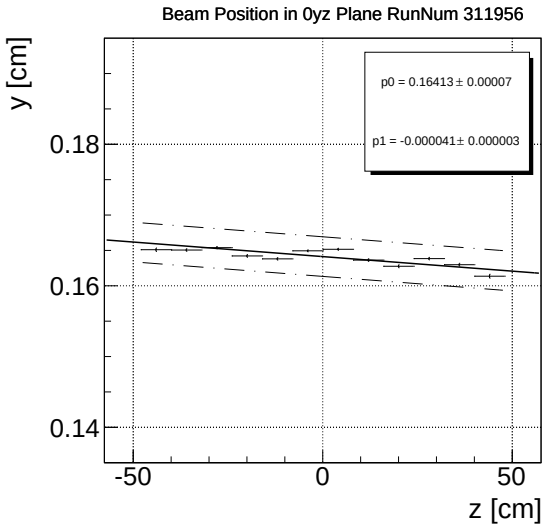

(t) Run 311956 beam position in 0yz plane.

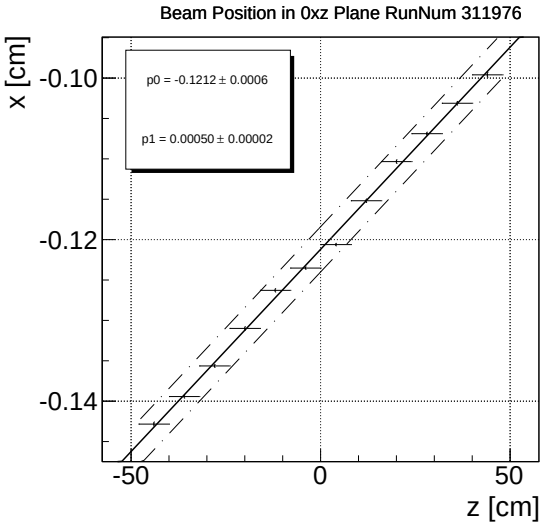

(u) Run 311976 beam position in 0xz plane.

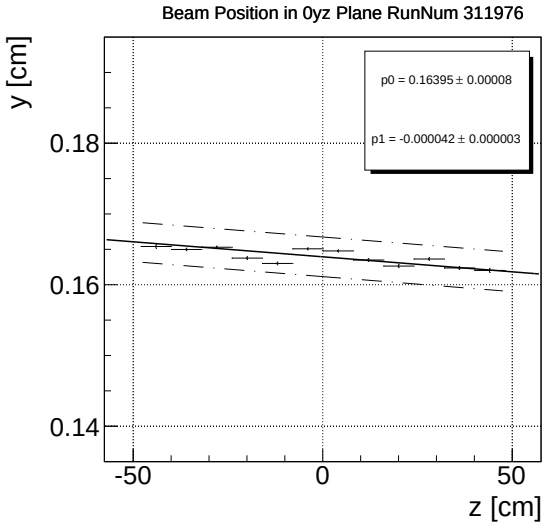

(v) Run 311976 beam position in 0yz plane.

Figure 4.6: Beam position in 0xz and 0yz planes for low energy runs. The black continuous lines represent the results of our fits; the black dashed lines show the systematic uncertainty due to the beam width.

Run#	$x_0 \pm \sigma_{x_0}$ [cm]	$\frac{dx}{dz} \pm \sigma_{\frac{dx}{dz}}$ [rad]	$y_0 \pm \sigma_{y_0}$ [cm]	$\frac{dy}{dz} \pm \sigma_{\frac{dy}{dz}}[rad]$
311662	$(-4.26 \pm 0.06) \cdot 10^{-2}$	$(5.2 \pm 0.2) \cdot 10^{-4}$	$1.6297 \cdot 10^{-1} \pm 9 \cdot 10^{-5}$	$(-0.9 \pm 0.4) \cdot 10^{-5}$
311664	$(-4.48 \pm 0.06) \cdot 10^{-2}$	$(5.2 \pm 0.2) \cdot 10^{-4}$	$1.6576 \cdot 10^{-1} \pm 8 \cdot 10^{-5}$	$(-1.0 \pm 0.3) \cdot 10^{-5}$
311699	$(-4.35 \pm 0.06) \cdot 10^{-2}$	$(5.2 \pm 0.2) \cdot 10^{-4}$	$1.6465 \cdot 10^{-1} \pm 10 \cdot 10^{-5}$	$(-1.7 \pm 0.4) \cdot 10^{-5}$
311713	$(-4.32 \pm 0.06) \cdot 10^{-2}$	$(5.2 \pm 0.2) \cdot 10^{-4}$	$1.6420 \cdot 10^{-1} \pm 10 \cdot 10^{-5}$	$(-1.3 \pm 0.4) \cdot 10^{-5}$
311714	$(-12.55 \pm 0.06) \cdot 10^{-2}$	$(5.2 \pm 0.2) \cdot 10^{-4}$	$1.6430 \cdot 10^{-1} \pm 10 \cdot 10^{-5}$	$(-1.2 \pm 0.4) \cdot 10^{-5}$
311730	$(-12.50 \pm 0.06) \cdot 10^{-2}$	$(5.1 \pm 0.2) \cdot 10^{-4}$	$1.6178 \cdot 10^{-1} \pm 9 \cdot 10^{-5}$	$(-1.9 \pm 0.4) \cdot 10^{-5}$
311825	$(-12.33 \pm 0.06) \cdot 10^{-2}$	$(5.2 \pm 0.2) \cdot 10^{-4}$	$1.6345 \cdot 10^{-1} \pm 9 \cdot 10^{-5}$	$(-1.3 \pm 0.4) \cdot 10^{-5}$
311835	$(-12.26 \pm 0.06) \cdot 10^{-2}$	$(5.2 \pm 0.2) \cdot 10^{-4}$	$1.6366 \cdot 10^{-1} \pm 7 \cdot 10^{-5}$	$(-1.4 \pm 0.3) \cdot 10^{-5}$
311910	$(-12.05 \pm 0.06) \cdot 10^{-2}$	$(5.0 \pm 0.2) \cdot 10^{-4}$	$1.6110 \cdot 10^{-1} \pm 7 \cdot 10^{-5}$	$(-4.3 \pm 0.3) \cdot 10^{-5}$
311956	$(-12.29 \pm 0.06) \cdot 10^{-2}$	$(5.0 \pm 0.2) \cdot 10^{-4}$	$1.6413 \cdot 10^{-1} \pm 7 \cdot 10^{-5}$	$(-4.1 \pm 0.3) \cdot 10^{-5}$
311976	$(-12.12 \pm 0.06) \cdot 10^{-2}$	$(5.0 \pm 0.2) \cdot 10^{-4}$	$1.6395 \cdot 10^{-1} \pm 7 \cdot 10^{-5}$	$(-4.2 \pm 0.2) \cdot 10^{-5}$

Table 4.3: Fitted beam positions and their statistical uncertainties for low energy runs.

Chapter 5

Monte Carlo samples

5.1 Monte Carlo simulation

In complex experiments like CDF II, the detector acceptance and the detector expected response to the passage of a particle are often simulated via Monte Carlo (MC) techniques. It is impossible, in fact, to analytically predict the detector behavior because of the complexity of its geometry and because of the huge number of variables to consider. MC simulation techniques are useful numerical methods that allow, e.g., to estimate the fraction of events escaping from the detector acceptance or to predict the functional form of a particular signal.

In HEP experiments, MC techniques can be generally divided into three kinds: *generation* simulation, *detector* simulation and *trigger* simulation. In this analysis we do not need the trigger simulation.
The generation simulation incorporates, for this analysis, all the physical processes involved in the $p\bar{p}$ collision. The collision is simulated from the initial interaction up to the final formation of the hadronic state.
The detector simulation is the simulation of the passage of the MC produced particles inside the detector geometry. The detector simulation also provides the generation of the signals collected by the subdetectors, their read out, etc..
The final result of a complete MC simulation is a sample of simulated data that has the same format as data, allowing their analysis with the same anal-

ysis frameworks.

Different types of generators are used in CDF Monte Carlo samples; in this analysis we used BGenerator [22].

BGenerator is used in the CDF B Monte Carlo (BMC). BMC generates samples of hadrons containing a quark b or a quark c (e.g. D mesons). After generating the hadrons, BGenerator forces them to decay into a particular final state. At the end, the decay products are propagated within the CDF II detector simulation. The joint distribution of transverse momentum and pseudo-rapidity for the different hadrons are the input information of the BGenerator.
The interactions between the particles and the different materials of the detector are also reproduced. The different signals that the particles produce in all the subdetectors are then simulated. The version 3 of the GEANT package [23] models the detector geometry and material for the standard CDF II simulation.

Some sub-detectors are simulated by specific packages rather than by GEANT. For the silicon detectors, a parametric model, tuned on data, simulates the charge deposition: it accounts for the Landau distribution, production of δ rays, capacitive charge sharing between neighboring strips and noise, etc.

The off-line database is used to tune the simulation. The configuration is changed on a run by run basis (position and slope of the beam line, relative mis-alignments between subdetectors, trigger table used, etc.) and local or temporary inefficiencies of the silicon tracker (active coverage, noisy channels, etc.) are taken into account. In this way, a detailed simulation of the real runs is available and it is possible to match the distribution of data and MC in any given sample.

5.2 Generation technique

We exploit MC techniques to simulate the shapes of the signals.
We simulate the $D^0 \to K\pi$ decay channel for the signal and all the other D^0 decay channels for the physical background. Through this simulation, we are able to interpret the invariant $K^-\pi^+$ mass distribution obtained from data.

As input for the BMC, we used the rapidity distribution versus the transverse momentum (y–p_T) for the mesons to be generated in the ranges [-1.3; 1.3]×[0; 15] GeV/c. A shape that describes the phenomenological distribution in the y–p_T range is used.

In order to reproduce the same characteristics of our data sample, we do not perform any trigger simulations. The MC events follow the same reconstruction chain as data: we also perform the same candidate selection used for the data (see Sec. 6.1).

5.3 Samples

For our purpose, we simulate two different MC sample, the $D^0 \to K\pi$ sample and the $D^0 \to X$ sample.

5.3.1 $D^0 \to K\pi$

For this sample, we generate D^0 and $\bar{D}^0$ and force them to decay into Kπ only ($D^0 \to K^-\pi^+$ and $\bar{D}^0 \to K^+\pi^-$).

Fig. 5.1 shows the resulting invariant $K^-\pi^+$ mass plot. For each candidate D^0, we assume that the negative track is a kaon and the positive track is a pion and we sum their four-momenta to evaluate the invariant mass. The plot is composed by the sum of two structures, both centered at the expected D^0 mass ($m_{D^0} \simeq 1.864$ GeV/c^2): a narrow peak with a width of about 8 MeV/c^2 and a wider one with a width of about 80 MeV/c^2. In the D^0 candidate reconstruction, we always assign the mass of the kaon to the negative track. Thus, when a $\bar{D}^0$ is produced, we fail the mass assignment of the tracks. The narrow peak in Fig. 5.1 represents the $D^0 \to K^-\pi^+$ signal

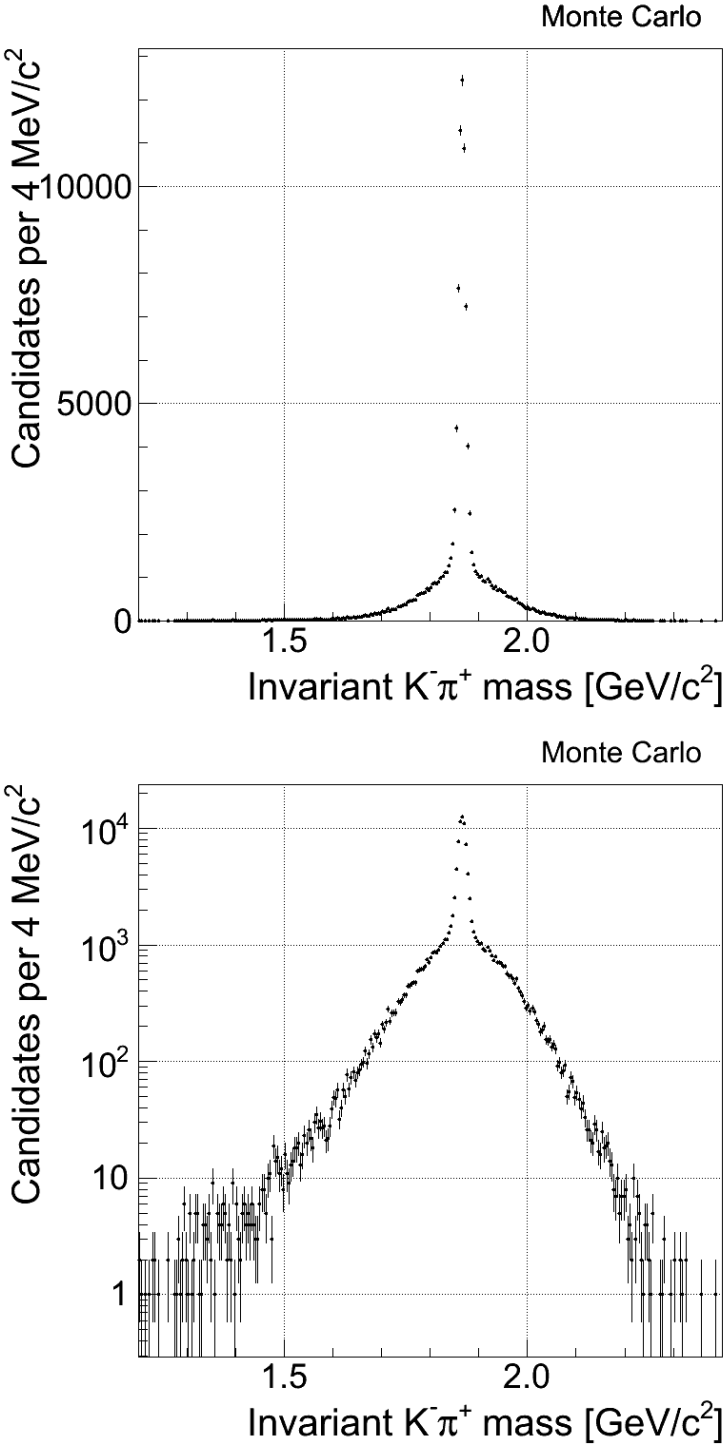

Figure 5.1: Invariant $K^-\pi^+$ mass of candidates reconstructed in the $D^0 \to K\pi$ MC sample, linear scale (Top). Invariant $K^-\pi^+$ mass of candidates reconstructed in the $D^0 \to K\pi$ MC sample, logarithmic scale (Bottom).

that we obtain when we have the Right Sign (RS) assignment of the masses: the kaon mass ($m_{K^-} \simeq 494$ MeV/c^2) is assigned to the negative track and the pion mass ($m_{\pi^+} \simeq 139$ MeV/c^2) to the positive track. The wide peak represents the $\bar{D}^0 \rightarrow K^+\pi^-$ signal that we obtain every time we have the Wrong Sign (WS) assignment of the masses.

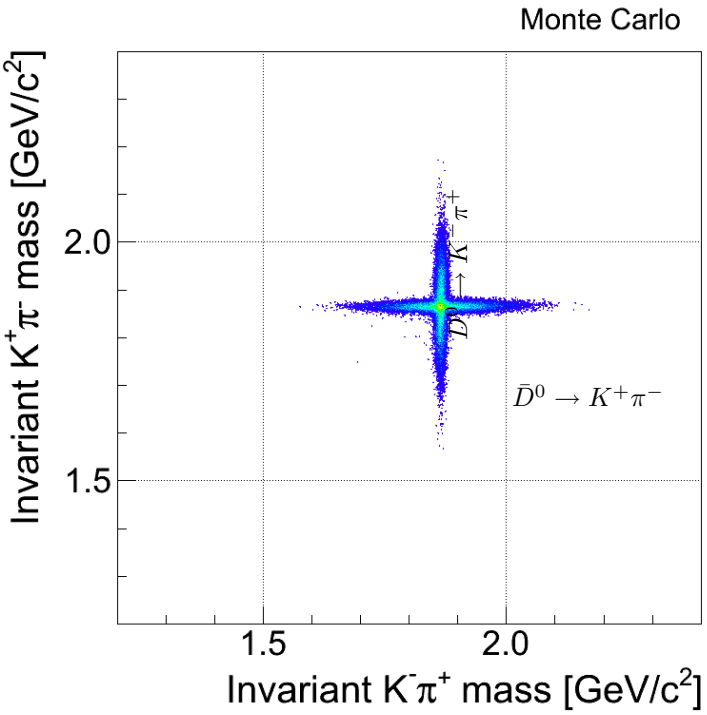

Figure 5.2: $D^0 \rightarrow K\pi$ MC sample: 2D invariant mass plot of candidates with $K^+\pi^-$ assignment in the y axis versus $K^-\pi^+$ assignment in the x axis.

We plot the two possible $K\pi$ invariant mass assignments in a 2D scatter plot: $K^+\pi^-$ versus $K^-\pi^+$. As one can see in Fig. 5.2, the two signals are distinctly separate: the generated $\bar{D}^0$ are represented by the horizontal bulk of candidates, while the generated D^0 are represented by the vertical one. Fig. 5.1 is in fact the projection of the 2D plot of Fig. 5.2 on the horizontal axis.

We use this MC sample not only to understand how the signals (D^0 and $\bar{D}^0$) appear in the invariant $K^-\pi^+$ mass plots, but also to study the signals

shapes as a function of p_T (see Sec. 5.4) and to perform the fit of the yield described in Chapt. 6.

5.3.2 $D^0 \to X$

For this sample, we simulate the main D^0 decay channels that could affect the invariant $K^-\pi^+$ mass distribution.

Fig. 5.3 shows the resulting invariant $K^-\pi^+$ mass plot. The plot still shows the RS and the WS peaks, but several other structures are visible at different invariant mass ranges.

Plotting again the two mass assignments on a 2D scatter plot (Fig. 5.4), these structures are well visible and their origin is cleared; each structure corresponds to a different decay channel, described in what follows:

- $D^0 \to KK$ decays: in the mass assignment, we assume that the positive track is due to a pion. In this case we underestimate the candidate's mass (left-bottom region of the plot);
- $D^0 \to \pi\pi$ decays: in the mass assignment, we assume that the negative tracks is due to a kaon. In this case we overestimate the candidate's mass (right-top region of the plot);
- multibody D^0 decays: we underestimate the candidate mass (left-bottom region of the plot), because we evaluate it using only two tracks (e.g. we miss additional particles, daughters of the D^0);
- combinatorial: the random combination of tracks that accidentally satisfy our selection and form a fake candidate are visible as a large diagonal band in the plot.

We use this MC sample not only to understand how the different D^0 decay channels appear in the invariant $K^-\pi^+$ mass plots; in fact, this MC also shows that from $m_{K^-\pi^+} \geq 1.8$ GeV/c^2 the only components that enter the plot are RS, WR and combinatorial background. The tails from other decay channels in this range are negligible with respect to the uncertainties expected from the fit.

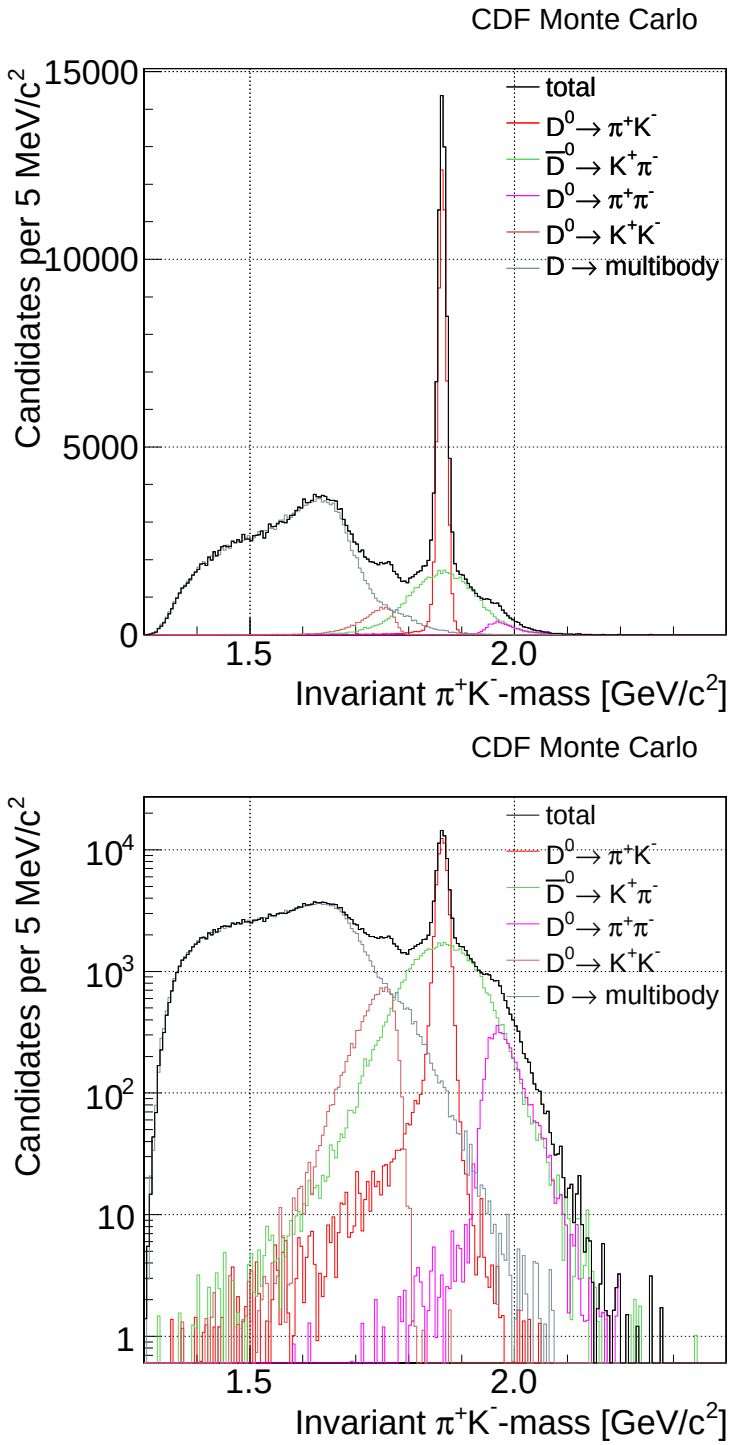

Figure 5.3: Top: Invariant $K^-\pi^+$ mass of candidates reconstructed in the $D^0 \to X$ MC sample, linear scale. Bottom: Invariant $K^-\pi^+$ mass of candidates reconstructed in the $D^0 \to X$ MC sample, logarithmic scale.

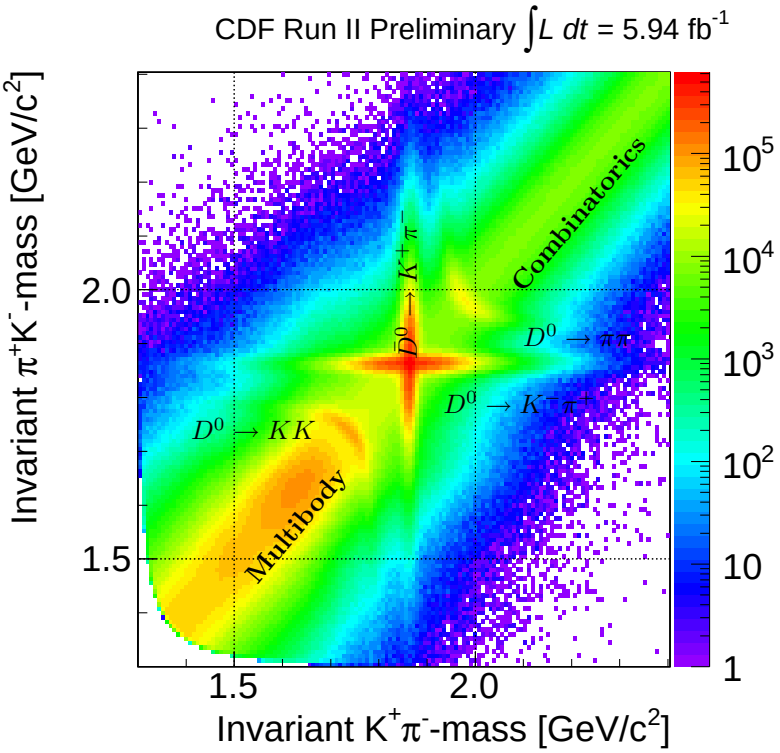

Figure 5.4: 2D invariant mass plot of candidates with $K^+\pi^-$ assignment in the y axis vs $K^-\pi^+$ assignment in the x axis. The plot shows data collected by high-p_T triggers; we are showing these data instead of our MC sample because they give a better view of the distribution thanks to the huge statistics and the presence of the combinatorial component (the BMC simulates exclusively the D^0 decays and not the whole event).

5.4 Signal shapes

The statistics in our data allow us to measure the D^0 yields as a function of $p_T(D^0)$. We divide the p_T range from 0.5 to 6.5 GeV/c in bins of 1 GeV/c. We then analyze the shapes of the RS and WS separately for each bin. The shapes obtained from the MC sample are then fixed and used to fit the data.

5.4.1 Right Sign (RS)

We parameterize the mass line shape of the RS candidates with a sum of two Gaussians. The probability density function is then defined as follows:

$$\wp_{\rm RS}(m;\vec{\theta}_{\rm RS}) = g \cdot G(m;m_1,\sigma_1) + (1-g)\cdot G(m;m_2,\sigma_2) \qquad (5.1)$$

where:

- $\vec{\theta}_{\rm RS}$ is the vector of parameters. It is defined as $\vec{\theta}_{\rm RS} = \{g, m_1, m_2, \sigma_1, \sigma_2\}$ and it is extracted by fitting the simulated invariant $K^-\pi^+$ mass distribution when a D^0 is generated;
- g is the relative fraction of the Gaussian labeled with the index *1* with respect to the sum of the two Gaussians;
- G represents the parameterization of the gaussian functions. It is defined as follows:

$$G(m;\mu,\sigma) = \frac{1}{\sigma\sqrt{2\pi}} e^{-\frac{(m-\mu)^2}{2\sigma^2}}; \qquad (5.2)$$

- $m_{1(2)}$ and $\sigma_{1(2)}$ are, respectively, the mean and the width of the Gaussian *1* (*2*);

The results of the parameterization for each bin of $p_T(D^0)$ between 0.5 GeV/c and 6.5 GeV/c are shown in Fig. 5.5. D^0 candidates from the $D^0 \to K\pi$ MC sample are used for this fits.

From these simulations, we infer that the RS signal width is almost costant throughout the all $p_T(D^0)$ range under exam.

5.4.2 Wrong Sign (WS)

We parameterize the mass line shape of the WS candidates with the same pdf used for the RS:

$$\wp_{\rm WS}(m;\vec{\theta}_{\rm WS}) = g \cdot G(m;m_1,\sigma_1) + (1-g)\cdot G(m;m_2,\sigma_2) \qquad (5.3)$$

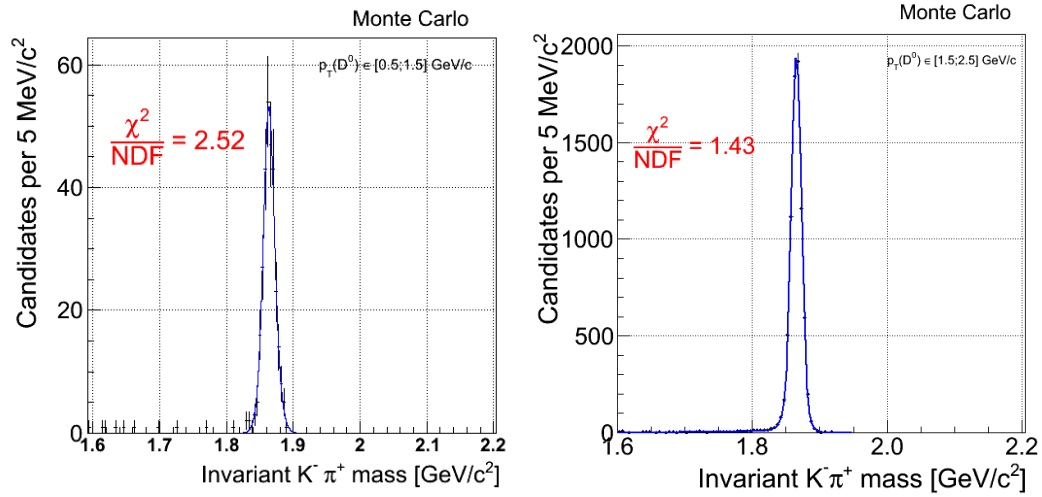

(a) $0.5 \leq p_T(D^0) < 1.5$ GeV/c (b) $1.5 \leq p_T(D^0) < 2.5$ GeV/c

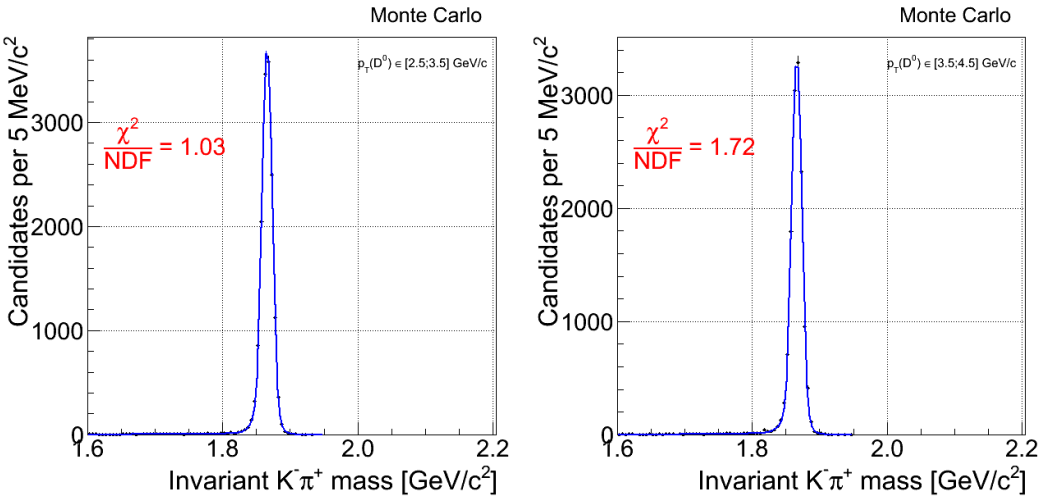

(c) $2.5 \leq p_T(D^0) < 3.5$ GeV/c (d) $3.5 \leq p_T(D^0) < 4.5$ GeV/c

Figure 5.5: $\bar{D}^0 \to K\pi$ MC sample: invariant $K^-\pi^+$ mass distribution for the RS candidates in 1 GeV/c intervals of $p_T(D^0)$.

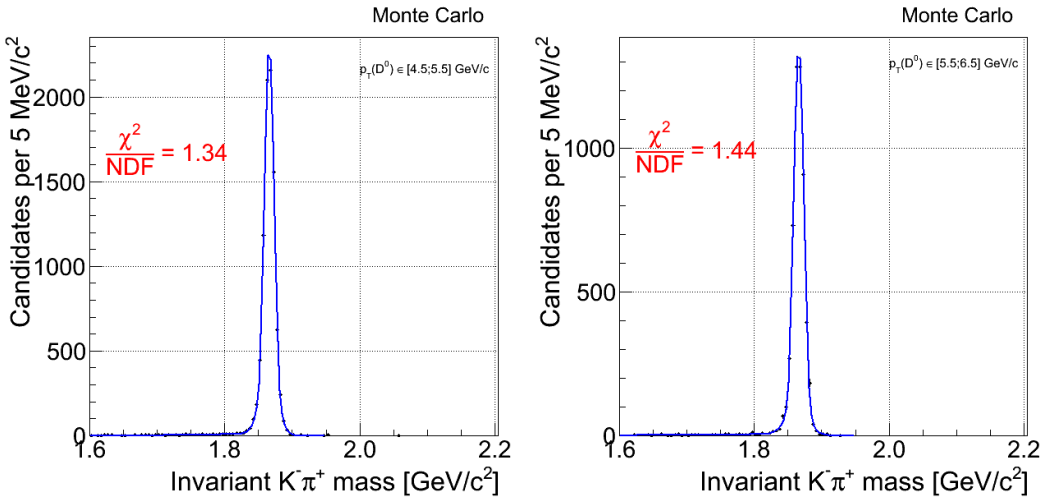

(e) $4.5 \leq p_T(D^0) < 5.5$ GeV/c (f) $5.5 \leq p_T(D^0) < 6.5$ GeV/c

Figure 5.5: $\bar{D}^0 \to K\pi$ MC sample: invariant $K^-\pi^+$ mass distribution for the RS candidates in 1 GeV/c intervals of $p_T(D^0)$.

The results of the parameterization for each bin of $p_T(D^0)$ for the WR are shown in Fig. 5.6. $\bar{D}^0$ candidates from the $D^0 \to K\pi$ MC sample are used for this fits.

At lower masses, a long tail due to a soft photon emission is present. For the fit shapes, we do not take into account the radiative tail because this correction is minimal with respect to the measurement uncertainties.

We notice that the WS signal width has a clear dependence on the $p_T(D^0)$, unlike the RS shapes. The width of the distribution increases with the momentum.

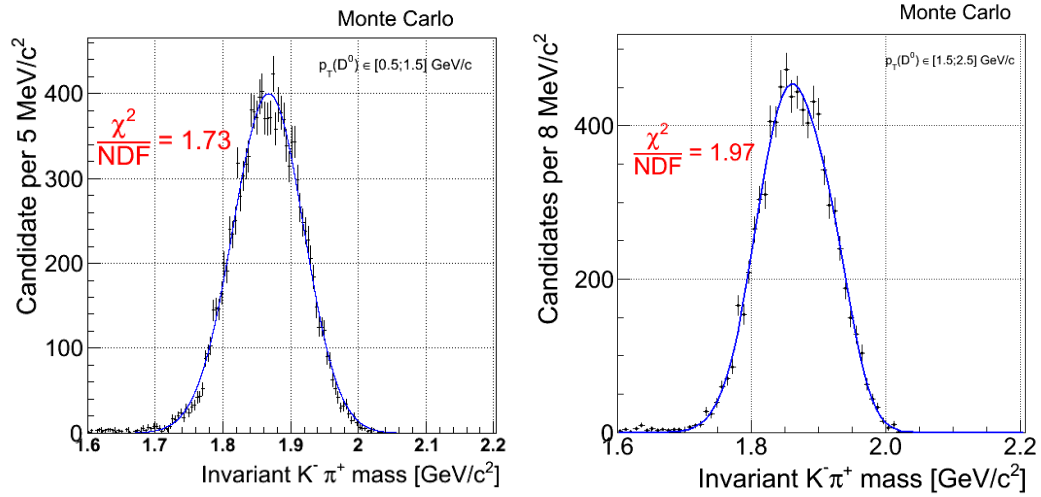

(a) $0.5 \leq p_T(D^0) < 1.5$ GeV/c

(b) $1.5 \leq p_T(D^0) < 2.5$ GeV/c

(c) $2.5 \leq p_T(D^0) < 3.5$ GeV/c

(d) $3.5 \leq p_T(D^0) < 4.5$ GeV/c

Figure 5.6: Invariant $K^-\pi^+$ mass distribution for the WS candidates in 1 GeV/c intervals of $p_T(D^0)$.

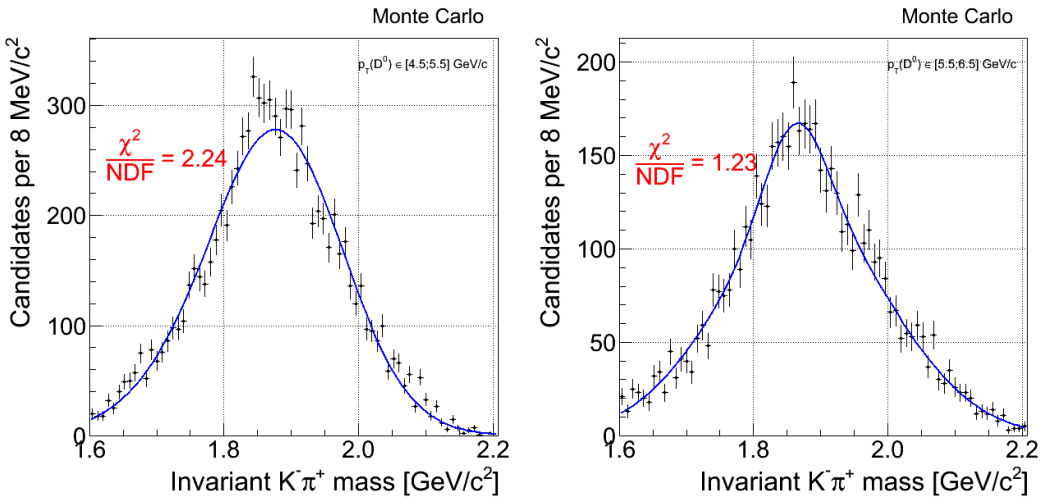

(e) $4.5 \leq p_T(D^0) < 5.5$ GeV/c (f) $5.5 \leq p_T(D^0) < 6.5$ GeV/c

Figure 5.6: Invariant $K^-\pi^+$ mass distribution for the WS candidates in 1 GeV/c intervals of $p_T(D^0)$.

5.4.3 Background

Unrelated couples of tracks can accidentally satisfy our selection requirements on candidates, generating a combinatorial background.

From the MC simulation, we observe that the the signal is spread on a large invariant mass range around the expected D^0 mass value because of the WS candidates. Thus, we can't rely on the sidebands of the data invariant mass plot to parametrize it. In addition to that the MC does not simulate the whole event, but only the signal.

We extract the combinatorial background trend directly from data by forcing the reconstruction of fake candidates. We repeat exactly our selection but using couples of tracks of the same sign (SS). We find that a decreasing exponential shape is a good parameterization for the combinatorics trend. Fig. 5.7 shows the invariant $K^{\pm}\pi^{\pm}$ mass plot for the SS candidates, integrated over all the p_T range.

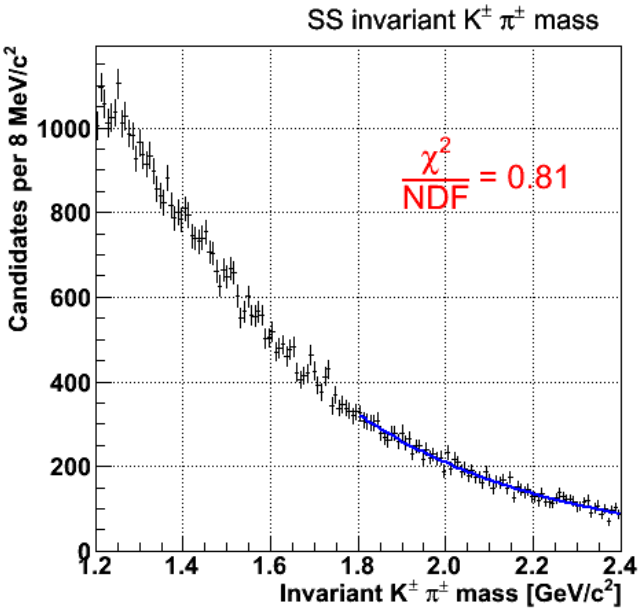

Figure 5.7: Invariant $K^{\pm}\pi^{\pm}$ mass distribution for Same Sign candidates of the data sample. The distribution is integrated over the whole $p_T(D^0)$ range.

Chapter 6

Signal evidence

6.1 Base selection

We discuss here the data selection which leads to the measurement of D^0 candidates in the sample. The two fundamental parameters of the selection are the daughters' impact parameter, d_0, and the D^0 transverse decay length, L_{xy}; these parameters both depend on the beam position. In the following, we use the d_0 and L_{xy} referred to the beam measurement performed in Chap. 4.

The method to reconstruct the D^0 candidates consists in evaluating the invariant mass of any possible combination of two tracks (with opposite charge) reconstructed in each event, assuming that they are a K and a π.

To suppress fake tracks, we apply some selection criteria, specifically studied for this task. We select tracks only in the η and p_T ranges where the reconstruction efficiency of the tracking system is maximum. We also require a minimum impact parameter of the tracks in order to reduce the number of the tracks coming from the primary vertex of interaction and maximize the number of tracks coming from a secondary vertex.

The requests for the single track are the following:

- SVX II small angle stereo hits ≥ 1;
- SVX II stereo hits ≥ 2;
- SVX II axial hits ≥ 3;

- COT stereo hits ≥ 25;
- COT axial hits ≥ 25;
- $|\eta| \leq 1.2$;
- $p_T \geq 0.7$ GeV/c;
- 60 μm $\leq |d_0| \leq 1.0$ mm;

The first six requests represent a base "quality" selection of the tracks used in what follows. To fix the values of these parameters, we take into account the tracking system specification: in fact, these values assure the lowest contamination of fake reconstructed tracks. The requirements on transverse momentum and on impact parameter are preliminarly set after the study of their distributions in MC events. Each possible pair of tracks that passed the above selection is then required to meet the following additional criteria:

- $q_1 \cdot q_2 < 0$;
- $d_{0,1} \cdot d_{0,2} < 0$;
- $2^\circ \leq \Delta\varphi_0 = |\varphi_{0,1} - \varphi_{0,2}| \leq 90^\circ$;
- $\Delta z_0 = |z_{0,1} - z_{0,2}| \leq 6$ mm;

where we label the parameters relative to the negative track with (1) and the ones relative to the positive track with (2); q_1 and q_2 are the daughters' charges. The first two requirements are two constraints set by the decay geometry and kinematics. We make requests on $\Delta\varphi_0$ studying its distribution in MC events in order to take into account tracking resolution ($\Delta\varphi_0 \geq 2^\circ$) and kinematics of the decay channel ($\Delta\varphi_0 \leq 90^\circ$).

For each couple, we assign the masses to the tracks in the hypothesis that the negative track represents the kaon and the positive track represents the pion. We set the z coordinate of the primary vertex to be the average of the tracks z_0; the x and y coordinates are then obtained from those of the beam after evaluating the beam position in the transverse plane at that z.

Then, we fit each pair of tracks, looking for a possible common origin point displaced by the primary vertex.

The fitter looks for a possible intersection point between the two tracks in the transverse plane. The fit converges only if the longitudinal distance between the two helices is within a certain threshold. The fitter returns the candidate's decay vertex position and the resulting χ^2/ndf of the fit, referred to as χ^2 in what follows. We then apply the following selection on the reconstructed candidates:

- $L_{\rm xy} \geq 300$ μm;
- $|y(D^0)| \leq 1$;
- $\chi^2 \leq 9$;

where $y(D^0)$ is the candidate's rapidity; its value represents the rapidity range we are interested in. The values of the decay length and χ^2 are fixed at first studying their distributions in MC events.

6.2 Evidence of the D^0 signal

We plot the invariant $K^-\pi^+$ mass distribution for the candidates selected as described above, looking for a structure in the D^0 mass region: Fig. 6.1 shows the resulting distribution.
This plot represents the first evidence of the D^0 signal and, in general, of the charm production in a $p\bar{p}$ collider experiment at $\sqrt{s} = 900$ GeV.
The distribution shows a peak at the expected D^0 mass, $m_{D^0} \simeq 1.864$ GeV/c^2.

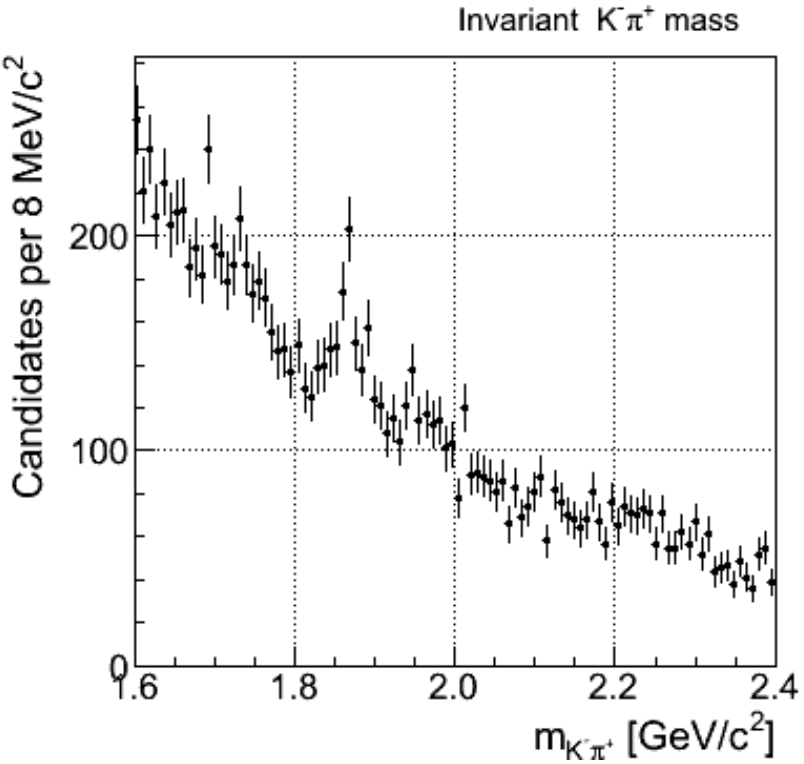

Figure 6.1: Invariant $K^-\pi^+$ mass distribution of ZB plus MB events obtained with the discussed selection.

6.3 Fitting procedure

In order to find the D^0 yield, we need to perform a fit of the invariant $K^-\pi^+$ mass distribution of the selected candidates.

The bins of the invariant $K^-\pi^+$ mass plots have a constant width of 8 MeV/c^2; the fit range is $[\mathrm{m}_0; m_{max}] = [1.8\ ;\ 2.4]$ GeV/c^2, as described in Sec. 5.3.2.

We assume a Poisson distribution for the number of events in each bin, n_b, because the bin contents represent counts. We define $f(m, \mathbf{p})$ to be the probability density function used to perform the fit and $\mathbf{p}$ to be the vector of the fit parameters. The fitted bin content is $f_b(\mathbf{p})$; in the equations we refer to $f_b(\mathbf{p})$ as f_b for sake of simplicity. Thus, the histogram likelihood results to be the following:

$$\mathcal{L}_b(\mathbf{p}) = \prod_{b=1}^{M} \frac{(f_b)^{n_b} e^{-f_b}}{n_b!}, \tag{6.1}$$

giving

$$\mathcal{F}_b(\mathbf{p}) = -2 \ln \mathcal{L}_b(\mathbf{p}) = -2 \sum_{b=1}^{M} (n_b \ln f_b - f_b - \ln n_b!). \tag{6.2}$$

$\sum_{b=1}^{M} f_b$ is the fitted contents of all bins. $\sum_{b=1}^{M} \ln n_b!$ is independent of $\mathbf{p}$ and does not alter the fit result. Ignoring this term, we perform the fit minimizing the following function:

$$\mathcal{F}_b(\mathbf{p}) = -2 \ln \mathcal{L}_b(\mathbf{p}) = -2 \sum_{b=1}^{M} n_b \ln f_b + 2 \sum_{b=1}^{M} f_b. \tag{6.3}$$

With respect to a χ^2 fit, the likelihood method has the advantage of treating correctly the empty bins and use them in the fitting procedure.

In our case, the parameter vector is $\mathbf{p} = (n_S,\ n_B,\ \mathrm{q})$, where n_S and n_B are respectively the signal and background yields, while q is the slope of the exponential used for the combinatorics.
The fit function is defined as follows:

$$f(m; \mathbf{p}) \quad = \quad n_S \cdot \wp_{\mathrm{sig}}(m) + n_B \cdot \wp_{\mathrm{bkg}}(m; q). \tag{6.4}$$

$\wp_{\rm sig}(m)$ is the Probability Density Function (*pdf*) of the signals; it is defined as follows:

$$\wp_{\rm sig}(m) = f_{\rm RS} \cdot \wp_{\rm RS}(m) + (1 - f_{\rm RS}) \cdot \wp_{\rm WR}(m); \tag{6.5}$$

where $f_{\rm RS}$ is the fraction of RS candidates with respect to the number of D^0 and $\bar{D}^0$ candidates. We set its value to 0.5 assuming the C-invariance of the strong interaction production. $\wp_{\rm RS}(m)$ and $\wp_{\rm WR}(m)$ are fixed in shape and central value by the fit of the corresponding MC (see Sec. 5.4).
$\wp_{\rm bkg}(m)$ is the pdf of the background. It is defined as follows:

$$\wp_{\rm bkg}(m; q) = \frac{e^{-q \cdot m}}{\int_{m_0}^{m_{\rm max}} e^{-q \cdot m} dm}. \tag{6.6}$$

The yield is defined as the integral of the RS plus the WS fit functions; in this manner, the yield represents the number of D^0 and $\bar{D}^0$ found.

6.4 D^0 yield

We now fit the $K^-\pi^+$ mass distribution for all the candidates with $p_T(D^0)$ greater than 1.5 GeV/c and calculate the yield relative to the base selection described in Sec. 6.1. Fig. 6.2 shows the results of the fit.

We compare the D^0 yield in the 900 GeV sample with the one in the 1.96 TeV. This comparison is possible because the data were collected by the same detector and the same selection configuration is applied. We neglect here minor differences in the reconstruction efficiencies that may arise due to the different center of mass energies and that will need more detailed studies. We choose the selection described in Sec. 6.1. For each sample, we normalize the invariant $K^-\pi^+$ mass plot to the number of events in the sample. The resulting plots are shown in Fig. 6.3

In the low energy sample we obtain one third of candidates per million of events with respect to the high energy one. This reduction is due to the difference of the D^0 cross sections at the different energies: the ratio between

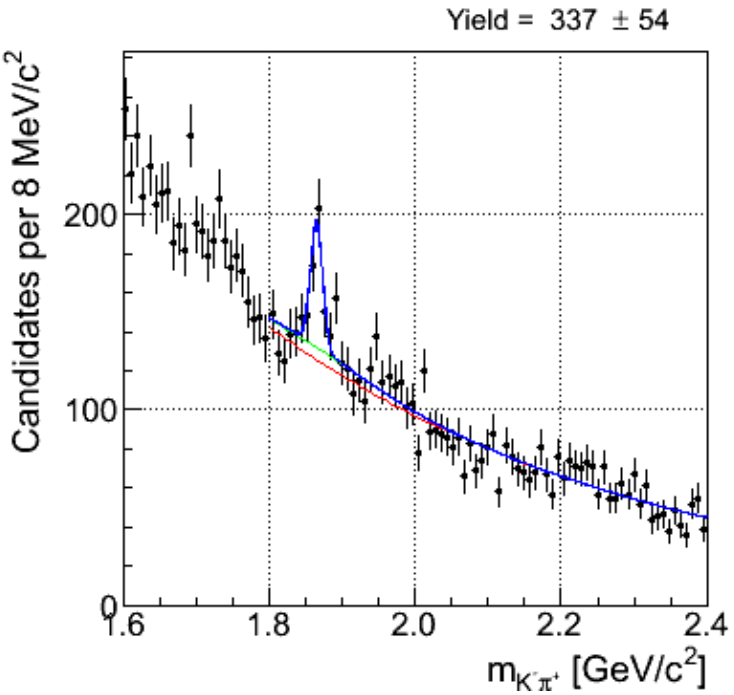

Figure 6.2: Invariant $K^-\pi^+$ mass distribution of ZB plus MB events obtained with the discussed selection. The blue line represents the result of the fit; the combinatorial background (red) and the WS (green) contributions are also shown.

the high and the low energy distributions is consistent with what is expected from a rough extrapolation of the total $c\bar{c}$ cross section (see Fig.1.3).

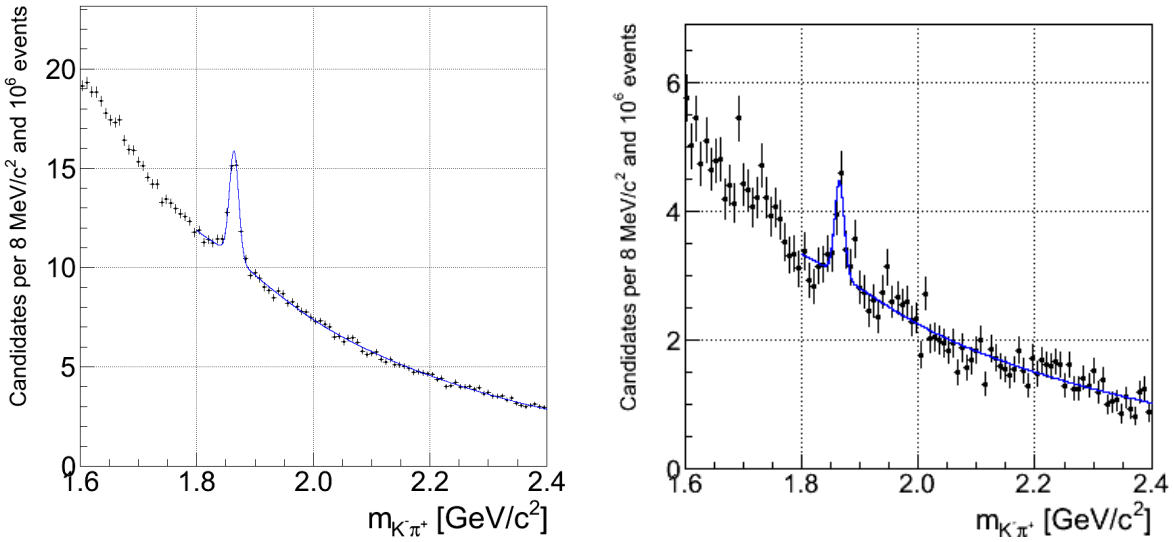

(a) Normalized yield at $\sqrt{s} = 1.97$ TeV.

(b) Normalized yield at $\sqrt{s} = 900$ GeV.

Figure 6.3: Comparison between the invariant $K^-\pi^+$ mass plots, normalized to the number of events in the sample, obtained in the high energy sample (left) and in the low energy sample (right).

Chapter 7

Differential yields

7.1 Selection optimization

The requirements described in the previous chapter were set in order to unfold the D^0 signal from the background, considering all the candidates with $p_T \geq 1.5$ GeV/c. If the D^0 production is studied as a function of the D^0 transverse momentum, this selection is not guaranteed to be the best one as a function of $p_T(D^0)$.

Thus, instead of considering all the candidates with $p_T \geq 1.5$ GeV/c, we divide the $p_T(D^0)$ range in bins of 1 GeV/c and we perform an optimization procedure of the selection independently in each $p_T(D^0)$ bin.
Since the MC simulation does not correctly reproduce the background, we decided to use a pure data-driven optimization.

The aim of the optimization procedure is to reduce the statistical uncertainty associated with the signal for each $p_T(D^0)$ bin. In order to do so, we define a figure of merit that accounts for the signal combined with the background and we find the selection that maximizes it, independently for each bin.

We define the signal $\mathcal{S}$ as the integral of the RS and WS fit functions in the mass range $m_{D^0} \pm 16$ MeV/c^2, i.e. $m_{D^0} \pm 2\sigma_{m_{D0}}$; we define the background $\mathcal{B}$ as the integral of the background fit function in the same range.

In order to avoid eventual statistical biases in the selection, we proceed as follows:

- the sample is split into two mutually exclusive subsamples, A and B, using a random criterion. We choose to fill the subsample A with the events with even event number and B with the ones with odd event number, obtaining independent subsamples of approximately the same size.

- We *independently* apply the same optimization steps on both the subsamples:

  1. we measure the signal events $\mathcal{S}_i^A$ and the background events $\mathcal{B}_i^A$ which satisfy the i-th selection configuration in subsample A by performing a fit of the candidates invariant mass distribution;
  2. we choose the figure-of-merit

     $$f(\mathcal{S}_i^A, \mathcal{B}_i^A) = \frac{\mathcal{S}_i^A}{\sqrt{\mathcal{S}_i^A + \mathcal{B}_i^A}}$$

     and we maximize it over the space of configurations built by all combinations of requirements. We chose this figure of merit because it gives an estimate of how much the signal is unlikely to be a background fluctuation;
  3. the selection configuration corresponding to the maximum of f defines the set of requirements optimized in sample A;
  4. we repeat steps 2-3 in the sample B;

- we obtain the final sample by applying to the subsample B the requirements optimized in subsample A and viceversa. Since a background fluctuation is not likely to happen in the same mass range for independent samples, we obtain a sample of candidates that can be considered statistically unbiased and optimized.

We use the variables listed in Tab. 7.1 to built a 5D matrix of selection configuration. To built the matrix, we differentiate the selection on each single variable for several different values, referred to as "steps". The number of steps considered for each variable and its range is listed in the table.

Variable	Range	Number of steps
p_T of the daughters	[0.7; 1.0] GeV/c	i = 4
d_0 of the daughters	[0; 160] μm	j = 10
Δz_0 of the daughters	[0.2; 0.7] cm	k = 6
χ^2 of the candidate	[2; 12]	l = 10
L_{xy} of the candidate	[0; 340] μm	m = 10

Table 7.1: Variables used in the optimization procedure; we report the range mapped and the number of steps used.

A selection configuration is defined as:

- $p_T \geq p_{T,i}$;
- $|d_0| \geq |d_{0,j}|$;
- $|\Delta z_0| \leq |\Delta z_{0,k}|$;
- $\chi^2 \leq \chi^2_l$;
- $L_{\rm xy} \geq L_{\rm xy,m}$,

where $p_{T,i}$, $d_{0,j}$, $\Delta z_{0,k}$, χ^2_l and $L_{\rm xy,m}$ are the different values corresponding to the different steps of each single variable selection.

We map the figure of merit over every possible combination of requirements on the five variables. Each configuration is coded with a single number (C) where every digit represents the considered step for each variable: $C = ijklm$.

Fig. 7.1 shows a typical plot of the figure of merit versus the configuration number. Several peaks are visible: the highest one represents the best selection for the considered $p_T(D^0)$ bin.

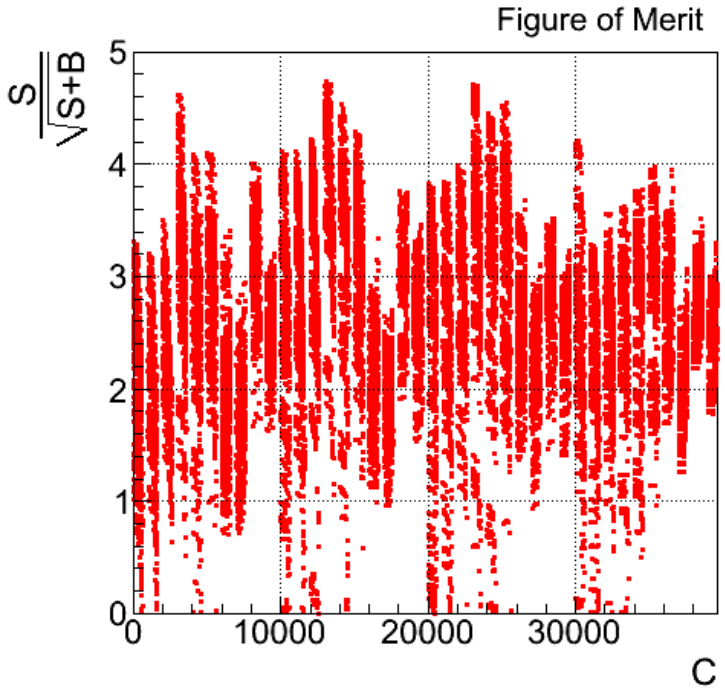

Figure 7.1: Figure of merit versus the configuration number for sample A, in the range $1.5 \leq p_T \leq 2.5$ GeV/c.

7.2 Optimized selection

We apply the same optimization procedure considering all the candidates with $p_T(D^0) \geq 1.5$ GeV/c and we obtain the optimized integrated selection; thus, for each bin of p_T, we compare this selection with the one optimized in the single bin in order to check if the bin by bin optimization is actually the best way to discriminate the signal. As we expected, Fig. 7.2 shows that the figure of merit obtained with the bin by bin selection is higher or equal to the one obtained with the integrated selection for each bin.

For the measurement of the D^0 yields as a function of p_T, we decided to consider only the bins with a figure of merit $\gtrsim 3$, where the separation of the signal from the background is larger. Thus, we considered the p_T range from 0.5 GeV/c to 6.5 GeV/c.

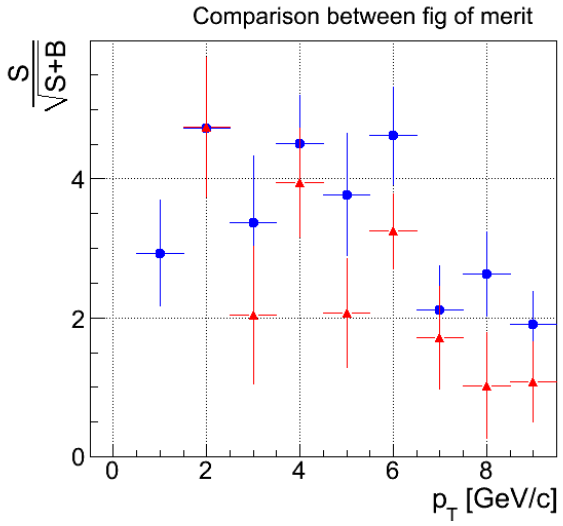

Figure 7.2: Comparison of the figures of merit for the selection optimized on the whole p_T spectrum (red) and for the selection optimized bin by bin (blue).

7.3 Yields as a function of $p_T(D^0)$

Fig. 7.3 shows the results of the fits on data in each $p_T(D^0)$ bin. The blue line represents the result of the fit; the combinatorial background (red) and the WS (green) contributions are also shown.

It is important to highlight that we are able to measure the D^0 signal in the $0.5 \leq p_T(D^0) \leq 1.5$ GeV/c bin, as shown in Fig. 7.3 (a), only because of the of MB and ZB bias triggers and because we unfold the signal from the background via the bin by bin optimization procedure.

Summing the yield for each $p_T(D^0)$ bin, even if the selections are different for each $p_T(D^0)$ bin, we obtain an estimate of the number of D^0 and $\bar{D}^0$ in the studied range $0.5 \leq p_T(D^0) \leq 6.5$ GeV/c.
Fig. 7.4 shows the fitted D^0 yields as a function of p_T and Tab. 7.2 summarizes the fit results.

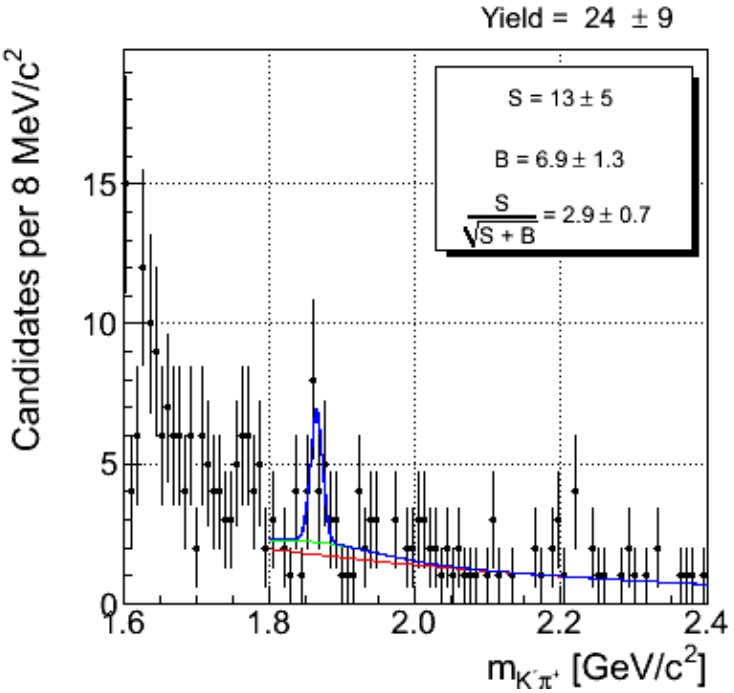

(a) $0.5 \leq p_T(D^0) < 1.5$ GeV/c

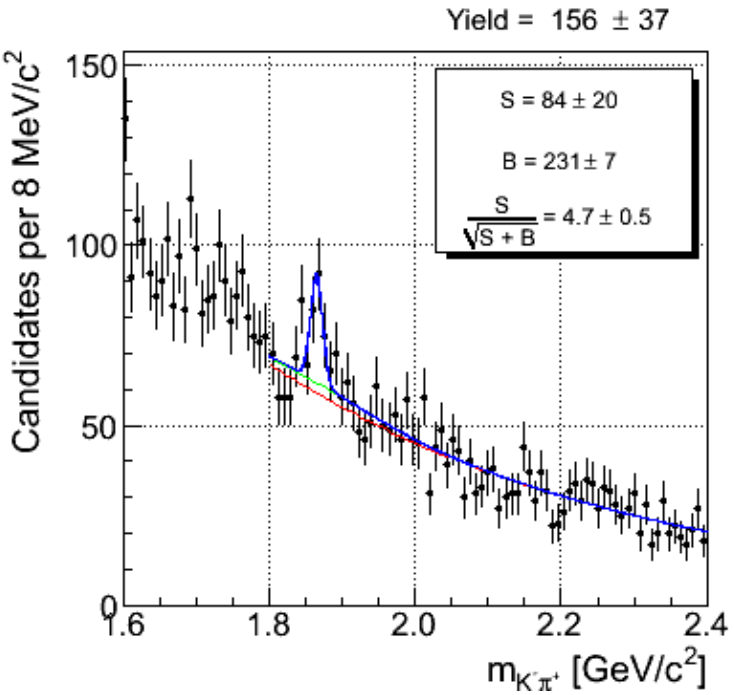

(b) $1.5 \leq p_T(D^0) < 2.5$ GeV/c

Figure 7.3: Invariant $K^-\pi^+$ mass fit of data in 1 GeV/c intervals of $p_T(D^0)$. The blue line represents the result of the fit; the combinatorial background (red) and the WS (green) contributions are also shown.

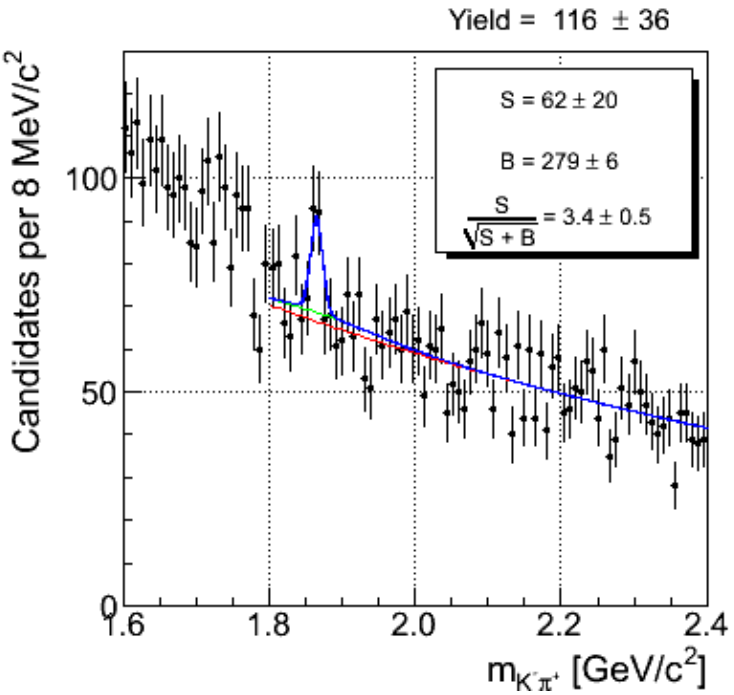

(c) $2.5 \leq p_T(D^0) < 3.5$ GeV/c

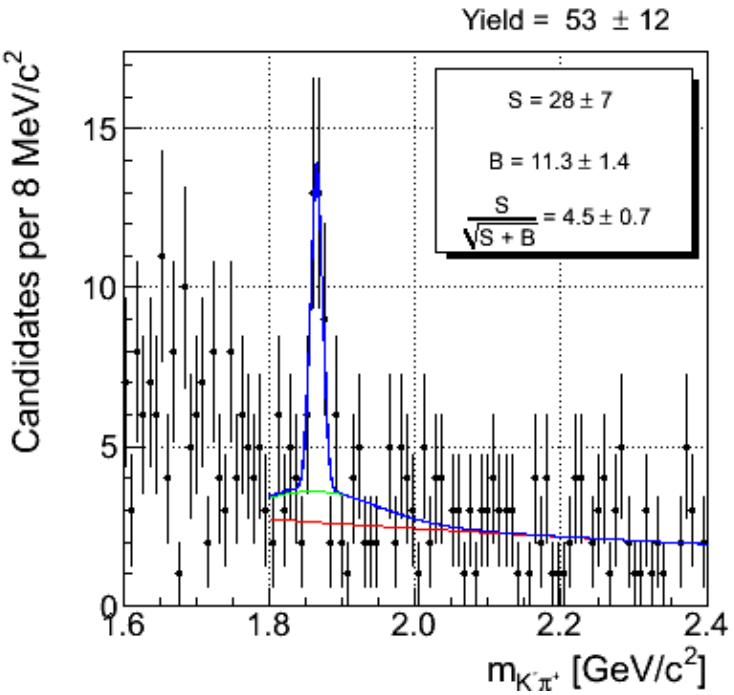

(d) $3.5 \leq p_T(D^0) < 4.5$ GeV/c

Figure 7.3: Invariant $K^-\pi^+$ mass fit of data in 1 GeV/c intervals of $p_T(D^0)$. The blue line represents the result of the fit; the combinatorial background (red) and the WS (green) contributions are also shown.

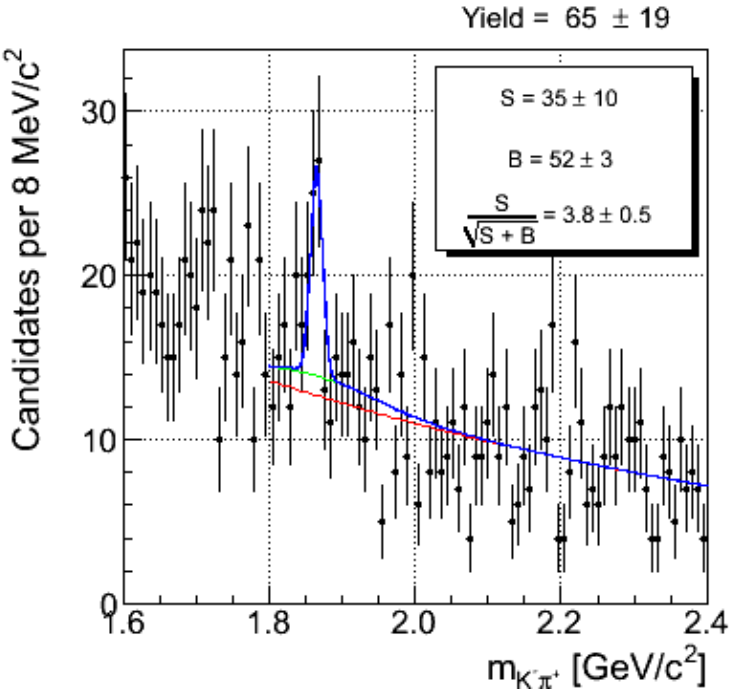

(e) $4.5 \leq p_T(D^0) < 5.5$ GeV/c

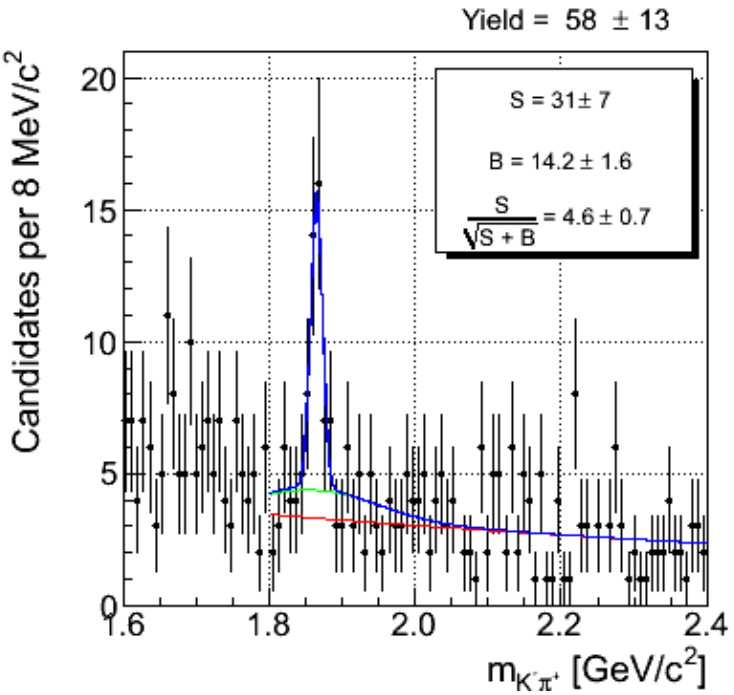

(f) $5.5 \leq p_T(D^0) < 6.5$ GeV/c

Figure 7.3: Invariant $K^-\pi^+$ mass fit of data in 1 GeV/c intervals of $p_T(D^0)$. The blue line represents the result of the fit; the combinatorial background (red) and the WS (green) contributions are also shown.

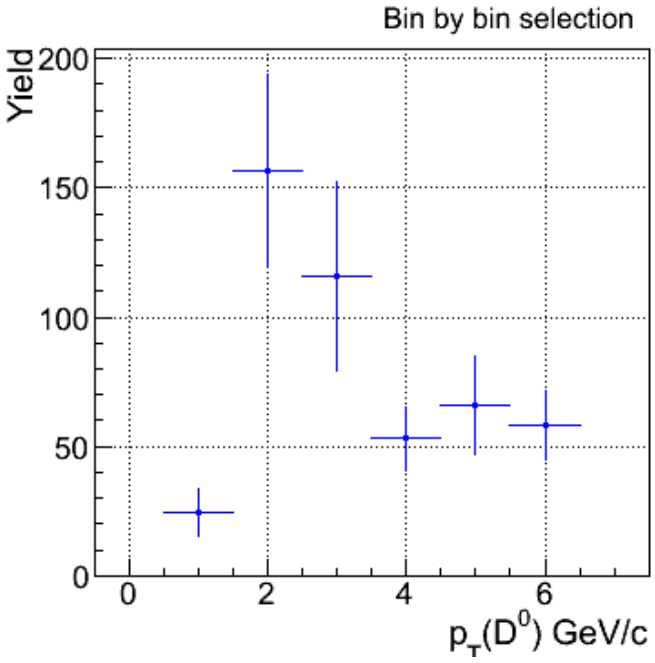

Figure 7.4: Yields as a function of p_T obtained with the bin by bin optimization.

p_T [GeV/c]	Yield	σ_{Yield}	σ_{Yield}/Yield
0.5 – 1.5	24	9	38%
1.5 – 2.5	156	37	24%
2.5 – 3.5	116	36	31%
3.5 – 4.5	53	12	23%
4.5 – 5.5	66	19	29%
5.5 – 6.5	58	13	22%
Total	473	58	12%

Table 7.2: $p_T(D^0)$ range, correspondent yield and uncertainties.

Conclusions

In this analysis, we presented a study of the D^0 meson production at $\sqrt{s}$ = 900 GeV in the Minimum Bias and Zero Bias samples collected by the CDF experiment at the Tevatron Collider. Our study belongs to a series of experimental QCD studies in the kinematic conditions where the perturbative QCD does no longer apply and the behavior of the strong interactions is not well understood.

The D^0 yields as a function of p_T has been measured. Specifically, we evaluated the raw yield of the D^0 meson in the decay channel $D^0 \to K^-\pi^+$ ($\bar{D}^0 \to K^+\pi^-$) as a function of the D^0 transverse momentum in the range $0.5 \leq p_T \leq 6.5$ GeV/c.
A preliminary step was also completed. We developed a procedure to reconstruct the beam and we successfully reconstructed its position for the low energy runs. The beam position we measured can be further exploited by other analyses of the collaboration.
We successfully unfolded the D^0 signal from the background, thus completing the main step toward the measurement of the D^0 differential production cross section. This result is of particular importance since such measurement is likely to remain the only one of its kind for several years.

Our result is consistent with what is expected from a rough extrapolation of the total $c\bar{c}$ cross section measurement performed at different energies.

Bibliography

[1] P. W. Higgs, *Broken Symmetries, Massless Particles And Gauge Fields*, Phys. Lett. **12** (1964) 132.

[2] P. W. Higgs, *Broken Symmetries, Massless Particles And Gauge Fields*, Phys. Lett. **13** (1964) 508.

[3] M. R. Pennington, *Swimming with quarks*, http://arxiv.org/pdf/hep-ph/0504262

[4] K. Nakamura *et al.* [Particle Data Group], J. Phys. G **37**, 075021 (2010).

[5] A.V. Manohar and M. B. Wise, Camb. Monogr. Part. Phys. Nucl. Phys. Cosmol. **10**, 1 (2000).

[6] G. 't Hooft, Nucl. Phys. B **44**, 461 (1972).

[7] B. W. Lee, Phys. Rev. D **5**, 823 (1972).

[8] Ikaros I. Y. Bigi, *Charm physics - like Botticelli in the Sistine chapel*, hep- ph/0107102 (2001).

[9] G. Isidori *et al.* [LHCb Collaboration], arXiv:1111.4987v1 [hep-ph], (2011).

[10] D. Acosta *et al.* [CDF Collaboration], Phys. Rev. Lett. **91**, 241804 (2003).

[11] A. Adare *et al* [PHENIX Collaboration], Phys. Rev. Lett. **97**, 252002 (2006).

[12] J. Adams *et al.* [STAR Collaboration], Phys. Rev. Lett. **94**, 062301 (2005).

[13] B. I. Abelev *et al.* [STAR Collaboration], Phys. Rev. Lett. **98**, 192301 (2007).

[14] R. Bala, for the ALICE Collaboration, arXiv:1201.0729v1 [nucl-ex], (2012).

[15] B. A. Kniehl, G. Kramer, I. Schienbein and H. Spiesberger, AIP Conf. Proc. 792, 867 (2005).

[16] B. A. Kniehl, G. Kramer, I. Schienbein and H. Spiesberger, Phys. Rev. Lett. **96**, 012001 (2006).

[17] Fermilab Beam Division, *Run II Handbook* and *Operations Rookie Books.*

[18] R. Blair *et al.* [CDF Collaboration], *The CDFII Detector : Technical Design Report*, FERMILAB-Pub-96/390-E (1996).

[19] D. Acosta *et al.*, CDF note 6052, 2002.

[20] S. Klimenko, J. Konigsberg and T. Liss, CDF note 6314, 2003.

[21] N. Goldschmidt CDF note 10650, 2011.

[22] K. Anikeev, P. Christoph and P. Murat, *Description of Bgenerator II*, CDF note 5092, 1999.

[23] R. Brun *et al.*, *GEANT: Simulation Program For Particle Physics Experiments. User Guide and Reference Manual*, 1978.

[24] R. Brun *et al.*, *ROOT object oriented data analysis framework.*, http://root.cern.ch.

[25] http://pdg.lbl.gov/2011/hadronic-xsections/

[26] H. Stadie *et al.*, CDF note 6327, 2003.

[27] H. Wenzel *et al.*, CDF note 1924, 1993.

Allegato: sommario in lingua italiana

In questo lavoro di tesi è presentato uno studio della produzione del mesone D^0 nelle collisioni protone-antiprotone. I dati in analisi sono stati raccolti dall'esperimento CDF II presso il collisionatore di protoni e antiprotoni Tevatron sito al Fermi National Accelerator Laboratory. Questo lavoro fa parte di uno specifico sforzo da parte della collaborazione CDF per misurare la sezione d'urto differenziale dei mesoni contenenti quark di tipo charm nella regione cinematica dei bassi momenti trasversi.

Lo studio della produzione dei mesoni D^0 a basso momento transverso a differenti energie nel centro di massa è un'opportunità per arricchire l'attuale conoscenza sul comportamento dell'interazione forte nella regione in cui la produzione del quark c avviene in condizioni non perturbative. L'attuale teoria di cromodinamica quantistica (QCD) infatti non è in grado di descrivere il comportamento dell'interazione forte nella regione dei bassi quadri-momenti transferiti (basso Q^2), a causa del *running* della costante di accoppiamento α_S. In queste condizioni cinematiche, α_S è dell'ordine dell'unità, quindi le teorie pertubative non sono applicabili. Studi sperimentali in questa regione sono fondamentali per superare la limitazione teorica e fornire spunti per nuovi modelli.

Il mio lavoro di tesi, supportato dal gruppo di ricerca CDF Bologna, è un'estensione dei precedenti lavori della collaborazione CDF sui mesoni D^0 e concerne l'analisi del campione di dati raccolto all'energia di 900 GeV nel

centro di massa durante il cosidetto "Low Energy Scan". Si è per la prima volta osservata la produzione di D^0 a basso momento trasverso a questa energia. Il campione di eventi analizzato è il più numeroso mai raccolto ad un collisionatore adronico in queste condizioni sperimentali.

Obiettivo primario dell'analisi è stato la misura del numero di D^0 prodotti in funzione del loro momento trasverso. Si è selezionato il canale di decadimento $D^0 \to K^-\pi^+$ ($\bar{D}^0 \to K^+\pi^-$) per la sua semplice topologia, la sua buona efficienza di ricostruzione (entrambi i prodotti di decadimento sono carichi e visibili dall'apparato di tracciamento di CDF) e per il *Brancing Ratio* relativamente alto (circa 3.9%).

E' stato necessario effettuare una misura preliminare per poter finalizzare analisi: poiché per i run a bassa energia la posizione del fascio non era stata ricostruita, si è dovuto studiare una procedura ad hoc per tale ricostruzione. La posizione del fascio è stata quindi ricostruira indipendentemente per ogni run: potranno beneficiare del risultato ottenuto anche altre analisi della collaborazione. La necessità di questa misura è data dal fatto che la segnatura del decadimento dei mesoni D^0 è un vertice secondario distante dal vertice primario di interazione diversi micron. E' stato quindi possibile estrarre il segnale di D^0 dal fondo costituito da mesoni leggeri e misurarne il numero in funzione del momento trasverso nell'intervallo fra 0.5 GeV/c e 6.5 GeV/c. La misura del numero di D^0 in tale intervallo di p_T è stata possibile grazie all'utilizzo degli eventi raccolti dai trigger di Minimum Bias e di Zero Bias e grazie anche alla procedura di ottimizzazione della selezione studiata nell'analisi.

La tesi si articola in sette capitoli. Nel primo viene presentata una breve introduzione teorica, mentre nel secondo viene descritto l'apparato sperimentale. Il capitolo tre descrive il campione utilizzato e la strategia d'analisi. Il capitolo quattro è dedicato alla procedura di ricostruzione della posizione del fascio ed ai suoi risultati per i run considerati. Nel capitolo cinque sono descritte le tecniche di simulazione Monte Carlo utilizzate per l'analisi preliminare dei dati. Nel capitolo sei viene presentata l'evidenza del segnale di D^0. Nel settimo capitolo è illustrata la misura del numero di D^0 prodotti in funzione del loro momento trasverso.

Acknowledgements

A un uomo gentile e onesto va il mio primo ringraziamento: al Prof. Franco Rimondi. E' stato lui a volere fortemente questa analisi, a volermi in questo gruppo ed io non posso che essergli riconoscente per il fatto che, nonostante tutte le difficoltà, ho concluso un lavoro che mi ha reso un fisico migliore e mi ha dato la possibilità di conoscere un manipolo straordinario di persone che, veramente, "buttano il cuore oltre l'ostacolo". E' stato lui, insieme a Milena, a darmi l'opportunità di "scoprire l'America" ed il suo anomalo, ma straordinario ambiente di lavoro. Con lui è iniziato questo mio lungo viaggio chiamato tesi e ora, insieme alla gioia della finalizzazione, rimane un retrogusto amaro.

Il suddetto "manipolo straordinario" è il gruppo CDF Bologna. Per aver raccolto un pesante testimone, ringrazio il dott. Stefano Zucchelli che ha avuto il cuore e la volontà di completare insieme a me questo lavoro.
Ringrazio il dott. Manuel Mussini, che, con infinita pazienza e tempra instancabile, per questi mesi mi ha preso per mano e mi ha guidato lungo tutta l'analisi: senza di lui avrei continuato a proiettare grafici a caso e a disperarmi ogni quindici minuti. In questi mesi è stato per me un grande insegnante e un amico. Quanto gli devo non è neanche numerabile....
Ringrazio anche il dott. Niccolò Moggi per aver accettato di correggere la mia tesi nonostante non fosse suo compito, nonostante l'influenza e nonostante la mancanza di sonno; i suoi preziosi consigli sono stati quanto mai graditi.
Infine ringrazio la dott.ssa Milena Deninno per il suo apporto a questo lavoro, ma soprattutto perché non è da tutti essere sorridenti e gentili anche nella più buia delle ore.

Ringrazio gang di Cottonwood: Vitolino che mi ha dato un tetto sopra la testa, Phede che mi ha contagiato con la sforzite, Colò per gli abbracci gratuiti, Pisotti perché è completamente matto e Vittorio, perché se va male c'è sempre l'industria. Poi ancora Jen, Elettra e Céline, perché le donne che vestono al contrario han capito tutto dalla vita. Grazie per non avermi fatto mai sentire sola nello sconfinato Yankee-continente. I luv u, pipol.

Ringrazio l'Ele-di-Milano perché è pur essendo continuamente super impegnate siamo riuscite a trovare uno strano equilibrio a distanza per coltivare la nostra stupenda amicizia. Non era facile.

Ringrazio l'Elisa perché essere certe persone non è affatto facile e lei ci riesce alla grandissima. Sei una roccia e sei per me un'ispirazione.

Ringrazio la Fede perché tutti i giorni mi fa scoprire chi sono e chi voglio diventare.

Ringrazio Luca perché è mio fratello e in famiglia ci si ama nonostante tutte le malefatte, i giudizi e le foto col pizzetto.

Ringrazio tutti i miei amici, fra cui in particolare Vinci, Sotti, Marquez, Giova, la Tasso, Edo, la Viola, Brogna, Sighi, Giacomo, gli Ornitorinchi, i semiotici in genere e le regaz del basket perché se cinque anni di fisica non mi hanno trasformato in una nerd irrecuperabile è soprattutto merito loro.

Ringrazio il mio topo perché cresciamo ogni giorno insieme, perché mi sopporta quando sclero, perché mi ha dettato le correzioni di questa tesi all'una di notte, perché dopo quasi due anni che viviamo a Bologna non sa ancora qual è il nostro ripiano del frigo, ma ha sempre riconosciuto cosa è bene per noi. Nelle cose importanti sei la mia guida. Andiamo bene...

Infine ringrazio la mia mamma, perché è la mia mamma e nessuno tranne lei sa cosa questo comporti...